IISc Theses Abstracts

Contents

J. Indian Inst. Sci., Sept.–Oct., 1993, **73**, 471–543

IISc THESES ABSTRACTS

Thesis Abstract (Ph.D.)

BIPEDS: A class of self-routing permutation networks for array processing systems by
P. Navaneethan
Research supervisor: Lawrence Jenkins
Department: Electrical Engineering

1. Introduction

Modern scientific and engineering computations are quite involved, and distributed computing is being considered as a possible solution for the speed-up of these computations. In this model of computing, multiple CPUs are employed, and the given task is split up into many subtasks and are distributed among the multiple CPUs. To solve the main task co-operatively, the multiple CPUs have to communicate among themselves. Interconnection networks[1], which are functionally similar to telephone exchanges, facilitate such communication.

In this work, two important distributed computation models, namely, the single instruction and multiple data stream[2] (SIMD), and multiple instruction and multiple data stream[2] (MIMD) are first explained briefly to illustrate the use of interconnection networks. The current literature on interconnection networks, and the main results and conclusions of this work are discussed.

2. Distributed computation models

2.1. *SIMD Model*

Let us consider the computation of $S = a_1+a_2+\ldots+a_{12}$, in which only the 'addition' operation is involved. Typically, in a sequential computation, we shall compute the value of S as per the following algorithm:

S: =0; For i: =1 to 12 do S: = $S+a_i$;

To speed up the above process, we shall split it up into subprocesses, namely, S_1, S_2, and S_3, where $S_1 = a_1+a_2+a_3+a_4$; $S_2 = a_5+a_6+a_7+a_8$; $S_3 = a_9+a_{10}+a_{11}+a_{12}$. Each of these processes can be run concurrently on three different CPUs, namely, A, B, and C. Once these processes are carried out, we can compute the value of S, through the process $S = S_1+S_2+S_3$. In order that this process be initated, say by the CPU A, the CPUs B and C have to communicate CPU A as to whether their respective processes are over. To facilitate this communication, there should be some communication channel that can be shared by these processors.

2.2. *MIMD model*

Consider the computation of S, where $S = (a_1+a_2+a_3+a_4)^2 + (a_5{}^*a_6{}^*a_7{}^*a_9)^{1/2} + \text{Log}\,(a_9/a_{10}/a_{11}/a_{12})$, and in this case, the multiple instructions that are involved are addition, multiplication, division, squaring, square-rooting and computing logarithm.

Let us assume that we have three processors, namely, A, B, and C and that they have the pair of facilities (adder, square-rooter), (multiplier, logarithimic unit), and (divider, squarer), respectively. We shall initially allocate the subprocesses $S_1 = (a_1+a_2+a_3+a_4)$, $S_2 = (a_5{}^*a_6{}^*a_7{}^*a_8)$ and $S_3 = (a_9/a_{10}/a_{11}/a_{12})$ to the CPUs A, B, and C, respectively. Once these processes are over, the subprocesses $S_4 = (S_1)^2$,

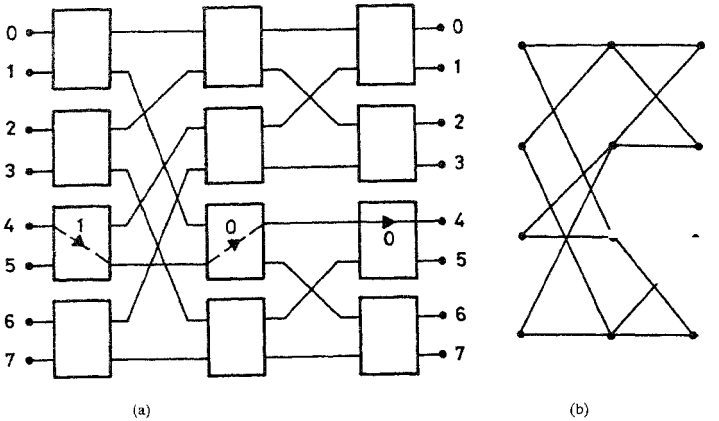

FIG. 1 (a) An 8×8 BIPED network and (b) RGM of the BIPED of Fig. 1(a).

$S_5 = (S_2)^{1/2}$, and $S_6 = \log(S_3)$ are to be carried out by the processors C, A and B, respectively. In order that these be carried out, the CPUs A, B, and C, have to communicate C, A, and B, the values of S_1, S_2, and S_3, respectively. This communication pattern represents a permutation on (A,B,C). To facilitate this type of communication, permutation networks are used.

3. Literature survey

Multistage interconnection networks (MINs)[1] make use of (2×2) crossbar switches as primitive building blocks. The n-stage permutation networks, where $N = 2^n$, are the Omega network[2], the Multistage Cube[4], the Flip network[5], the Baseline and the Reverse Baseline networks[5]. These networks are referred to as 'classical networks'[6], and realize only a subset of the possible N! permutations. Moreover, these networks are also self-routing, otherwise known as destination-tag controlled. If $d_1\ d_2 \ldots\ d_n$ denotes the destination address in binary, then the switch in the ith stage makes use of the bit d_i to establish the path to the destination; *i.e.*, if $d_i = 0$, the path is established through the top output of the switch, else through the bottom output, and further destination bits are sent along the same path to the ensuing stage.

Wu and Feng[5] have proved that the classical networks are topologically equivalent to one another *i.e.*, by rearranging the switches of one network, one can realize the other. Similarly, two networks are said to be functionally equivalent, if by renaming the sources and/or the destinations of one network, it can be made to realize the same set of permutations or the other. Agrawal *et al*[7] have designed non-equivalent networks on the basis of graph models, but they are not guaranteed to be self-routing.

4. Main results and conclusions

In this work, a matrix model has been developed to represent a class of self-routing networks, known as Bipeds, whose structure resembles that of a two-legged animal. This model is shown to encompass many non-equivalent networks, and one such example of an (8 × 8) Biped is shown in Fig. 1, along with its reduced graph model[7] (RGM) which is non-isomorphic to that of the baseline network.

A new concept of *macro cycle* has been introduced on the basis of the entries of the matrices. It is shown that these macro cycles have direct relationship with those of the bipartite loops[7], and this relationship can be used to design non-equivalent self-routing networks with the desired loop structures[7] by appropriately choosing the entries of the matrices.

A new class of permutation, known as *quotient-pair permutation*, has been identified, and on the basis of this permutation, equivalence relationships among Bipeds have been studied. It is shown that for every Biped, there exists an equivalent Biped, known as OE-Biped, whose odd, even rows of the matrices satisfy certain conditions. This result is of significance to the reduction in the search time for a suitable functionally non-equivalent permutation network.

Bounds on the number of non-equivalence classes of self-routing networks have been derived, and the lower bound is shown to be related to integer-partitioning of integers. To derive the upper bound, the problem has been split up into derivations of bounds, on the buddy[7] and non-buddy class of Bipeds. In the former case, the conditions for two OE-Bipeds to be non-automorphic (isomorphic), and in the latter case, the conditions for two OE-Bipeds to be automorphic, have been derived, and have been made use of to derive the respective bounds.

A sufficient condition for Baseline equivalence is first derived, and is shown to encompass the sufficient condition derived by Bermond *et al*[6], as a special case. A new class of permutations, known as permutations induced on the leaves due to an automorphism on the binary tree (PLUMB), is identified, and then on the basis of this permutation, necessary and sufficient conditions for an OE-Biped to be equivalent to the Baseline network have been derived.

The set of sources of a Biped are partitioned on the basis of destination groups. It is shown that two paths will be non-blocking if and only if the pair of sources corresponding to a pair of destinations of the same group belong to disjoint source-partitions. This result is extended to derive the necessary and sufficient conditions for a permutation to be realized by a given Biped.

Further work relates to the identification of a subclass of OE-Bipeds such that for every OE-Biped there exists an equivalent Biped in this subclass. Such an identification will help reduce the search time further. Moreover, equivalence within the class of Bipeds which have identical macro cycle structures needs to be investigated.

References

1. FENG, T Y. — A survey of interconnection networks, *IEEE Computer*, 1981, **14**, 12–27.
2. HWANG, K. AND PRIGGS, F.A. — *Computer architecture and paralle processing*, 1985, McGraw-Hill.
3. LAWRIE, D. H. — Access and alignment of data in an array processor, *IEEE Trans*., 1975, **C-24**, 1145–1155.
4. SIEGEL, H J. AND MCMILLEN, R. J. — The multistage cube: A versatile interconnection network, *IEEE Computer*, 1981, **14**, 631–642.
5. WU, C. L. AND FENG, T. Y — On a class of multistage interconnection networks, *IEEE Trans* , 1980, **C-29**, 694–702.
6. BERMOND, J. C. AND FOURNEAU, J. M — Independent connections An easy characterization of Baseline equivalent multistage interconnection networks, *Theor Comput. Sci* , 1989, **64**, 191–201
7. AGARWAL, D. P., KIM, S. C AND SWAIN, N. K — Analysis and design of non-equivalent interconnection networks, *IEEE Trans* , 1983, **C-32**, 637–647

Thesis Abstract (Ph.D.)

Learning automata algorithms for connectionist systems: Local and global convergence

by V. V. Phansalkar
Research supervisor: M. A. L. Thathachar
Department: Electrical Engineering

1. Introduction

Connectionist systems have been studied with much interest as models for the brain and also as systems which work in a parallel and distributed manner These systems exhibit desirable properties such as learning capability and robustness.

Learning algorithms for connectionist systems are developed and analysed in this work. Connectionist systems based on the generalised reinforcement learning model are considered. This model consists of a learning system and an environment interacting with each other. The environment is characterised by a set of context vectors and a set of actions. At each instant the environment generates a context vector which forms an input to the learning system. Based on its internal state and the context vector from the environment, the learning system outputs an action affecting the environment. This evokes a response from the environment indicating the suitability of the action to the particular context vector. The learning system then updates its internal state based on this information using an algorithm. Algorithms to learn the optimal action for each context vector are considered here. The algorithms are completely decentralised and there is no information exchange involved between the various units of the system.

The problem of learning the optimal action is posed as an optimisation problem with respect to the internal state of the learning system. Then, using weak convergence techniques[1], the algorithm under consideration is approximated by an ordinary differential equation (ODE) or a stochastic differential equation (SDE). The ODE/SDE and the optimisation problem are studied together to show that the algorithm converges to a solution of the optimisation problem. Two types of algorithms are considered here, the L_{R-I}[2] and the REINFORCE[3]-type algorithms. First, local algorithms, that is, algorithms that converge to local solutions of the optimisation problem are considered.

2. Local results

Initially, connectionist systems in which the units are composed of hierarchies of teams of learning automata[2] are analysed. The linear reward–inaction (L_{R-I}) algorithm is used. This is approximated by an ODE using weak convergence techniques. This ODE is shown to have properties which indicate that it solves the related optimisation problem locally. As the asymptotic behaviour of the algorithm and the ODE are similar, the algorithm converges to a local solution of the optimisation problem. Global convergence is not achievable in general, but if the problem is simple enough, globally optimal solutions are obtained.

Next, the REINFORCE algorithm[3] is analysed. The ODE approximating this algorithm is shown to have unbounded solutions by giving an example This is also confirmed through simulation results of the same example. A new algorithm based on constrained optimisation is presented and analysed. It is shown that this algorithm overcomes the problem of unboundedness and also exhibits local convergence properties

3. Global results

In many cases, local properties are not sufficient and global solutions are required. One way to obtain global solutions is to use a gradient following algorithm along with a random perturbation to enable the algorithm to get out of local optima which are not globally optimal, such as in simulated annealing and the constant temperature heat bath algorithms. Simulated annealing and the constant temperature heat bath algorithms have been applied to discrete state space optimisation with the exact function values known. Here, the optimisation is in $\mathbf{R}^5$ and only sample values of the function are available at each instant. The algorithms used are therefore gradient following with an additive random noise. These algorithms are approximated by SDEs. It is known that the Langevin equation solves a global optimisation problem. Algorithms based on this idea are suggested to solve the optimisation problem globally.

An algorithm based on the modified REINFORCE algorithm described above is developed. It is shown that this algorithm can be approximated by the Langevin equation and thus global properties are obtained. These techniques can also be used to obtain global results for learning automata in connectionist systems. It is difficult to apply such techniques directly. So the learning automata are parametrised and algorithms

with global convergence properties are developed. These parametrised learning automata (PLA) can be used in various applications for obtaining global solutions.

4. Three-layer network for pattern recognition

One of the most popular structures for pattern recognition is the three-layer feedforward network[4]. This network can be formed with each unit comprising a team of learning automata using the L_{R-I} algorithm. The analytical results of Section 2 hold for this structure. The global results of Section 3, with each learning automaton (using the L_{R-I}) replaced by a PLA, also hold.

Simulations were conducted on pattern recognition problems using these types of feedforward networks. Both the local (L_{R-I}) and global (PLA) algorithms were used.

When the local algorithm (L_{R-I}) is used, convergence to the optimal solution is assured only if the initial conditions are correctly chosen. This is because the use of the L_{R-I} guarantees only local convergence. Convergence to the global optimum is obtained when the initial conditions are proper, or when the problem is simple enough.

If there is not much knowledge about the problem, global algorithms using the PLA described in Section 3 can be used. A pattern recognition problem is simulated using PLA, with a high bias towards a local optimum which is not a global optimum. The network of PLAs converged to the globally optimal set of actions. With the same bias towards a local optimum, the network with the L_{R-I} converged to the local optimum.

5. Simulations

The analytical results described in sections 2 and 3 do not give any indication about the rate of convergence of the algorithms. Simulations are performed to show that the rate of convergence is acceptable. One set of simulations has already been described in connection with the three-layer pattern recogniser.

Simulations for the REINFORCE algorithm show that the solutions can become unbounded and the new algorithm does not have this problem. The PLA can also be used in a common payoff game with no knowledge of the existence of other players, that is, it is totally decentralised. Simulations show convergence to the optimal solution in this case also. In particular, simulations of a two-person, two-action game show that the PLA does converge to the global optimum even with a high bias in favour of the non-optimal actions.

6. Conclusions

The results show that learning automata can be used as basic units in connectionist systems. Simulations show that the rates of convergence are acceptable. Depending on the application on hand either local or global algorithms can be used.

References

1. KUSHNER, H. J. — *Approximation and weak convergence methods for random processes with applications to stochastic systems theory*, 1984, MIT Press.

2. NARENDRA, K. S. AND THATHACHAR, M. A. L. — *Learning automata: An Introduction*, 1989, Prentice Hall.

3. WILLIAMS, R. J. — *Toward a theory of reinforcement–Learning connectionist systems*, Technical Report NU–CCS–88–3, North Eastern University, Boston, July 1988.

4. MEISEL, W. S. — *Computer-oriented approaches to pattern recognition*, 1972, Academic Press.

Thesis Abstract (Ph.D.)

Finite section convolution integral operators—Structure of resolvent and solution of first kind equations by B. R. Shankar
Research supervisor: R. Vittal Rao
Department: Mathematics

1. Introduction

Finite-section integral operators occur in a wide variety of physical problems. Such operators have been extensively studied in connection with their application in radiative transfer[1,2] and neutron transport theory[3]. Of particular interest are such operators with difference kernels. When the interval of integration is the full real line, direct Fourier transform methods can be employed to solve nonhomogeneous integral equations involving such operators. When the interval of integration is the non-negative half line, then one has the famous Wiener–Hopf technique to study such equations[4,5]. However, when the interval of integration is finite, we have, what we call as a finite-section integral operator of the form

$$Kf = \int_0^t k(x-y)f(y)dy \tag{1}$$

and the above-mentioned methods are not directly applicable. All the same, extensive results are available on the spectrum of such operators—for instance, one can find such results in Leonard and Mullikin[6] & Vittal Rao[7] (this being, by no means, an exhaustive list, but giving only a flavour of such results). Further, various methods are available to study the resolvent of such finite-section operators with difference kernels. Leonard and Mullikin[8] have shown that the resolvent of such an operator is completely determined by its action on the function $\exp(-xz)$, where z is a complex parameter.

One can also observe that since the resolvent kernel $R_\lambda(x,y)$ for such an operator is itself the solution of the integral equation,

$$R_\lambda(x,y) = k(x-y) + \lambda \int_0^t k(x-s)R_\lambda(s,y)ds, \tag{2}$$

one can formally differentiate with respect to t to get,

$$\frac{\partial R_\lambda}{\partial t}(x,y) = \lambda k(x-t)R_\lambda(t,y) + \lambda \int_0^t k(x-s) \frac{\partial R_\lambda}{\partial t}(s,y)ds \tag{3}$$

thus giving

$$\frac{\partial R_\lambda}{\partial t} = \lambda R_\lambda(x,t)R_\lambda(t,y). \tag{4}$$

Equation (4) seems to suggest some kind of separation of the x and y variables. However, one has to be careful, since if in (2), we replace the term $k(x-y)$, before the integral on the right side, by any function $g(x,y)$, then also, the solution of the eqn (2) satisfies (4), at least formally. Equations of the type (4) have been considered, for instance, by Sobolev[9] and Bellman *et al*[10].

2. Contribution of the thesis

We investigate the structure of the solutions of Fredholm integral equations of the first and second kinds

with convolution kernels on finite intervals and some of its applications. We consider the second kind equation

$$f(x)-\lambda \int_0^t k(x-y)\, f(y)\, dy = g(x) \tag{5}$$

where $t>0$, $k(x) \in L_2[-t,t]$, $g(x) \in L_2[0,t]$, and $f(x) \in L_2[0,t]$, f being the unknown function. The above equation (5) may be written as

$$(I-\lambda K)\, f = g.$$

If λ is not in the spectrum of the operator K, the resolvent $(I-\lambda K)^{-1} = R_\lambda$ exists as a well-defined, bounded linear operator on $L_2[0,t]$. We show that R_λ is determined by its action on the constant function and one more specially chosen function, $\gamma(x)$. In obtaining the representation for R_λ, essential use is made of the following theorem.

Theorem: Let T be any bounded linear operator on $L_2[0,t]$. Then $\exists$ a kernel $\gamma(x,y)$ *s.t.*

$$(Tf)(x) = \frac{d}{dx} \int_0^t \gamma(x,y)\, f(y) dy \qquad \forall\, f \in L_2[0,t].$$

For every fixed $x \in [0,t]$, $\gamma(x,y) \in L_2[0,t]$ as a function of y.

It is also shown that the representation for R_λ takes a simpler form in the case of self-adjoint operators; and that in the case of Volterra-type operators, it is determined by its action on the constant function alone.

The above results are applied to obtain a generalisation of the well-known Chandrasekhar–Ambartsumyan X and Y functions, occurring in radiative transfer,[1,2] for a class of bounded linear operators on $L_2[0,t]$. We also obtain a generalization and representation for the scattering function $S(z,\omega)$ in terms of X and Y functions, analogous to that in radiative transfer[2].

Further, a representation is obtained for the solutions of the Fredholm integral equation of the first kind with convolution kernel on a finite interval, *i.e.*, integral equation of the form

$$\int_0^t k(x-y) f(y) dy = g(x).$$

Let $W^2 = \{g \in L_2[0,t]: g', g'' \in L_2[0,t]\}$.

Whenever $g \in W^2$ it is shown that the solution can be expressed in terms of the solutions for special right sides, namely, $g = 11$ and $g = x$.

The above representation is illustrated with an example of a classical kernel, arising from applications, namely, $\log |x-y|$.

References

1. Chandrasekhar, S — *Radiative transfer*, 1960, Dover.
2. Busbridge, I.W. — *The mathematics of radiative transfer*, 1960, Cambridge University Press.
3. Davison, B. — *Neutron transport theory*, 1957, Oxford University Press.
4. Carrier, G.F., Krook, M and Pearson, C.F. — *Functions of a complex variable*, 1966, Ch.8, McGraw-Hill

5 KREIN, M G.	Integral equations on a half-line with kernel depending upon the difference of the arguments, *Am Math Soc Transl* (2), 1962, **22**, 163–288.
6 LEONARD, A AND MULLIKIN, T W	Integral equations with difference kernels on finite intervals, *Trans Am Math Soc*, 1965, **116**, 465–473
7 VITTAL RAO, R	On the eigenvalues of integral operators with difference kernels, *J. Math Anal Appl.*, 1976, **53**, 554–566.
8. LEONARD, A AND MULLIKIN, T W	The resolvent kernel for a class of integral operators with difference kernels on a finite interval, *J Math Phys*, 1965, **44**, 327–340
9 SOBOLEV, V V	*A treatise on radiative transfer*, 1963, D.Van Nostrand.
10. BELLMAN, R., KALABA, R AND UENO, S.	*Invariant imbedding and a resolvent of the proton diffusion*, The RAND Corporation, RM-3937, ARPA, 1964.

Thesis Abstract (Ph.D.)

White dwarf pulsators—A study with the whole earth telescope by S. Seetha

Research supervisor: T. M. K. Marar and N. Kumar
Department: Physics

1. Introduction

White dwarfs are the hot embers left behind by low mass stars at the end of all or most of their nuclear burning stages. A typical white dwarf consists of a carbon/oxygen degenerate core surrounded by thin layers of helium and/or hydrogen. White dwarfs start their evolution at a blazing temperature of over 200,000 K and gradually cool down depending on the composition of the core, its temperature and the blanketing provided by the outer layers

During the process of cooling, white dwarfs tend to pulsate in non-radial gravity modes in specific temperature ranges on their evolutionary track[1]. These narrow temperature ranges are called instability strips. At present, three instability strips exist which are defined as follows:

a) DAV instability strip – 11,000 K $\leq T_{eff} \leq$ 13,000 K
b) DBV instability strip – 24,000 K $\leq T_{eff} \leq$ 29,000 K
c) DOV instability strip – 80,000 K $\leq T_{eff} \leq$ 200,000 K

All white dwarf pulsators and their non-pulsating cousins exhibit similar properties. Their masses are centered around 0.6 $M_{\odot}$, and they have surface gravity of log $g \sim 8$, except for the hot objects which have a log $g \geq 7$. Thus, the white dwarfs form a homogenous class and any inference derived from the study of pulsators can be applied to the other white dwarfs as well.

White dwarf pulsations have periods in the range of 100 to 2000 seconds, and pulsation amplitudes ranging from 0.001 to 0.34 magnitudes. These pulsations can therefore be observed with existing techniques and telescopes

We undertook a study of these pulsations with a view to determine the following important features:

(i) to find the limits of periods of pulsations exhibited by these stars,
(ii) to determine the location of the driving region for these pulsations; and
(iii) to estimate observationally the total energy in these pulsations and hence to determine the physical process responsible for driving them.

The driving of these pulsations is at present believed to occur at the surface layers. The DA instability is caused either due to partial ionization of hydrogen or due to convective blocking. Similarly, the DB

instability is either due to partial ionization of helium or due to convective blocking[2] The DOV stars are extremely hot, and hence the driving could be either due to carbon/oxygen partial ionization or due to nuclear burning.

Our aim was to determine if we could find answers to the above puzzles, with the help of observational data

2. Observational methods and analysis

To determine period limits in the pulsations of these stars, it is necessary to search for periods over a large range. For this purpose we have used long-term data collected using the Whole Earth Telescope (WET), which is a network of co-ordinating telescopes distributed at different longitudes over the Earth[3]. We at ISRO Satellite Centre, Bangalore, India, are one of the collaborators for this network. We have chosen for our analysis, one object from each of the instability strips. For the DA instability strip, we have used data on G29-38, for the DB strip have observations on GD 358, and have observed PG 1159-035 as a representative of the DOV strip. The data on the above objects consist of photometric measurements collected using mainly a two-star photometer at various sites. We therefore observed the program star and a nearby comparison star simultaneously

All the data sets from various sites were reduced and joined together to form one master data set for each program star and comparison star. Typical lengths of master data sets for each star had a duration of at least 10 days, though it was not continuous during the whole range. We have analyzed the data by means of discrete Fourier transform, and obtained the overall power spectrum from about 0.0001 Hz all the way to 0.05 Hz. We have analyzed channel 1 data on the program star and channel 2 data on the spectrum as a measure of the noise in the observations contributed both due to transparency and scintillation effects. We remove from the channel 1 spectrum this effect of noise in the observations contributed both due to transparency and scintillation effects. We remove from the channel 1 spectrum this effect of noise and use the resultant spectrum for our analysis.

We calculate the location of the driving region by using the condition that it should coincide with the adiabatic/non-adiabatic transition zone in the star. This is defined by the relation,

$$M_{\text{driving}} = L \times P / C_v \times T$$

where M_{driving} is the mass of the layers in the star that lie above the driving region, L, the luminosity in erg s^{-1}, C_v, the specific heat at constant volume in erg g^{-1} K^{-1}, P, the period of pulsation in seconds and T, the temperature in K. By using the upper and lower limits of the period P observed for each star (P_{higher} and P_{lower}), we determine the location of the driving region in stellar mass units. We then compute the energy in the pulsations by adding the total power in the spectrum. We then intercompare the values obtained for each of the stars that we have analyzed to determine the process which causes the driving of the pulsations in these white dwarfs.

3. Results and conclusions

The results of our analysis can be summarized as follows:

1) We have determined period limits of the power spectrum calculated for these stars.

For G29-38	$P_{\text{lower}} \approx 57$ seconds
	$P_{\text{higher}} \geq 3333$ seconds
For GD 358	$P_{\text{lower}} = 104$ seconds
	$P_{\text{higher}} \geq 3333$ seconds
For PG 1159-035	$P_{\text{lower}} \approx 357$ seconds
	$P_{\text{higher}} \geq 1000$ seconds

Based on the above period limits we obtain the following locations for the driving regions.

Table I

Star name	Position of outer layer of the driving region from the surface, in stellar mass units	Position of inner layer of the driving region from the surface, in stellar mass units
G29-38 (DAV)	7×10^{-14}	4×10^{-12}
GD358 (DBV)	6×10^{-12}	2×10^{-10}
PG1159-035 (DOV)	4×10^{-08}	1×10^{-7}

The above results indicate that the driving regions are fairly thin and lie on the surface, *i.e.*, at distances $> 0.9\ R_*$. Their location favors partial ionization of a predominant surface element as the driving mechanism, rather than convective blocking in the case of DAV and DBV or nuclear burning in the case of DOV.

2) We have calculated the total energy in these pulsations and estimated the relative values for these stars. These calculations indicate that GD 358 has about 1.6 times the energy in pulsations as compared to G29-38. This also favors the theory that G29-38, being a DAV is driven by partial ionization of hydrogen, and GD 358 being a DBV is driven by helium partial ionization.

PG 1159-035 which is a DOV star has about 5.7 times the energy content as that of G29-38, and 3.6 times that of GD 358. The two results are independent and are consistent. They favor a carbon/oxygen partial ionization as the driving mechanism in PG 1159-035 and similar stars. They also rule out the possibility of nuclear burning being the cause of pulsations in PG 1159-035.

The above results are the first available observational estimates on the nature of the driving regions in white dwarf pulsators.

References

1. WINGET, D.E — *In IAU Symp. No. 123*, Advances in helio- and asteroseismology, (J. Christensen Dalsgaard and S. Frandsen, eds), 1988, p. 305, Reidel
2. COX, A.N., STARRFIELD, S.G., KIDMAN, R.B. AND PESNELL, W.D. — *Astrophys. J.*, 1987, **317**, 303-324.
3. NATHER, R.E., WINGET, D.E., CLEMENS, J.C., HANSEN, C.J. AND HINE, B.P — *Astrophys. J.*, 1990, **361**, 309-317

Thesis Abstract (Ph.D.)

Numerical studies of unsteady boundary layer flow problems by V. Rajeswari
Research supervisor: G. Nath
Department: Mathematics

1. Introduction

Unsteady boundary layer flows are those whose properties depend on time if referenced with respect to an Eulerian frame. Although the boundary layer theory was first developed for steady laminar flows, it was soon realised that most flow problems encountered in practical applications are unsteady and, in

fact, there are no actual flow situations natural or artificial that do not involve unsteadiness. Examples of unsteady flows are flow through turbomachinery blades, dynamic stall of lifting surfaces, stall flutter of helicopter rotor blades, rotating stall in engine compressor blades, ship propellers, accelerated and decelerated rocket missiles and nozzles, to name a few. In the last two decades, the unsteady viscous flows have been extensively studied A recent book on unsteady boundary layers by Pop[1] gives an excellent understanding of the theory of unsteady flows. Also a very recent review article on the unsteady flows by Wang[2] gives the exact solutions of the unsteady Navier–Stokes equations.

2. Present study

The current work presents the numerical studies of some unsteady boundary layer flow problems which have not been studied by any other worker. The first problem deals with the semi-dimensional boundary layer flow over a continuously stretching surface in two lateral directions in a fluid at rest. The velocity of the stretching surface varies arbitrarily with time. Both the nodal and the saddle point regions of flow have been considered. Also, the constant wall temperature (concentration) and constant heat (mass) flux conditions at the wall have been considered In the second problem, the unsteady boundary layer flow caused when a lighter fluid impinges on a heavier fluid which is at rest are considered[3]. The velocity of the spreading surface is either accelerating or decelerating. Both the two-dimensional and the axisymmetric cases have been considered The effect of magnetic field has also been included in the analysis. In the third problem, the study of the unsteady flow over a stretching surface in a rotating fluid is considered[4]. The results appear in two parts Part A deals with semi-similar solution wherein the velocity of the stretching surface and the angular velocity of the rotating fluid varies arbitrarily with time. It has been observed from Part B that when the velocity of the stretching surface and the angular velocity of the rotating fluid varies inversely as a linear function of time, a self-similar solution could be obtained. For both the cases, the variable wall temperature of the stretching surface is considered. In the last problem, the effect of large injection on a vertical thin cylinder in an unsteady free stream is studied taking into account the viscous dissipation.

3. Method of solution

The unsteady boundary layer equations obtained for the above-mentioned problems are highly nonlinear. Thus, by a suitable similarity or semi-similarity transformations, the governing boundary layer equations for each problem are reduced to either ordinary or partial differential equations. Numerical computations are carried out through the implicit finite-difference scheme along with either the quasi-linearisation or the parametric differentiation technique.

4. Results and discussion

The results which are presented in the form of graphs and the comparison tables are analysed and discussed in detail for each problem. The effect of various parameters such as unsteadiness in the wall velocities, stretching ratio, suction, magnetic field, rotation parameter, temperature parameter, etc., on skin friction, heat and mass transfer coefficients as well as on velocity, temperature and concentration profiles have been studied in detail.

From the results of the first problem, it is observed that suction is found to be an important parameter in obtaining a convergent solution in the case of saddle point region of flow. The Prandtl number and the Schmidt number strongly affect the heat and mass transfer of the diffusing species, respectively. For the unsteady flow on the surface of a quiescent fluid, the results show that in the presence of applied magnetic field, velocity overshoot occurs on the upper fluid and is strongly dependent on time and applied magnetic field. The effect of interface velocity is more pronounced on skin friction than on heat transfer. The values of skin friction and heat-transfer coefficients are higher for the two-dimensional case than for the axisymmetric case. In the unsteady flow in a rotating fluid, the rotation parameter, variable wall temperature and velocity distributions of the stretching surface are all found to have significant effect on skin friction and heat-transfer coefficients. The magnitude of temperature parameter strongly affects the direction of the flow and the quantity of the heat transfer between the stretching surface and the ambient rotating fluid. In the case of large injection problem, the dividing streamlines are

shifted away from the boundary due to large rates of injection. Also, for higher values of the curvature parameter, the dividing streamlines are shifted away from the boundary. For large values of the Prandtl number and the Eckert number there is a temperature overshoot near the wall for moderate rates of injection. This implies that due to viscous dissipation, the temperature of the fluid near the wall becomes more than that of the wall, which was originally at a higher temperature and the wall will get heated instead of being cooled.

References

1 POP, I. *Unsteady laminar boundary layers*, 1983, Bucharest, Romania

2 WANG, C Y. Exact solutions of the unsteady Navier–Stokes equations, *Appl. Mech. Rev.*, 1989, **42**, S269–S282.

3 RAJESWARI, V AND NATH, G. Unsteady boundary layer flow on the surface of a quiescent fluid, *Acta Technica, CSAV*, 1991, **36**, 282–291.

4 RAJESWARI, V AND NATH, G. Unsteady flow over a stretching surface in a rotating fluid, *Int J Engng Sci.*, 1992, **30**, 747–756

Thesis Abstract (Ph.D.)

Nuclear magnetic resonance investigations of certain protonic conductors by G. Mangamma

Research supervisor: S.V.Bhat
Department: Physics

1. Introduction

The discovery of high degree of ionic mobility in certain classes of materials like hydrogen uranyl phosphate and arsenate, metal hydrides, tungsten bonzes, β-alumina and intercalation compounds of transition metal disulphide has suggested a wide variety of applications, particularly in the field of high-energy density batteries. On account of their potential applications, these materials, also known as fast ionic conductors (FICS), have become recently a subject of intense investigations. FICs usually contain one, occassionally two, mobile ionic species which exhibit translational diffusion, sometimes along with rotational diffusion. Of the several techniques available to study these materials, nuclear magnetic resonance (NMR) is the most suited for the study of microscopic properties as it essentially looks at individual ions[1,2]. In NMR, information about the diffusion of the nucleus under study is usually obtained by observing the changes in the line width or second moment and in the relaxation times (spin-lattice relaxation time, T_1, spin-lattice relaxation time in the rotating frame, $T_{1\rho}$, and spin-spin relaxation time, T_2) as a function of temperature when interpreted in terms of the Bloembergen, Purcell and Pound (BPP) model[3].

These measurements yield the motional parameters, E_a, the activation energy and τ_{eo}, the pre-exponential factor. However, a long-standing problem with these measurements has been the large discrepancies observed between the values of E_a and τ_{eo} obtained by the NMR experiments and those obtained by conductivity measurement. Various explanations like distribution of the activation energies and correlation times, a breakdown of the absolute rate theory, low-dimensionality effects and non-exponential nature of the correlation times, have been put forward over the years to account for these discrepancies[4]. However, no consensus has yet emerged about this problem. We sought to examine the specific contribution of low dimensionality to the discrepancies by studying the NMR of the same substances prepared in two different structures of differing dimensionalities.

2. Experimental

The compounds investigated are $HMWO_6.1.5\ H_2O$ (where M=Ta or Nb and hydrated layered

perovskite oxide, $HLa_2NbTi_2O_{10}.1.5\ H_2O$. ^1H NMR investigations have been carried out on a home-built-pulsed NMR spectrometer[5,6], whose frequency range is 4–90 MHz and an MSL-300 spectrometer which works at a fixed frequency of 300 MHz

A pulsed-field gradient spin-echo NMR spectrometer was assembled by interfacing a programmable pulse generator and a data acquisition system (designed and fabricated in our laboratory) with other imported units. A general description of the spectrometer is presented. In addition to this, details of the microprocessor-based programmable pulse generator and data-acquisition system are provided. Outlines of the remaining imported units like electromagnet, double-balanced mixer, power amplifier, preamplifier, receiver and pulsed-field gradient unit are given. Measurement of spin-lattice relaxation time, T_1, spin-spin relaxation time, T_2, and spin-lattice relaxation time in rotating frame, $T_{1\rho}$, are also described. A brief discussion on the line narrowing by 'magic angle sample spinning' (MASS) technique has also been given.

3. NMR studies of $HMWO_6.xH_2O$ (M=Nb, Ta) in 2- and 3-dimensional structures

Two different structures (2D and 3D) of $HMWO_6.xH_2O$ (where M = Ta or Nb) have been prepared and studied by different ^1H NMR techniques (T_1, $T_{1\rho}$ and T_2). For the 2D system, ^1H NMR results suggest that system goes from a rigid lattice state to a liquid-like state after a sudden and sharp transition at about 190 K. The low-temperature line shape of the signal shows the evidence for the existence of rigid water molecules and protons as separate entities. T_2 and $T_{1\rho}$ results suggest that at temperatures above 200 K translational motion of the protons dominates. ^1H NMR relaxation data indicate a strong 2D character for ionic diffusion which is assisted by vacancy jump mechanism. Protons jump over vacancies available along 0–0. ^1H NMR results of defect pyrochlore $HMWO_6.H_2O$ (M=Ta or Nb) show that low-temperature signal is due to the water protons of the $HMWO_6$ molecule.

Since $HMWO_6.xH_2O$ is a defect pyrochore system vacancies are formed in A–Y–A channels. Protons of water molecule and single species occupy these vacancies randomly in all these directions. Since ionic motion is random, the analysis of the relaxation data is done with the help of the BPP model and E_a and τ_{c0} are calculated. It was observed that the results of $HMWO_6.xH_2O$ (2D and 3D) are affected by the dimensionality of ionic diffusion. The low temperature line shapes of the signals and the full width at half maximum (FWHM), nature of splitting of outer peaks and its dependence on temperature, transition temperature in line width *vs* temperature curve and its behaviour with respect to temperature, E_a and τ_{c0} values, ionic diffusion path (channel structure), and the behaviour of relaxation data with respect to temperature are affected. The three important aspects of these, *viz.*, rigid lattice state to liquid-like state transition temperature, dependence of splitting of outer peaks and occurrence of $T_{1\rho}$ minimum show that layered $HMWO_6 1.5\ H_2O$ are better ionic conductors than cubic $HMWO_6.H_2O$.

Participation of both the types of protons of $HNbWO_6.H_2O$ is also supported by MASS results.

4. NMR studies of hydrated ammonium ferrocyanide

The relaxation times T_2, T_1 and $T_{1\rho}$ are measured as a function of temperature and frequency. A double minimum was observed in T_1 *vs* 1000/T curve which is attributed to reorientational motion of the two different ammonium groups (at *g* and *b* sites). Another important feature is the indication of $T_{1\rho}$ minimum around room temperature. However, the fact that $T_{1\rho}$ minimum seems to occur at a higher temperature than that of the T_1 minimum indicates that the T_1 and $T_{1\rho}$ relaxations have different origins. We associate $T_{1\rho}$ relaxation with translational motion and T_1 with reorientational motion of the ammonium groups[7]. The results are consistent with those of earlier detailed studies on the compound[8–10].

5. NMR studies of $HLa_2NbTi_2O_{10}.1.5\ H_2O$

$HLa_2NbTi_2O_{10}.1.5\ H_2O$ is a newly synthesized layered oxide. This compound has been prepared by means of ion exchange and consists of three octahedra thick pervoskite slabs of $La_2NbTi_2O_{10}$ interleaved by proton and water molecules. Proton NMR results of this system are very similar to those of layered $HMWO_6.1\ 5\ H_2O$. Since in this system the vacancies are found in the plane, ionic motion takes place in two dimensions. Temperature dependent-relaxation data show the kind of behaviour expected from the structural viewpoint (2D character). It indicates that vacancy-assisted protonic jump is the mechanism for

2D diffusion in such perovskite oxides. MASS results also provide evidence for the participation of two types of protons from separate entities in this compound. A brief discussion on the exchange of protons, based on MASS results, has also been provided.

6. Conclusion

The drastic differences observed in the temperature dependences of the ^1H NMR linewidths in 2- and 3-dimensional analogues of the same compound bring out the importance of low-dimensionality effects in the NMR of fast ionic conductors. However, an analysis of the motional parameters of the 3-dimensional substances points towards additional contributions affecting the NMR behaviour.

References

1. Boyce, J. B. and Huberman, B. A. — *Phys. Rep.*, 1979, **51**, 189–265.
2. Bjorkstam, J. L. and Villa, M. — *Magn. Resonance Rev.*, 1980, **6**, 1–57.
3. Bloembergen, N., Purcell, E. M. and Pound, R. V. — *Phys. Rev.*, 1948, **73**, 679–712.
4. Slade, R. C. T. — *Solid St. Commun.*, 1985, **54**, 1035–1038
5. Colluroy, B., Mangamma, G. and Bhat, S. V. — *Pramana*, 1988, **31**, 51–57
6. Mangamma, G., Balakrishnan, N. and Bhat, S.V. — *J. Phys. E., Sci. Instrum.*, 1987, **20**, 100-101
7. Mangamma, G. and Bhat, S. V. — *Solid St. Ionics*, 1989, **35**, 123–125.
8. Balasubramanyan, D. R. and Bhat, S. V. — *Solid St. Ionics*, 1987, **23**, 267–270.
9. Balasubramanyan, D. R., Bhat, S. V., Mohan, M. and Singh A. K. — *Solid St. Ionics*, 1988, **28–30**, 664–667.
10. Balasubramanyan, D. R. and Bhat, S. V. — *J. Phys., Condensed Matter*, 1989, **1**, 1495-1502

Thesis Abstract (M.Sc. (Engng))

Study and development of four commonly used temperature indicators for industrial temperature instrumentation by C. Rameshu

Research supervisor: A. P. Shivaprasad
Department: Electrical Communication Engineering

1. Introduction

Temperature indicators have important role to play in many areas of electronic instrumentation in research and industry, especially in the field of measurement and control of process parameters. Temperature range of interest for many areas, *viz.*, cryogenic, meteorology, agriculture, environmental engineering, medical, domestic and industrial is wide, and may vary from −200 to 3726.85°C[1]. The accuracy required may be 5°C at higher temperatures, and 0.1°C or even 0.01°C in some other particular applications. Hence, accurate measurement of temperature is an important aspect of the industrial world today. Although a variety of temperature indicators for measurement of temperature are avialable in a wide range of configurations, their sensitivity, accuracy, repeatability and range of operation are limited. Therefore, development of precision temperature indicators for a specific application requires proper temperature transducers, stable signal conditioners, high-resolution analog interfaces and efficient software for linearization. Hence

the aim of the study is to develop precision temperature indicators based on commonly available temperature transducers, *viz* , thermistor, platinum, copper and thermocouples to meet the above needs.

2. Experimental work and results

The following is a brief summary of the study and development carried out on the four commonly used temperature indicators.

Thermistors are often preferred to other temperature transducers because of their low cost and high sensitivity. However, the resistance–temperature relationship of thermistors is highly nonlinear. Hence, using Hewlett Packard's thermistor equation[2], two temperature indicators were developed. In the first indicator, the temperature-sensing circuit produces a voltage which is proportional to the thermistor resistance. The delay-based voltage-controlled oscillator converts the temperature-dependent voltage to a square wave in a logic-compatible form of frequencies that are accurately proportional to the temperature. A 4-digit counter and display system measures the temperature-dependent frequency and reads the temperature directly. In the second indicator, the analog-interfacing module generates a square-wave signal of variable frequency and its ontime interval is measured by counting of a standard clock frequency in a standard 8253 counter. The 8085 microcomputer displays the temperature in °C after solving the thermistor equation. Both the indicators offer a linear performance over a wide temparature range of 0 to 100°C with an accuracy of ±0.1°C

Platinum-resistance temperature sensors are often used in ultra-high accuracy applications because of their greater stability and wide temperature range of operation. Keeping this in mind, a temperature indicator using platinum as sensor was developed. In this indicator, the temperature-sensing circuit generates a voltage which is directly proportional to the platinum resistance and is free from the lead resistances of the platinum probe. The temperature-dependent voltage is amplified in a drift-free dc amplifier[3] and is converted into digital using a 12-bit integrating ADC The 8085 microcomputer computes the temperature in °C after solving the Callendar–Van Dusen equation[4]. This indicator provides a linear performance over a wide dynamic temperature range of −183° to +200°C with an accuracy of better than ±0.05°C.

Thermocouple sensors cost less and can measure temperatures over a wide range. With this in view, a temperature indicator using the thermocouple as the sensor was developed. In this indicator, a low-level solid-state relay-based flying-capacitor multiplexer[5] in conjunction with a drift-free dc amplifier is used to extract millivolt signals[6] of the thermocouple from a high common-mode voltage (0 to ±300V peak). The amplified signal is converted into digital signals using a 12-bit integrating ADC. Linearization of the thermocouple is performed using a segmented fourth-order polynomial curve-fit algorithm in the 8085 microcomputer. For a K-type thermocouple, this indicator offers a linear performance over a wide dynamic temperature range of 50 to 1000°C with an accuracy of better than ±0.3°C.

A low-cost printed copper-resistance thermometer for the measurement of air temperature was developed. In this thermometer, a printed copper-resistance probe was constructed using a general-purpose double-sided glass-epoxy copper-clad laminate[7]. The copper layers on both sides of the probe were protected. The temperature-sensing circuit generates a voltage which is directly proportional to the copper resistance and is free from the lead resistances of the probe. The temperature-dependent voltage is amplified in a drift-free dc amplifier and displayed in the digital panel meter (DPM). Without linearization, this system offers a response linearity with a peak error of about ±0.3°C over a 0–100°C range.

A single precision binary floating-point arithmetic package[8] for an Intel 8085 microprocessor was developed and used for linearizing responses of RTDs (thermistor and platinum) and thermocouples. The algorithms[9], flowcharts and opcode listing for commonly used floating-point arithmetic routines are detailed. Using cubic splines and the least-square techniques[10], a method for determining the fourth-order polynomial coefficients for the given curve (or data) is presented with a Basic program suitable to HP-85 computer.

3. Conclusion

In this study, methods of linearization, design of signal conditioners and analog interfaces have been

proposed and implemented successfully to measure temperature precisely to give the required accuracy using transducers, viz., thermistor, platinum, thermocouples and copper. In these methods, high degree of accuracy and repeatability in the measurement of temperature have been achieved by solving exact function of the transducer in 8085 microcomputer with the help of floating-point routines specially developed for this purpose. Thus, the temperature indicators presented in this work establish their superiority over all other indicators reported in the literature and, therefore, should prove more attractive in applications where an accurate and precise measurement of temperature using the commonly available temperature transducers is required.

References

1. MAYES, V — Temperature scales: Let's think again, *Instn Measurement Control*, 1984, **17**, 169–176
2. — *Practical temperature measurement*, Application Note No 290, 1983, Hewlett Packard, USA
3. DAUPHINEE, T M — *In situ* conductivity measurements using low frequency square wave AC, *ISA Mar. Sci Instrum.*, 1968, **4**, 555.
4. NORTON, H N — *Sensor and analyser handbook*, Ch 4, 1982, Prentice Hall.
5. CONNORS, S — Protect data-acquisition systems with the right input isolation, *Electronics*, 1980, **53**, 134–141.
6. — *Temperature measurement handbook and encyclopedia*, 1984, pp. T-42/43, Omega Engineering, Stanford, Connecticut
7. BOSSHART, W.C — *Printed circuit boards–Design and technology*, 1983, pp. 17–32 and 199–224, Tata McGraw-Hill.
8. HASHIZUME, B. — Floating-point arithmetic, *Byte*, 1977, **2**, 76–78 and 180–188.
9. ABRAMOWITZ, M., *et al* — *Handbook of mathematical functions*, 1972, Dover
10. GERALD, C F. — *Applied numerical analysis*, 1977, Ch.10, pp. 465–504, Addison-Wesley.

Thesis Abstract (Ph.D.)

An experimental study of the specific heat at the glass transition during cooling by M. Rajeswari

Research supervisor: Arup Kumar Raychaudhuri
Department: Physics

1. Introduction

Glass transition is manifested in calorimetric studies as an abrupt step-like fall in the specific heat associated with the arrest of the configurational degrees of freedom which occurs when the time scale of the structural relaxation becomes comparable to the time scale of observation. Hence, the study of specific heat is instrumental in understanding the structural relaxation processes and also in probing the possible relation of the calorimetric transition to underlying phase transitions, if any. Earlier studies of the glass transition employing differential scanning calorimetry (DSC) and adiabatic calorimetry[1,2] have been done during the reheating of a quenched glass. The frozen-in enthalpy of the nonequilibrium starting state affects the observed specific heat during reheating[3] and also complicates the analysis of the data. On the other hand, when the specific heat is measured during cooling through the glass transition we can ensure a thermodynamically well-defined initial state. The specific heat observed in such an experiment would be more directly representative of the enthalpy relaxation at the glass transition. The work presented was largely motivated by the above idea. The results clearly point to a nontrivial distinction between the specific heat measured during cooling and that obtained during the heating of a quenched glass. In this work, the behavior of the specific heat at the glass transition has been studied in several organic glass

formers as the supercooled liquid freezes into the glassy state starting from an equilibrium state at a temperature well above the glass transition range.

2. Experimental technique

Specific heat was measured employing continuous cooling calorimetry[4] which is a derivative of the relaxation calorimetry[5]. This technique was developed during the course of the work The sample is thermally linked to a heat reservoir at liquid nitrogen temperature. The specific heat is derived from the cooling rate of the sample as it cools through the heat link of known heat loss rate. The work presented here establishes this technique to be a versatile tool for the quantitative calorimetric study of the glass transition.

3. Results

(i) The specific heat of five organic glass formers—glycerol, propylene glycol, amyl alcohol, propylene carbonate and diethyl phthallate—has been studied in temperature ranges covering the supercooled liquid state, the glass transition interval and the glassy state. Specific heat is measured as the supercooled liquid cools from a well-annealed quasi-equilibrium state at a temperature $T > T_g$ The data in the supercooled liquid state and the glassy state are in reasonable agreement with the earlier data obtained during heating in the adiabatic calorimetry and DSC experiments. The glass transition range however shows significant differences reflecting the sensitivity of the relaxational part of the specific heat to the experimental kinetics.

(ii) A phenomenological model of the kinetics of enthalpy relaxation has been developed for the analysis of the specific heat data. This model incorporates the non-equilibrium nature of the relaxation time through its dependence on the excess enthalpy of the system. The effect of delayed heat release on the observed specific heat is also considered. The relevant parameters which describe the enthalpy relaxation has been obtained in the framework of this model. The analysis suggests an equilibrium configurational specific heat which increases with temperature suggesting a purely kinetic origin of the specific heat step at the glass transition. Another important observation is the departure from the Vogel–Fulcher law as indicated by the fact that to fit the experimental data, we need to assume in the model, a temperature-dependent parameter T_0 in the relation $\tau = \tau_0 \exp(A/(T-T_0))$.

(iii) Another aspect studied is the effect of partial crystallisation on the observed specific heat at the glass transition. These experiments were designed to investigate the effect of partial crystallisation on the structural relaxation of the residual vitreous phase. They have been conducted in two systems—glycerol and propylene carbonate. In the case of glycerol, we find that the width of the glass transition interval varies with the degree of partial crystallisation. This suggests that the width of the relaxation spectrum is altered which may be associated with the heterogenities in the system due to nucleation of the crystallites. Such heterogenities may affect the relaxation process when their scales become comparable to the length scales of molecular rearrangements.

(iv) The dependence of the observed specific heat on the rate of cooling has also been studied. The results indicate that slower cooling leads to a lower value of the observed specific heat. Analysis of the cooling rate dependence in the framework of the enthalpy relaxation model suggests that the above observation cannot be explained solely through the kinetic effects of varying the experimental time scale. The observed cooling rate dependence could arise from the dependence of the observed specific heat on the configurational state of the system.

(v) Another study presented in this work is the behavior of the specific heat on thermal cycling through glass transition. The specific heat observed in the thermal cycling experiments show an anomalous dip below the glass-transition temperature. This dip has been observed for all the samples studied. In the specific heat it has not been observed in the earlier heating experiments where the initial state before cooling is an equilibrium state. The occurrence of the dip is thus exclusive to the thermal cycling experiments. Detailed experiments on the dependence of this anomaly on thermal history and experimental kinetics suggest that this may have its origin in memory effects related to a broad distribution of relaxation times.

4. Scope of future work

(i) Partial crystallisation experiments merit further experimentation. It would be interesting to see whether the broadening of the relaxation spectrum is also seen in ac-specific heat measurements on partially crystallised glasses. The effect of partial crystallisation on the relaxation spectrum may also be investigated in other experiments like dielectric relaxation and ultrasonic attenuation. It would be interesting to look into the relaxation behavior at the late stages of crystallisation to see if it is related to any size-limited effects. For higher crystal fractions the supercooled liquid phase would be confined to small pockets of the crystalline matrix and we may expect size-limited behavior in the relaxational response.

(ii) The origin of the anomaly in the thermal cycling experiments is to be understood in the framework of a rigorous model of the thermal cycling process. It would be interesting to see if the anomaly occurs in other glass formers (*e.g.*, inorganic glasses) where glass transition occurs at higher temperatures.

References

1 CHANG, S.S AND BESTUL, A B — *J Chem. Phys*, 1974, **56**, 503–508.

2 MOYNIHAN, C.T *et al* — *J Am Cerum Soc*, 1976, **59**, 12–16

3. THOMAS, S B AND PARKS, G S. — *J Phys. Chem.*, 1931, **35**, 2091–2095.

4. RAJESWARI, M , RAMASESHA, S K. AND RAYCHAUDHURI, A.K — *J Phys E*, 1988, **21**, 1017–1022

5 BACHMANN, R *et al* — *Rev Sci Instrum.*, 1972, **43**, 205–214.

Thesis Abstract (Ph.D.)

Quantum corrections in a disordered electronic system: A low temperature study of the perovskite oxide $LaNi_{1-x}Co_xO_3$ by K. P. Rajeev

Research supervisor: A. K. Raychaudhuri

Department: Physics

1. Introduction

The Boltzmann theory of transport in metals is valid only when the electron wavelength (λ) is much less than the electron mean free path (l). It is assumed that the electron follows a classical trajectory in between two collisions. But when λ becomes comparable to l, as a result of increased disorder, electron waves can interfere and this leads to weak or strong localization. The advent of scaling theory of localization[1] marked a watershed in the understanding of this phenomenon. This theory made quantitative predictions for electronic transport which were tested experimentally in a number of different systems.

As the electrons tend to localize resulting in a decrease in their diffusivity, the screening of the electron–electron Coulomb interaction between electrons becomes less effective. This leads to quantum corrections to the conductivity of disordered systems which are observable at low temperatures[2,3]. The interaction effects also give corrections to thermodynamic quantities as well as single particle electron density of states. The above effects have been seen in a number of materials, for instance, heavily doped semiconductors are metallic glasses.

The above discussion puts the present investigation in proper perspective We carried out low temperature investigations on a perovskite oxide system well inside the metallic regime as well as near the M-I transition. The purpose of this investigation is to see the behavior of these types of electronic systems at low temperatures and to explore to what extent the present theories are applicable to them.

Metal-insulator transition in perovskite oxides has been studied earlier[4,5]. But only in a few cases have the experiments been carried out at low enough temperatures where the quantum corrections can be unambiguously seen[6-8]. In particular, to our knowledge, a comprehensive investigation involving

conductivity, magnetoconductance and tunneling conductance have never been carried out. These oxides with a large carrier concentration (10^{21}–10^{22}/cm^3) and low diffusivity (0.01–0.1 cm^2/s) form a rather unique class of systems where it is expected that the interaction effects will play a very significant role. Our investigation supports this view. Investigations on normal conducting perovskite oxides have also a special significance in view of the discovery of high-temperature superconductivity in this class of materials.

We chose the perovskite oxide system $LaNi_{1-x}Co_xO_3$ for this study. The compound $LaNiO_3$ is a metal with properties very similar to the normal state properties of the high T_c oxide $YBa_2Cu_3O_7$. On the other hand, $LaCoO_3$ is an insulator. The compounds are isostructural and they make a polycrystalline solid solution for $0 < x < 1$. The system is metallic for $x \leq 0.65$ and it shows quantum corrections to various quantities starting right from $x = 0$. Our emphasis was on transport measurements—electrical conductivity, magnetoconductance, and tunneling conductance. The present investigation allowed us to reach quite a few interesting conclusions some of which are presented here.

2. The metallic oxide $LaNiO_3$

Even the pure oxide metal $LaNiO_3$ has sufficient disorder built into it, that it shows a low-temperature maximum in conductivity at $\sim$ 10K and below this temperature $\sigma(T) \propto \sqrt{T}$ + const. A square root singularity, at zero bias, has also been observed in the tunneling conductance at low temperatures. These behaviors are attributed to enhanced electron–electron interaction in the system arising from disorder. Surprisingly, one has a thermopower which is negative—indicating electrons as charge carriers—and linear with temperature, which is the behavior expected of a good metal. The free electron picture gives for this metal an $E_F = 0.21$ eV which leads to an $m_{eff} = 11m_e$ (assuming one carrier per primitive cell) where m_e is the bare electron mass. It is of interest to note that the effective mass estimated from the linear part of specific heat ($= 10m_e$) at low temperatures closely agrees with the one estimated from thermopower.

3. Electrical conductivity

The electrical conductivity of $LaNi_{1-x}Co_xO_3$ has been studied in the temperature range $0.1K < T < 300K$ For all x, at low temperatures the conductivity (σ) rises with temperature (T) Below 2K, σ follows the power law behavior $\sigma(T) = \sigma(0) + aT^m$ with $m \approx 0.3$ for samples deep in the metallic regime ($x \leq 0.4$). As the M–I transition is approached m begins to increase and is ≈ 1 at the transition† ($x \approx 0.65$) and thereafter continues to rise much faster. Earlier studies by others[2,3] on disordered metals usually found that $m = 0.5$, and it was attributed to enhanced electron–electron interaction in the presence of disorder. The behavior we see can be explained as arising from electron–electron interaction by taking into account the diffusion channel contribution (which gives $m = 0.5$) as well as the Cooper channel contribution. The Cooper channel contribution, though predicted, has never been observed in non-superconducting disordered metals. The observation of this term is an important finding of this investigation. We fit the conductivity in the range 0.1 to 10 K to the sum of terms mentioned above and a weak localization term. The fit parameters are found to be reasonable. From the weak localization term we conclude that the dominant phase-breaking mechanism in these materials is electron–electron scattering. Near the M–I transition, where one has stronger localization tendency and interaction, the situation is more difficult. We were unable to find any proper explanation for the observations in this regime. We also take note of the fact that for a large range of x ($0.25 < x < 0.65$) the conductivity of the system remains below the Mott minimum metallic conductivity.

4. Magnetoconductance

The magnetoconductance measurements on the system were done in the magnetic field range $0 < x < 7T$ and the temperature range $1.5K < T < 90K$. The system is found to have a positive magnetoconductance for all the fields, temperatures and compositions ($0.25 < x < 0.65$) studied. In the weakly localized

†The M–I transition is determined by the rule that $\sigma(T=0)=0$ at the transition Earlier studies used the 'wrong' rule of the change of sign of TCR—temperature coefficient of resistivity—to determine transition point.

metallic regime it is found that the magnetoconductance increases as the temperature is lowered, and saturates below 4K. We explain the positive magnetoconductance as arising mainly from the destruction of weak localization by the magnetic field. The low-temperature saturation shows that the phase-breaking rate (τ_φ^{-1}) tends to a limiting constant value at low temperatures. Near the M–I transition we also see that the magnetoresistance $\propto$ B/T which could be a signature of moment formation in the system.

5. Tunneling conductance

The tunneling conductance measurements were done with various counter electrodes, *viz.*, tungsten, niobium, silver and lead at temperatures ranging from 0.4 to 4.1K. The main observation is a cusp-like (essentially square root) dip in the tunneling conductance at zero bias It is found that as x is increased the dip becomes deeper and eventually on the insulating side of a Coulomb gap opens up with the density of states showing a parabolic behavior. It is known that the tunneling conductance reflects the behavior of the single particle density of states of the system and the theory predicts a behavior similar to that we see in our system.

6. Conclusions

To summarize: We see interaction and weak localization effects on the metallic side. For a large range of x we have $\alpha < \alpha_{min}$ which could mean that we have a continuous transition For the first time, we have seen the effect of Cooper channel interaction in conductivity. Near the M–I transition the results are too complex to be explained with our present-day understanding of disordered electronic systems.

References

1 ABRAHAMS, E., ANDERSON, P.W LICCIARDELLO, D C. AND RAMAKRISHNAN, T V. — *Phys. Rev. Lett.*, 1979, **42**, 673–676.

2. ALTSHULER, B L AND ARONOV, A.G — In *Electron–electron interactions in disordered systems* (A.L. Efros and M. Pollak, eds) 1985, North Holland.

3. LEE, P A AND RAMAKRISHNAN, T.V. — *Rev. Mod. Phys.*, 1985, **57**, 287–337.

4 EDWARDS, P.P. AND RAO, C.N R. — *Metallic and non-metallic states of matter*, 1985, Taylor and Francis.

5 VASANTHACHARYA, N Y. — *Investigations of metal-insulatory transitions in the Perovskite oxide system $LaNi_{1-x}B_xO_3$(B=Cr,Mn, Fe or (O))*, Ph.D Thesis, Indian Institute of Science, Bangalore, 1985.

6. RAJEEV, K.P., VASANTHACHARYA, N.Y., RAYCHAUDHURI, A.K AND GANGULY, P. — *Physica C*, 1988, **153–155**, 1331–1332

7. RAJEEV, K.P , SHIVASHANKAR, G V. AND RAYCHAUDHURI, A.K. — *Solid St. Commun* , 1991, **79**, 591–595.

8 RAYCHAUDHURI, A.K. — *Phys. Rev B*, 1991–II, **44**, 8572–8577.

Thesis Abstract (Ph.D.)

Electrical conductivity of the complexes obtained from 1,4-diamino anthraquinone and of the pyrolytic carbon films by M. N. Vijayashree

Research supervisor: S. V. Subramanyam
Department: Physics

1. Introduction

Anthraquinone dyes have been the most important single class of dyes for a long time. 1,4-Diaminoanthra-

quinone is an anthracene derivative with molecular formula $C_{14}H_{10}N_2O_2$. This is a violet crystalline powder with a donor NH_2 and an acceptor C=O groups. Introduction of less-reactive species into the conducting pathway which can exhibit multiple oxidation states produces a stable, intrinsically conducting complex. Conducting coordination oligomers are synthesised by oxidising 1,4-diaminoanthraquinone with different metal ions. Different metal complexes obtained are of Fe^{2+}, Co^{2+}, Ni^{2+}, Cu^{2+}, Ag^{+}, and Pt^{4+}. Conducting complexes obtained are highly stable, insoluble and infusible polycrystalline powders with a room temperature conductivity varying from 1×10^{1} to 1×10^{4} S/cm depending on the metal atom present in the system.

2. Experimental

Low-temperature conductivity measurements are studied through four-probe (Vanderpauw) method. The powders of the conducting complex are pressed into 8-mm diameter pellets at 4kbar pressure, and contacts are made with silver paste. A bath-type cryostat made as part of instrumentation section of this work has been used to study conducting properties in the temperature interval 300–77K. A commercial JANIS SUPERVARIEXP helium cryostat has been used for low-temperature conductivity measurements below 77K down to 1.4K.

High-pressure studies up to 8GPa have been carried out on the above conducting complexes. A 4mm-tip diameter Bridgman anvil set-up has been fabricated and used for these types of measurements. The set-up has the facility of locking the system at desired pressures to study low-temperature conducting properties at different pressures.

3. Discussion

Low-temperature studies of these complexes reveal that the conductivity mechanism in these complexes is of variable range hopping type, where the resistivity varies as $T^{-0.25}$ (lnR a $T^{-1/4}$). Electrical conductivity in these complexes is attributed to the overlapping of d-orbitals of the metal atom with p-orbitals of aromatic ring. Copper which favors square planar coordination exhibits relatively high conductivity. The amount of copper present in the system also contributes to the conductivity. Complex with 22.2% of copper exhibits relatively high conductivity (0.198 S/cm). A donor–acceptor-type conducting complex is formed when 1,4-diaminoanthraquinone is oxidised with ceric ammonium nitrate salt. Cerium is completely absent in the complex formed. This complex has a conductivity in the range of the coordination complex formed with copper, where its percentage is 22.2. This is the first relatively high-conducting complex obtained with 1,4-diaminoanthraquinone without metal. Low-temperature-conducting properties of this complex takes deviation from $T^{-1/4}$ law. The resistivity varies as $T^{-1/2}$. This type of behavior is attributed to the Coulomb interaction between electrons of the stacks.

Another system that has been studied as part of this work is conducting carbon film, obtained through pyrolysis of the 3,4,9,10-perylenetetracarboxylic anhydride dye powder[1]. The film conductivity varies from 2.25 to 126 S/cm depending on the pyrolysis temperature. The film formed at 700–800°C has a room temperature conductivity of 2.25 S/cm. Resistivity variation is of the form exp ($T^{-0.25}$). The film formed at temperature 900–1000°C exhibits very interesting temperature-independent conducting property. This film shows no change in resistivity over a wide range of temperature, from 600K down to 1.4K. Magnetic fields applied up to 7 Tesla at different temperatures do not have any effect on the resistivity of the film. The high conductivity of this intrinsically carbon backbone system and its temperature-independent conductivity makes this system very interesting.

As all the monomer units are converted into polymer, the conjugation length becomes very large and hence the conductivity is very high. Thus, the gross feature seems to indicate a delocalised charge transport, and the scattering mechanisms do not seem to be affected by temperature.

Reference

1. VIJAYASHREE, M.N. AND SUBRAMANYAM, S.V. *Solid St. Commun.*, 1991, **79**, 629–630

Thesis Abstract (Ph.D.)

Investigations of superconducting thallium and bismuth cuprates and related oxide materials by R. Vijayaraghavan
Research supervisor: C.N.R. Rao
Department: Solid State and Structural Chemistry Unit

1. Introduction

A number of simple and complex metal oxides exhibit interesting electronic and magnetic properties besides novel structural features[1,2]. A few oxides of the transition metal ions show superconductivity at very low temperatures[3]. After the discovery of high T_c superconductivity in the La–Ba–Cu–O system in late 1986[4] several families of oxides exhibiting superconductivity near liquid nitrogen temperature have been synthesized and characterized[5] The structural features associated with these oxides are rather traditional in solid-state chemistry and have been extensively studied[6,7]. We have carried out detailed investigations of the thallium and bismuth cuprates with a view to obtain certain structure–property correlations. A variety of techniques such as powder x-ray diffraction, high-resolution XRD, neutron diffraction, electron microscopy, x-ray absorption spectroscopy, electrical resistivity, magnetic susceptibility, thermopower measurements and non-resonant microwave absorption have been used for the characterization of the materials.

2. Experimental

The superconducting cuprates are generally prepared by the usual ceramic method. But due to the toxicity and volatility of thallium oxide, the usual ceramic method was modified and the synthesis of the thallium cuprates was carried out in closed reaction systems. The mixture of the component oxides made in the form of pellets is sealed in a silver or quartz tube (pellet wrapped in Pt or Au foil) and then heated at appropriate conditions.

Powder x-ray diffractions were recorded with a JEOL JDX-8P diffractometer and the high-resolution x-ray diffraction data were collected with a STOE automatic diffractometer. Neutron diffraction patterns were recorded at the 10 MW reactor at Trombay, India. Electron microscopy studies were carried out using a JEOL JEM CX electron microscope in the top entry configuration. Electrical resistivity measurements were carried out by Four-probe method with silver paste contacts. DC magnetic susceptibility studies were carried out with a Lewis coil magnetometer (model 305) in the temperature range 20–300K. Thermoelectric power was measured using a differential technique with a home-built apparatus. X-ray absorption spectra were recorded with a Rigaku spectrometer with a 12 kW rotating anode x-ray generator. X-ray Photoelectron studies (XPS) were carried out on ESCA III Mark 2 spectrometer of VG Scientific. Non-resonant microwave absorption was carried on using a Varian E-109 X-band EPR spectrometer operating at a frequency of 9–11 GHz.

The hole concentration, n_h, in the thallium cuprates was estimated by a chemical titration method based on the finding that Br^- is selectively oxidized by holes in the CuO_2 sheets and not by thallium (III).

3. Results and discussion

A variety of thallium cuprates of the general formula $TlCaA_2Cu_2O_7$ (A=Sr,Ba) have been extensively studied with a view to obtain certain structure–property correlation The systems discussed include thallium-deficient cuprates of the formulae $Tl_{1-\delta}CaBa_2Cu_2O_7$ and $Tl_{1-\delta}Y_{1-x}Ca_xBa_2Cu_2O_7$, lead-doped cuprates of the formula $Tl_{1-x}Pb_xCaSr_2Cu_2O_7$, rare-earth (Ln)-substituted cuprates of the formula $TlLn_{1-x}Ca_xSr_2Cu_2O_7$ and the $Tl_{1-y}Pb_yY_{1-x}Ca_xSr_2Cu_2O_7$ system. Lastly, thallium cuprates containing fluorite-type layers of the formula $Tl_{0.5}Pb_{0.5}(Ln_{1-x}Ce_x)_2Sr_2Cu_2O_9$ have also been examined. A study of the $Tl_{1-\delta}CaBa_2Cu_2O_7$ and $Tl_{1-\delta}Y_{1-x}CA_xBa_2CU_2O_7$ systems has shown that superconducting $Tl_{1-\delta}CaBa_2Cu_2O_7$ can be prepared without the impurity of the corresponding double Tl–O layered cuprate only when some thallium-deficiency is incorporated[8]. Furthermore, thallium-deficiency seems to act as a source of holes. A relation between the transition temperature, T_c, and the hole concentration, n_h, similar to the one found for other cuprates has been shown to exist in the superconducting thallium cuprates.

In the Tl–Ca–Sr–Cu–O system, either substitution of Tl by Pb or of Ca by a rare earth (Ln) is essential for the stabilization of the 1122 phase. The T_c attains a maximum at an optimal composition.

Since it is not straightforward to determine n_h in the thallium cuprates, we have investigated the $Tl_{1-y}Pb_yY_{1-x}Ca_xSr_2Cu_2O_7$ system[9] which is suitably designed for the study of the dependence of superconductivity on n_h. In the above system, since Tl is in the 3+ state and Pb in the 4+ state, substitution of Tl^{3+} by Pb^{4+} introduces electrons while the substitution of Y^{3+} by Ca^{2+} introduces holes. The study has shown that the T_c depends sensitively on both x and y, showing a maximum at specific value of x, depending on the value of y. More interestingly, T_c shows a maximum at an optimal hole concentration as measured by the $(x-y)$ value. This value at the highest T_c being in the range 0.20–0.25. A study of the $Tl_{0.5}Pb_{0.5}(Ln_{1-x}Ce_x)_2Sr_2Cu_2O_9$ has shown that a fluorite unit can be intergrown with perovskite and rock-salt type layers in thallium cuprates. In all these thallium cuprates the maximum in T_c occurs at a certain in-plane Cu–O distance (r_{Cu-O}).

Investigations of the bismuth cuprates have revealed that the $n = 2$ member is the most stable phase among the bismuth cuprates represented by the general formula $Bi_2(Ca, Sr)_{n+1}Cu_nO_{2n+y}$ and substitution of Bi by Pb in these cuprates has enabled us to obtain the $n = 4$ member for the first time[10]. The T_c values of the $n = 2,3$ and 4 members are ~ 85, ~ 105 and ~ 110K, respectively. The T_c increases with the number of CuO_2 sheets up to $n = 3$. The study on the $Bi_2Ca_{1-x}Yb_xSr_2Cu_2O_{8+\delta}$ has shown that superconductivity is observed only in the range $0 \leq x \leq 0.50$ and the T_c value reaches a maximum around $x = 0.25$. At this composition, the hole concentration, n_h is also maximum with a value of ~ 0.20

Lastly, the study of $La_{4-x}Ba_{1+x}Cu_5O_{13+\delta}$ and $La_3LnBaCu_5O_{13+\delta}$ has shown that changes in the oxygen stoichiometry or the La:Ba ratio bring about metal insulator transition in these systems

References

1. RAO, C.N.R AND GOPALAKRISHNAN, J — *New directions in solid state chemistry*, 1986, Cambridge Solid State Science Series, Cambridge University Press.
2. RAO, C.N.R. — *A. Rev Phys. Chem.*, 1989, **40**, 291–326
3. SLEIGHT, A W. — *Science*, 1990, **247**, 656–667.
4. BEDNORZ, J G. AND MULLER, K A. — *Z. Phys. B*, 1986, **64**, 189–192.
5. RAO, C.N R. (ed) — *Chemistry of high temperature superconductors*, 1991, World Scientific.
6. RAO, C.N.R. — *Phil. Trans. R. Soc. Lond. A*, 1991, **336**, 595–607
7. RAO, C N.R. AND RAVEAU, B — *Acc Chem Res*, 1989, **22**, 106–113
8. VIJAYARAGHAVAN, R., GOPALAKRISHNAN, J AND RAO, C.N.R. — *J. Mater. Chem*, 1992, **2**, 327–330.
9. VIJAYARAGHAVAN, R., RANGAVITTAL, N., KULKARNI, G.U., GRANTSCHAROVA, E., GURU ROW, T.N. AND RAO, C N R. — *Physica C*, 1991, **179**, 183–190.
10. RAO, C.N.R., VIJAYARAGHAVAN, R., GANAPATHI, L AND BHAT, S V. — *J. Solid St. Chem*, 1989, **79**, 177–181.

Thesis Abstract (Ph.D.)

Theoretical and experimental investigations of nuclear Overhauser effect in nuclear magnetic resonance by V. V. Krishnan
Research supervisor: Anil Kumar
Department: Physics

1. Introduction

"One of the remarkable features of magnetic resonance is the very close connection between theory and experiment that leaves little room for a theory that could not be tested by a suitable experiment or for an experiment that does not admit of a well defined theoretical interpretation". What Abragam said three decades ago in his monograph *Principles of nuclear magnetism*[1] continues to be true in the field of nuclear magnetic resonance spectroscopy (NMR) even today. Developments in the theoretical tools and experimental techniques in the past fifteen years have made NMR spectroscopy an indispensable part of modern physics[2]. Improvements in methodology, instrumentation and data analysis, developed over these years, have made this branch of spectroscopy a unique spectroscopy to understand the structure and dynamics of molecules in the liquid state[3].

The structural information in NMR is obtained by Nuclear Overhauser effect, a cross-relaxation process *via* dipole–dipole interaction among the nuclear spins. This work investigates the details of the nuclear Overhauser effect (NOE) in homonuclear (portons) spin systems. An investigation of the major assumptions in correlating the NOE to internuclear distances, and the experimental utility of the NOE in molecular conformation of polypeptides has been carried out.

A general description to one-and two-dimensional NMR spectroscopy is presented as an introduction. Equation of motion of the density operator is discussed in detail with a special emphasis on the evolution of spins under incoherent process causing relaxation of the nuclear spins by explicit Redfield formalism. The introduction also discusses the use of one- and two-dimensional NMR spectroscopy in structural conformation of polypeptides.

Since most of the discussion in this work is confined to the study of NOE, a description of cross-relaxation process and NOE in coupled spins is also presented in detail including two and multispin NOE calculations, flip-angle effects on a non-equilibrium state and the effect of leakage and motional processes in NOE spectra. A comparative study of the different methods of calculating the NOE is also presented.

2. A diffusion equation approach to spin diffusion in biomolecules

NOE between spins crucially depends on the motional process causing relaxation and internuclear distance between the spins[4,5]. The motional process is governed by a parameter $\omega\tau_c$, the product of Larmour frequency of the nucleus (ω) and the correlation time (τ_c) of the random motion. The homonuclear NOE among the protons is positive for molecules which reorients at a rate faster compared to the Larmour frequency and negative for those which reorient at a slower rate. For large molecules such as biomolecules like polypeptides and oligonucleotides, the latter situation often prevails and that regime of motion is commonly known as 'biomolecular limit'. Since in this limit the magnetization of a spin can migrate to long distance within the molecule by a hopping mechanism (through flip-flop process, B term of the dipolar interaction), resembling a diffusion process, it is also known as 'spin diffusion limit'. However, the process of spin diffusion was not described by a diffusion equation.

In this work, it is shown that a diffusion equation can indeed be formed from the first principles for a linear chain of equidistant spins to describe the magnetization transfer process in the spin diffusion limit[6]. The diffusion equation is solved for two different kinds of NOE experiments that differ in the nature of perturbation, namely, truncated-driven and transient NOE experiments[6,7].

3. Approximations revisited

The cross peak volumes in a NOESY experiment is often related to inverse sixth power of the distance between the spins (r^{-6}). However, such direct relationship is the outcome of some of the approximations in the theory of cross-relaxation. The major approximations may be classified into three groups within the regime of relaxation of nuclear spins in the liquid state, where the rotational Brownian motion induces the random time dependence on the spin variables. Those are (i) two-spin or initial slope approximation, (ii) the assumption that the rotational Brownian motion of the molecule is isotropic rotational diffusion, free of any internal motion and hence represented by a single correlation time, and (iii) neglecting the multispin effects leading to cross-correlation among the dipole–dipole vectors.

The isolated spin pair approximation can be lifted by a full relaxation matrix analysis, while the situations, when the second and third approximations, are not entirely valid has been studied in detail

3.1. Modulation of internuclear distances due to segmental motion

The second approximation, cross-relaxation between the spins of a molecule, in the presence of an additional internal motion is investigated in detail A model has been developed in which the overall motion is anisotropic reorientation and the internal motion modulates the internuclear distance. Analytical spectral density functions for dipole–dipole relaxation are obtained when the internal motion is a bistable jump[8] These results show that the NOE is directly proportional to the average of the inverse sixth power of the distances ($<r^{-6}>$) only when the overall motion is isotropic and faster compared to the internal motion These model-based NOE calculations have been utilized to explain the simultaneous observation of positive and negative NOE in the steady-state NOE experiments in a tryptophan-containing polypeptide.

3.2. Dipolar cross-correlation effects in the NOE spectra

The work then addresses the third approximation listed above, namely, the neglect of dipole–dipole cross-correlation effects in the cross-relaxation process. A systematic study for a system of three scalar coupled spins (weakly or strongly coupled) has been undertaken[9]. It is found that in the weakly coupled spin systems, the cross-correlation effects are limited to single quantum transition probabilities and when all X spin transitions are perturbed equally. It is found that for a resolved spectrum, the cross-correlation effects are significant in the transient NOE experiments of weakly as well as strongly coupled spin systems Cross-correlation manifests itself as a multiplet effect in the transient NOE of weakly coupled spins and disappears either for a measuring pulse of 90° or when the multiplets are not resolved. These effects are however analytically zero for steady-state NOE experiments of three weakly coupled spins in which all the transitions of one of the spins are continuously saturated all the time.

4. Molecular conformation of Leu–Zervamicin

The NOE experiments in combination with other one- and two-dimensional NMR experiments have been utilized for the determination of the secondary structure of a 16-residue, natural polypeptide Leu-Zervamicin[10]. Theoretical and experimental results on the flip-angle dependence of heteronuclear COSY experiment in a strongly coupled ABX spin system where A and B are the protons and X is carbon-13[11] are also discussed.

References

1. ABRAGAM, A — *Principles of nuclear magnetic resonance*, 1961, Oxford University Press
2. ERNST, R R., BODENHAUSEN, G. AND WOKAUN, A — *Principles of nuclear magnetic resonance in one or two dimensions*, 1986, Oxford University Press
3. WUTHRICH, K. — *NMR of proteins and nucleic acids*, 1986, Wiley
4. NOGGLE, J.H. AND SCHIRMER, R E — *The nuclear Overhauser effect. Chemical applications*, 1971, Academic Press.
5. NEUHAUS, D AND WILLIAMSON, M P — *The nuclear Overhauser effect in structural and conformational analysis*, 1989, VCH Publishers.
6. KRISHNAN, V.V , MURALI, N. AND ANIL KUMAR — *J Magn Reson.*, 1989, **84**, 255–267.
7. KRISHNAN, V.V , USHA HEGDE AND ANIL KUMAR — *J Magn Reson.*, 1991, **94**, 605–611.
8. KRISHNAN, V.V , SHEKAR, S.C. AND ANIL KUMAR — *J. Am. Chem. Sci* , 1991, **113**, 7542–7550
9. KRISHNAN, V.V. AND ANIL KUMAR — *J. Magn. Reson.*, 1991, **92**, 293–311
10. KRISHNAN, V.V., KRISHNA, K., ANIL KUMAR AND BALARAM, P — Molecular conformation of leucine zervamicin in solution using one- and two-dimensional NMR spectroscopy, presented at the *Indo-USSR Symp. on Magnetic Resonance* and in the book entitled *Magnetic resonance—Current trends* (Khetrapal, C.L. and Govil G., eds) 1991, Narosa-Springer.
11. KRISHNAN, V.V., RAGHOTHAMA, S. AND ANIL KUMAR — *J Magn Reson.*, 1988, **79**, 328–335.

Thesis Abstract (Ph.D.)

Magic-angle-spinning NMR spectroscopic investigations of gels and glasses of silicates, phosphates, borates and related systems by S. Prabakar
Research supervisors: K. J. Rao and C. N. R. Rao
Department: Solid State and Structural Chemistry Unit

1. Introduction

Magic-angle-spinning NMR has proved to be a powerful tool for the study of inorganic solids. The impact made by this technique on the studies of silicates, especially zeolites, is illustrative of the power of the technique[1,2]. The advantage of this technique lies in the fact that even the coordination of atoms having similar scattering powers like Si and Al which cannot be studied by scattering experiments can be studied easily. Also, this technique is very useful when single crystals of adequate size and perfection are not available. The most useful parameter derived from NMR experiments is the chemical shift. It can be related to the coordination number provided the chemical nature of the species is known. It is often possible to obtain information about the nearest and next nearest neighbours, bond lengths, bond angles, state of hybridization, etc. In this work, results of the investigations of the local structures of several series of silicate, phosphate and borate gels and glasses obtained by employing MAS ^{27}Al, ^{29}Si, ^{31}P and ^{11}B NMR spectroscopy are presented. The present investigations have yielded results which are very useful in understanding the structure of amorphous materials.

2. Experimental

The glasses reported here were prepared by melting appropriate amounts of the respective oxides or respective carbonates and oxides. The gels were prepared by hydrolysis and polycondensation of respective alkoxides or nitrates and alkoxides[2].

The NMR spectra were recorded with a Bruker MSL-300 solid-state high-resolution spectrometer operating at 59.621 MHz (for ^{29}Si), 78.206 MHz (for ^{27}Al), 121.491 MHz (for ^{31}P) and 96.293 (for ^{11}B). The magnetic field employed is 7.05T. A cylindrical rotor with a spinning speed of 3 kHz was used in MAS experiments. Chemical shifts were reported with respect to tetramethyl silane (for ^{29}Si), $Al(H_2O)_6$ (for ^{27}Al), 85% H_3PO_4 (for ^{31}P) and $BF_3.Et_2O$ (for ^{11}B). Appropriate time delays between pulses were applied to prevent saturation of individual resonances.

3. Results and discussion

The gel–glass–crystal transformation of several series of gels has been studied as a function of temperature and composition. Changes in the NMR spectra that occur as the gels are progressively heated have been examined to understand the nature of the structural changes occurring during the crystallization process. In pure SiO_2 gel, Si present as Q_4, Q_3 and Q_2 (Q represents silicon tetrahedrally bonded to oxygens and the subscript refers to the number of bridging oxygens connected to it) change over to Q_4 on heating. Finally, the gel–glass crystallizes to cristobalite. In the aluminosilicate gels, the hydroxyl groups tend to be located on the Al sites as the percentage of Al increases. Mullite is the major phase formed at high temperatures[2]. Silicon is present in Q_4 units in the aluminosilicate glasses; all the Q_n types except Q_0 are present in alkali aluminosilicate glasses. ^{27}Al NMR is very sensitive to the changes in coordination even when the concentration of aluminium is very low. Pure Al_2O_3 gel consists of octahedral Al in xerogel, both tetrahedral and octahedral Al at the intermediate temperatures and only octahedral Al at higher temperatures. In the aluminosilicate glasses, Al is present in four, five and six coordination whereas in the alkali aluminosilicate glasses as well as in Bi and Pb aluminosilicate glasses, only tetrahedral Al is present, the additional oxygen being provided by alkali oxide, PbO or Bi_2O_3[3,4].

In the silicophosphate gels, Si is present in both Q_4 and Q_3 species. There is a change in the coordination of Si from four to six when the gel crystallizes at higher temperatures. Phosphorous which is present as orthophosphoric acid units in the xerogels change over to metaphosphate-like units as the gel is heated to

higher temperatures In the aluminosilicophosphate gels, Si is present in Q_4 and Q_3 species while P is present as metaphosphate units; Al is in tetrahedral network positions. Six-coordinated silicon is present in lead phosphosilicate glasses containing large proportions of P_2O_5 Six-coordinated silicon atoms are surrounded only by $[POO_{3/2}]$ groups[5].

^{31}P NMR spectra of several inorganic phosphates have been examined both in the crystalline and glassy states. The ^{31}P resonances of ortho, pyro and meta phosphates appear in distinct regions when plotted as a function of $(Z_{eff}/r),q$ (where Z_{eff} is the effective nuclear charge and r, the radius of the cation and q, the partial charge on P) Based on the diagram, inorganic phosphate glasses are shown to consist essentially of metaphosphate units[6] NMR resonances of the glasses are generally broader than those of crystalline phosphates.

In the aluminophosphate gels, Al is octahedrally coordinated in the xerogel and partially converted into tetrahedrally coordinated Al on heating. Phosphorous is present as metaphosphate[7]. The structure of $AlPO_4$ is shown to consist of $[AlO_{4/2}]^-$ and $[PO_{4/2}]^+$.

The sensitivity of this technique to even the minor changes in the local structure was demonstrated by examining glassy and crystalline $Na_4Nb(PO_4)_3$ by means of ^{31}P NMR[8].

To explain the processes occurring during the crystallization of gels as well as the local structural preferences of Al, Si and P, use has been made of the acid–base concepts and the electronegativity equalization principle. More importantly, it has been possible to rationalize all the known silicon chemical shifts in gels, glasses and crystals of silicate systems by making use of graph-theoretical approach to describe the structural units along with group electronegativities and ionic potential of the modifier cation. A universal function for ^{29}Si chemical shifts in silicates has been presented[9]. The relation (ppm) = 28.4 (1−exp (−P)) − 110.5, besides having predictive value, satisfactorily accounts for all the available chemical shift data on silicates and shows the right kind of limiting behaviour, with approaching Q_0 value at large P

^{11}B MAS NMR spectroscopic investigations of boric oxide and alkali borate glasses have been carried out. The chemical shift of trigonal boron shows an anomalous behaviour around 10 mol% alkali in all the $M_2O.B_2O_3$ (M = Li, Na and K) glasses studied. The variation in the chemical shift of the trigonal boron with composition was explained by re-examining the structure of B_2O_3 glass A new structural model for B_2O_3 glass has been proposed according to which two thirds of the boron atoms are present in the boroxol units, while the rest are in loose $BO_{3/2}$ units[10]. The model emphasizes the need for the use of topochemical concepts in understanding the formation of tetraborate and diborate units in the glasses. Furthermore, the model is shown to be consistent with key observations reported in literature.

The phase transitions associated with the formation of α-Al_2O_3 and β-Al_2O_3 from γ-Al_2O_3 have been studied by the combined use of ^{27}Al NMR and X-ray diffraction. Analysis of the kinetic data using the Avrami–Eurofeev equation points to the important role of nucleation in both these transitions[11].

References

1. RAO, C N.R AND GOPALAKRISHNAN, J. — *New directions in solid state chemistry*, 1986, Cambridge Solid State Science Series, Cambridge University Press
2. PRABAKAR, S., RAO, K.J AND RAO, C.N.R. — *J. Mater Res*, 1991, **6**, 592–601
3. PRABAKAR, S., RAO, K.J. AND RAO, C N.R — *Eur J Solid St. Inorg Chem.*, 1991, **29**, 95–110.
4. PRABAKAR, S. AND RAO, K J — *Phil. Mag B*, 1991, **64**, 401–411.
5. PRABAKAR, S , RAO, K J. AND RAO, C.N R — *Mater. Res. Bull*, 1991, **26**, 285–294.
6. PRABAKAR, S , RAO, K J AND RAO, C N.R — *Chem. Phys. Lett.*, 1987, **139**, 96–102.
7. PRABAKAR, S., RAO, K J AND RAO, C.N.R — *Mater. Res Bull.*, 1991, **26**, 805–812

8. PRABAKAR, S AND RAO, K J — *J. Solid St Chem.*, 1991, **91**, 186–188

9 PRABAKAR, S , RAO, K.J AND RAO, C N.R — *Chem. Phys Lett*, 1991, **183**, 176–182

10. PRABAKAR, S , RAO, K J AND RAO, C.N.R. — *Proc. R. Soc Lond. A*, 1990, **429**, 1–15

11. PRABAKAR, S., RAO, K J. AND RAO, C N.R. — *J Mater. Res.*, 1991, **6**, 2701–2705

Thesis Abstract (Ph.D.)

Theoretical studies of novel electronic effects in radicals and radical ions by K. Pius
Research supervisor: J. Chandrasekhar
Department: Organic Chemistry

1. Introduction

This work involves a systematic investigation of radicals and radical ions using quantum mechanical methods. Not much is known about radical ions as compared to the much more comprehensive store of data available on other reactive intermediates. The present study attempts to unravel certain unusual structural preferences in radical ions as also some novel electronic effects which operate in radicals and radical ions.

Various experimental methods are widely used for the generation and detection of radicals and radical ions. The computational approach represents an attractive alternative to obtain detailed information about the structure and energetics of these species. The computational methodologies employed in the present investigation are *ab initio* and semi-empirical molecular orbital theories.

2. Results and discussion

The structure and energetics of a novel class of radical ions called distonic ions have been examined in detail. Distonic ions are hydrogen-shifted isomers of classical radical ions, with their formal charge and radical centres located on two different atoms. The preference for radical ions to adopt these types of structures merits considerable attention if one recalls that the corresponding neutral molecules are not even minima on the potential energy surface in most cases. The stabilities of distonic ions relative to classical isomeric forms have been modelled by means of idealized reactions involving separation of charge and radical of smaller fragments. *Ab initio* energies at high levels of theory for these reactions indicate the existence of several distonic ions more stabilized than previously known organic distonic ions[1]. This approach has led to the hypothesis that the tendency to adopt distonic structures should increase with the difference in electronegativities of the charge and radical-bearing atoms of the distonic isomer For example, silanol radical cation has been shown to favour the distonic structure ($\bullet SiH_2OH_2^+$) over the classical structure ($SiH_3OH^{+\bullet}$) to a greater extent than methanol radical cation. Calculations carried out at *ab initio* and semi-empirical levels have revealed that the preference for distonic structure is, in general, more among silicon-based radical cations than their carbon-based analogues[2]

Radical anions too have been shown to prefer distonic-type structures[3]. The tendency to assume distonic structures on addition or removal of an electron has been proved to be quite general. Various phosphorus and boron-based radical ions have been shown to favour hydrogen-rearranged structures. Experimentally accessible systems which are likely to adopt distonic structures have been studied. The investigations that have been carried out on radical ions have led to the interesting suggestion that some molecules would undergo hydrogen migration both on removal and addition of an electron.

The magnitude of the captodative effect in radical ions has been estimated using semi-empirical and

ab initio molecular orbital methods[3]. Calculations indicate that the effect is much more pronounced in radical cations and radical anions than in neutral radicals. The enhanced captodative stabilization in radical ions can be rationalized on the basis of qualitative molecular orbital theory. The results have implications for preferred mass spectral fragmentation pathways.

The competition between two important non-additivity effects operating in some disubstituted radicals, namely, the anomeric effect and the one due to extended delocalization has been examined and its structural and energetic consequences discussed. Different conformations of such radicals which enjoy stabilization due to varying extents of these non-additivity effects have been examined. Many symmetrically disubstituted radicals, including dihydroxy and diaminomethyl radicals, have been shown to adopt non-planar asymmetric structures which are seldom proposed for them The results have wide implications in determining the course of stereo-specific radical reactions in carbohydrate substrates. The study exposes the fallacy of using these disubstituted radicals as reference species for estimating other non-additivity effects.

An MNDO study of organometallic complexes of the type $Li(R)_n$ with R=C_2H_2, C_2H_4 or C_6H_6 for n=1 or 2 has been carried out Several structures proposed for these complexes have been examined and characterized by carrying out frequency calculations The calculated results have been interpreted by viewing the species as complexes between Li^+ and ligand radical anions. The preferred structures have been rationalized on the basis of Huckel and Mobius topologies of the ligand Pi^* orbitals

References

1. PIUS, K AND CHANDRASEKHAR, J — *Curr Sci*, 1987, **56**, 857–860
2. PIUS, K AND CHANDRASEKHAR, J. — *Int J Mass Spctrometry Ion Processes*, 1989, **87**, R15–R18.
3. PIUS, K AND CHANDRASEKHAR, J. — *J Chem Soc, Perkin Trans II*, 1988, 1291–1295
4. PIUS, K. AND CHANDRASEKHAR, J — *J. Chem Soc., Chem Commun.*, 1990, 41–42

Thesis Abstract (Ph.D.)

Investigations of catalysts and oxide superconductors by EXAFS and other techniques

by G. U. Kulkarni
Research supervisor: C. N. R. Rao
Department: Solid State and Structural Chemistry Unit

1. Introduction

There is increasing interest in the surface science community today to understand the structural, electronic and chemical properties of dispersed metal systems which are of importance in many technological processes, especially catalysis. Extended X-ray absorption fine structure (EXAFS) is ideally suited for the study of supported metal catalysts which cannot be usefully examined by conventional structural techniques[1]. In this work, results of EXAFS and Mossbauer spectroscopic investigations of a few important catalyst systems are reported. The catalysts studied are: monometallic iron, nickel and copper catalysts supported on SiC_2 and γ-Al_2O_3, bimetallic Fe-Ni/SiO_2, Fe-Cu/SiO_2, Cu-Ni/SiO_2 and Cu-Ni/γ-Al_2O_3 catalysts, T-Mo/γ-Al_2O_3 (T = Fe,Co,Ni and Cu) and Mo/TiO_2 hydrodesulphurization (HDS) catalysts. The present investigations have yielded some results of relevance to catalysis. In view of the importance of understanding the electronic structure of high T_c superconductors[2], we have carried out detailed investigations on the nature of the metal ions in these systems employing X-ray absorption near edge structure (XANES).

2. Experimental

Monometallic catalyst samples (metal loadings up to 20 wt%), bimetallic catalysts (different proportions

of the component metals with a total metal loading of 20 wt%)[3] and HDS catalysts[4] were prepared by the procedure described in literature. X-ray absorption spectra were recorded at room temperature using a Rigaku spectrometer (Johanson geometry) attached to a 12 kW rotating anode x-ray generator (Ru −200B, Rigaku, Japan). ^{57}Fe Mossbauer spectra were recorded with a home-built constant acceleration spectrometer using a 25 mCi ^{57}Co source in Pd matrix (Amersham Corporation, UK). All the measurements were carried out in *in-situ* conditions employing an indigenously designed quartz cell

3. Analysis of data

The EXAFS data were analysed in the single scattering approximation where the EXAFS function is related to the structural parameters by

$$\chi(k) = \Sigma_j (N_j/R_j^2 k) \exp(-2r_j^2 k^2)\ F_j(k)\ \sin[2R_j k + \Theta_j(k)] \tag{1}$$

where

$$k = (1/\hbar)\ [2m(E-E_o)]^{1/2} \tag{2}$$

and N_j, R_j and r_j are the number of nearest neighbours of the jth shell, the interatomic distance and the Debye–Waller term, respectively. $F_j(k)$ and $\phi_j(k)$ are the amplitude and phase functions, respectively. Normalized EXAFS data were extracted from the raw absorption spectra after background subtraction using a cubic spline fit. The normalized data were Fourier transformed to r-space and the region of interest (1–4 Å) was windowed and backtransformed for further curve-fitting analysis.

In the case of a multiphasic system the EXAFS function $\chi(k)$ is defined as

$$\chi_{\text{Total}}(k) = \Sigma_i x_i C_{i,m} \chi_{i,m}(k) \tag{3}$$

where x_i is the fraction of the ith phase and $C_{i,m}$, the fraction of the jth coordination in the ith phase. Comparing eqns 1 and 3, we find that N_j and x_j are complementary; consequently, we have employed fixed N_j values (as obtained from model compounds). The unknown scatterers were determined using residual spectrum method, obtained as the difference between the calculated and experimental EXAFS data. In addition to the above-mentioned analysis, we have employed the logarithmic ratio of the amplitude part of the EXAFS function of the model system and the experimental system for determining the types of back scatterers.

4. Results and discussion

Our work on mono- and bimetallic catalysts has shown that the reducibility of the transition metal ions to the metallic state on treatment with hydrogen is only partial in monometallic catalysts such as Fe/SiO_2 or Ni/SiO_2; in the bimetallic catalysts such as Fe–Ni/SiO_2, however, the reducibility of Fe as well as Ni is far greater than that in the corresponding monometallic catalysts. The reducibilty and catalytic activity of the Fe–Ni/SiO_2, Fe–Cu/SiO_2 and Cu–Ni/SiO_2 or Al_2O_3 catalysts have been related to the tendency to form alloys on the basis of a detailed study of their structure and magnetic properties, involving both *in-situ* EXAFS and Mossbauer measurements. The reduced bimetallic catalysts show evidence for the formation of FCC or BCC alloy phases which are superparamagnetic or ferromagnetic depending on the composition and also the pretreatment conditions. The most active catalyst (Fe:Ni = 25:75) is found to contain superparamagnetic FeNi particles mostly in FCC structure.

Alumina-supported molybdenum sulphide catalysts show a few orders of enhancement in HDS activity when promoters such as nickel and cobalt are added. The promotion effect of iron is marginal whereas copper acts as a poison. We have investigated the local structure around the promoter transition metal atom as well as Mo in T–MoS_2/γ-Al_2O_3 (T = Fe, Co, Ni and Cu) catalysts by employing *in-situ* EXAFS. Short T–S distances are observed in the active [Ni(Co)–Mo–S] phases (0.2 Å less as compared to that in bulk sulphides) while Fe and Cu have been found to have Fe(Cu)–S distances just as in the bulk sulphides. Effects of pretreatment and compostion on the formation of the active phase are dealt with in detail. In

addition, we have investigated the Mo/TiO_2 catalyst which has been reported recently to be HDS-active. Short Mo–S distance have been found in the sulphided Mo/TiO_2 catalysts due to thiomolybdate species, this species is absent in $Mo/\gamma-Al_2O_3$ catalysts.

We have studied the charge states of the different metal ions in several cuprates by employing XANES spectroscopy. The study includes Cu, K, Tl–L_3, Pb–L_3 and Bi–L_3 XANES of the various cuprates. The Cu K–XANES of $YBa_2Cu_3O_{7-x}$ compound has shown that the proportion of Cu^{1+} species increases with x. The Tl–L_3 and Bi–L_3 XANES measurements on various thallium and bismuth cuprates have shown that Tl^{3+} and Bi^{3+} are the preponderant species in these compounds. Lead is shown to be in the 2+ state in lead cuprates while in the 4+ state it exists as a substitute for Tl^{3+} in thallium cuprates. In addition, the oxidation states of Bi and Pb in $Ba(Bi,Pb)O_3$ have been examined by a combined use of XANES and core-level X-ray photoelectron spectra.

References

1. WONG, J. *Mater. Sci. Engng.*, 1986, **80**, 107–144
2. RAO, C. N. R. AND RAVEAU, B. *Acc. Chem. Res.*, 1989, **22**, 106–132
3. WEILERS, A. F. H., KOCK, A. J. H. M., HOP, C. E. C. A., GENS, J. W. AND VANDER KRAAN, A. M. *J. Catal.*, 1989, **117**, 1–8.
4. ROB VAN VEEN, J. A., GERKEEMA, E., VANDER KRAAN, A. M. AND KNOESTER, A. *J. Chem. Soc., Chem. Commun.*, 1987, 1684–1686

Thesis Abstract (Ph.D.)

Combustion synthesis and properties of fine particle spinel, perovskite and K_2NiF_4 type oxides by S. Sundar Manoharan

Research supervisor: K.C. Patil

Department: Inorganic and Physical Chemistry

1. Introduction

Oxides form a major class of compounds in the field of ceramics. Depending upon the crystal structure, oxides are classified as spinels, perovskites and K_2NiF_4 type. Some technologically important oxide materials and their uses are: refractories ($MgCr_2O_4$, $LaCrO_3$), catalysts ($CuCr_2O_4$, $LaCoO_3$, La_2NiO_4), sensors ($ZnCr_2O_4$), pigments($CoCr_2O_4$), electrode materials ($LaMnO_3$), heating elements for high-temperature furnaces ($LaCrO_3$) and high T_c superconductors ($La_{1.8}Sr_{0.2}CuO_4$).

Preparation of these oxide materials by the conventional ceramic method incurs costly penalties on energy and time since they require high-temperature furnaces and longer processing time. Alternatively, several wet chemical methods[1] have emerged which include precursor method (involving oxalates, carbonates, citrates, nitrates and hydrazine carboxylates), freeze-drying, spray-drying techniques, etc. The emphasis in all these techniques is to obtain oxides in a reactive form.

Self-propagating high-temperature synthesis (SHS)[2] involving metal powders and non-metals has been employed for the preparation of exotic, high-temperature ceramics such as metal carbides, borides, silicides which find application as refractories, abrasives, heating elements and in powder metallurgy. It is interesting to note that the exothermicity of these solid-state reactions arises from the redox reactions between metals and non-metals which act as fuels and oxidizers, respectively. Extending this idea it has now been possible to prepare oxides of different structural types using redox mixtures containing metal nitrates (oxidizers) and hydrazine derivatives such as carbohydrazide, tetraformal triazine, 4-amino-3,5-dimethyl-1,2,4-triazole and urea (fuels). The oxides prepared by this process include MCr_2O_4, $LnMO_3$, La_2MO_4 and $La_{1.8}Sr_{0.2}CuO_4$.

2. Experimental

The instrumental techniques used in the present investigation are: powder X-ray diffraction, IR, UV-visible and X-ray photoelectron spectroscopy, density, particle size, surface area, transmission electron microscopy (TEM) and scanning electron microscopy (SEM). The catalytic property of some oxide materials for N_2O decomposition was studied using an all-glass static reactor.

3. Results and discussion

3.1. Combustion synthesis and properties of fine-particle spinel chromites, MCr_2O_4 (where M=Mg, Ca, Mn, Fe, Co, Ni, Cu, and Zn)[3]

The stoichiometric composition of the redox mixtures was calculated based on the total oxidizing and reducing valencies of the oxidizer and fuel which serves as numerical coefficients for stoichiometric balance so that the equivalence ratio ϕ is unity, *i.e.*, $o/f = 1.0$ and the energy released is at maximum. According to the concepts employed in propellant chemistry the elements C, H, Sr, Cu, La or any other metal are considered as reducing elements with corresponding valencies +4, +1, +2, +2 +3, respectively. The element oxygen is considered as oxidizing element with the valency −2. The valency of nitrogen is considered to be zero. Accordingly, the oxidizing and reducing valencies of the compounds used in the combustion mixtures can be calculated

Metal chromites, MCr_2O_4, were prepared by the combustion of corresponding metal nitrate–tetraformal triazine and metal nitrate–urea mixtures at 350°C in a few minutes. The resulting oxides were fine, fluffy and voluminous in nature. Formation of single-phase products was confirmed by XRD. The surface area of chromite powders obtained by TFTA process is higher (15–30 m^2/g) compared to the chromites prepared by urea process (5–25 m^2/g). The observed variation in the particulate properties is attributed to the combustible nature of the decomposition products of TFTA and urea and also to the amount of gases evolved during combustion. Sintering studies of $CaCr_2O_4$ and $MgCr_2O_4$ reveal the effect of powder processing method and narrow particle size distribution on the final microstructure. Uniform grains with an average size of 5μm and 10% porosity have been achieved for $MgCr_2O_4$ sintered at lower temperatures (< 1500°C) in air.

3.2. Combustion synthesis and properties of fine-particle perovskite oxides, $LnCrO_3$ (where Ln=La, Pr, Sm, Nd, Gd, Dy and Y), $La(Sr)MnO_3$, $LaCoO_3$ and $LaNiO_3$[4]

Rare-earth chromites, $LnCrO_3$, where Ln=La, Pr, Nd, Sm, Dy, Tb, Gd and Y were prepared by the combustion of metal nitrate–carbohydrazide and metal nitrate–TFTA mixtures at 350°C $LnCrO_3$ prepared by carbohydrazide process has more surface area (20–65 m^2/g) compared to TFTA process (8–19 m^2/g). The nature of fuel appears to alter the particulate property. Sintering of $LaCrO_3$ at 1500°C resulted in fine-grained microstructure, thus demonstrating that uniform particle size provides a measure of stability against exaggerated grain growth. $La_{1-x}Sr_xMnO_3$ (where x = 0.0, 0.2, 0.3, 0.4 and 0.5) was prepared by the combustion of corresponding metal nitrate–TFTA mixture at 500°C in a few minutes. Chemical analyses of the combustion product reveals that uniform doping of Sr ions in the A-site could be achieved by the combustion process. Combustion of metal nitrate–TFTA and metal nitrate–carbohydrazide redox mixtures resulted in amorphous powder which on annealing at 600–800°C for 1 h resulted in crystalline single-phase product.

3.3. Combustion synthesis and properties of K_2NiF_4-type oxides, La_2MO_4 (where M=Co, Ni, and Cu) and $La_{1.8}Sr_{0.2}CuO_4$[5]

Fine-particle K_2NiF_4-type oxides have been prepared by the combustion of metal nitrate–tetraformal trisazine/triazole mixtures at 350/550°C. Fine-particle nature of these oxides has been studied using density, particle size, surface area, SEM and TEM measurements. The strontium-doped La_2CuO_4, $La_{1.8}Sr_{0.2}CuO_4$ shows superconductivity at 34K as reported. The temperature dependence of the resistance in different magnetic fields (0 to 5 tesla) has been measured. The high-temperature side of the transition is little influenced by the magnetic field, on the other hand, the low-temperature side depends strongly on the magnetic field and the transition is extended towards the lower temperature.

3.4. Catalytic properties of combustion-derived oxides for the decomposition of N_2O

Kinetic studies were carried out for the N_2O decomposition on $CuCr_2O_4$, $LaCrO_3$, $LaMnO_3$ and La_2NiO_4. The kinetic data were analysed using standard rate expressions corresponding to no inhibition and strong inhibition by the product oxygen. The reactivity of these fine particles, large surface area powders show an order of magnitude higher for N_2O decomposition compared to the oxides prepared by the ceramic method/oxalate precursors The increasing reactivity of these oxides follows the order $La_2NiO_4 > LaMnO_3 > CuCr_2O_4 > LaCrO_3$.

References

1 ROETTENBACHER, R. AND SCHMIDBERGER, R. Ceramic Powders. In *Materials science monographs* (P. Vincenzin, ed.), Vol 16, 1983, p. 539, Elsevier

2. HLAVACEK, V. *Am. Ceram. Soc. Bull.*, 1991, **70**, 240–242

3 SUNDAR MANOHARAN, S. KUMAR, N R.S. AND PATIL, K C *Mater. Res. Bull.*, 1990, **25**, 731–739.

4 SUNDAR MANOHARAN, S. AND PATIL, K.C *Advances in ferrites* (C M. Srivatsava and M. J. Patni, eds) Vol. 1, pp. 1179–1183, 1990, Oxford & IBH Publishing.

5 SUNDAR MANOHARAN, S., PRASAD, V., SUBRAMANYAM, S V AND PATIL, K C *Physica C*, 1991, **190**, 225–228

Thesis Abstract (Ph.D.)

Inter and intramolecular electron transfer in porphyrin-acceptor systems by Francis D'Souza

Research supervisor: V. Krishnan

Department: Inorganic and Physical Chemistry

1. Introduction

Studies on photoinduced electron transfer (PET) reactions are of particular interest owing to their importance in understanding the basic biological phenomena such as photosynthesis, vision and others. The rates of electron transfer (ET) reaction vary between several minutes and several femto seconds and this depends on many complex variables that dictate the nature of interaction between the electron donor and the electron acceptor[1]. The work presents a few novel studies on donor–acceptor systems involving porphyrin as donor and several acceptors, *viz.*, iron(III) coordination compounds, organic disulfides and phenolphthalein (both in lactone and quinone forms). The intramolecular study involves covalently linked donor–acceptor systems involving porphyrin as donor and several acceptors, *viz.*, iron(III) coordination compounds, organic disulfides and phenolphthalein (both in lactone and quinone forms). The intramolecular study involves covalently linked donor–acceptor systems wherein the acceptor is appended to the porphyrin at different orientations and several distal separations. In addition to this, PET within a porphyrin superstructure where the thioetherbound silver(I) ions form the acceptor entity has been investigated.

2. Main results and conclusions

Intermolecular complexation of free-base porphyrin and its zinc(II) and magnesium(II) derivatives with various iron (III) coordination compounds have been studied in acetonitrile and micellar media such as SDS, Triton X-100 and CTAB. The iron(III) coordination compounds possess different geometries and spin states, *viz*, octahedral ($^6A_1$, $^2T_{2g}$), tetrahedral (^2E), square pyramidal and square planar (^2B). The quenching of the singlet emission of the porphyrins has been shown to proceed predominantly through electron transfer mechanism. The bimolecular quenching coefficient was found to be in the range of 10^9–10^{10} $M^{-1}s^{-1}$. Evidence for electron transfer in these systems has been obtained from steady-state photolysis

experiments The excited state reduction potential of the porphyrin $^1P^*/P^-$ (where P = porphyrins) obtained from Stern–Volmer quenching values agrees well with the theoretically estimated values. The rate data reveals the absence of Marcus-inverted region[2]

Studies on intramolecularly bound porphyrin–phenolphthalein systems have yielded many important results The variation of the distance and orientation of the acceptor unit with respect to porphyrin and a change in pH (lactone to semiquinone form of the acceptor) has resulted in significant changes of the electronic absorption and emission, and magnetic resonance spectra[3]. The rate of intramolecular PET determined from the time-resolved fluorescence is found to decrease with an increase in the length of the covalent linkage and also vary with the nature of substitution as *ortho* > *para*.

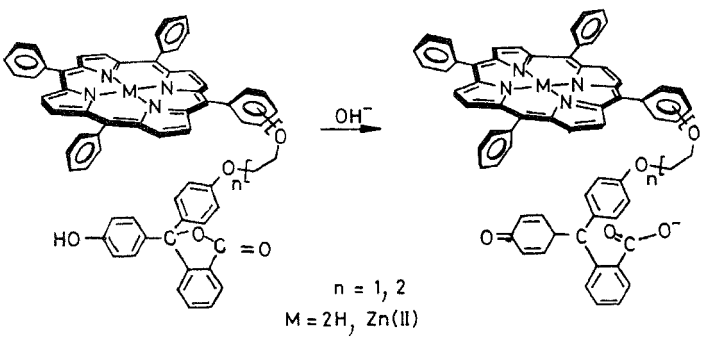

Interesting results have been obtained in inter and intramolecular complexation studies of porphyrin and 5,5-dithiobis-2-nitrobenzoic acid, DTNB. It is shown that free-base porphyrin and its zinc(II) derivative interact with DTNB with an association constant (K_{ass}) of 30 and 36 $M^{-1}dm^3$, respectively. The bimolecular rate coefficients obtained from the time-resolved emission studies were found to be in the order of $10^9M^{-1}s^{-1}$. The energetics of the CT state $P^{+\cdot}$–$DTNB^{-\cdot}$ obtained from the electrochemical redox studies and the estimated free-energy change (ΔG_{ET}) for these systems (ca −50 meV for free-base porphyrin derivatives and ~ −270 meV for its zinc(II) derivatives) reveal that the PET reactions are possible both in the free-base and its zinc(II) derivatives Steady-state and time-resolved fluorescence studies exhibited electron transfer to be the dominant pathway for fluorescence quenching in these systems[4]. The rate of ET reaction obtained from the life time measurements (10^8–10^9 s^{-1}) for these covalently linked porphyrin–DTNB systems varies as zinc(II) porphyrin > free-base porphyrin. Evidence for PET has been found from steady-state photolysis experiments which revealed the formation of thiolate anion in the presence of a sacrificial donor Computer simulation of the structures has suggested a critical electron transfer distance of ca 6.7 Å from the centre of the porphyrin to the disulfide group of DTNB, with a face-to-face orientation of the two interacting chromophores. The products of electrochemical reduction of covalently linked porphyrin–DTNB systems are found to be different from those observed for the photochemical studies.

'All *cis*' tetrakis (*o*-tetrahydrothiophenamidophenyl) porphinato zinc(II), $ZnPS_4$ cooperatively binds two Ag^+ ions with a dissociation constant of 2.2×10^{-11} M^{-1} dm^3. Time-resolved fluorescence studies have shown that PET occurs within the superstructure from the singlet excited state of the zinc(II) porphyrin to the bound Ag^+ ion with a rate constant of ~ 10^8 s^{-1}.

It has been observed that in the case of zinc(II) and cobalt(II)-metallated bis porphyrin derivatives the chemical or electrochemical reduction of the disulfide group results in well-defined hyperporphyrin spectra

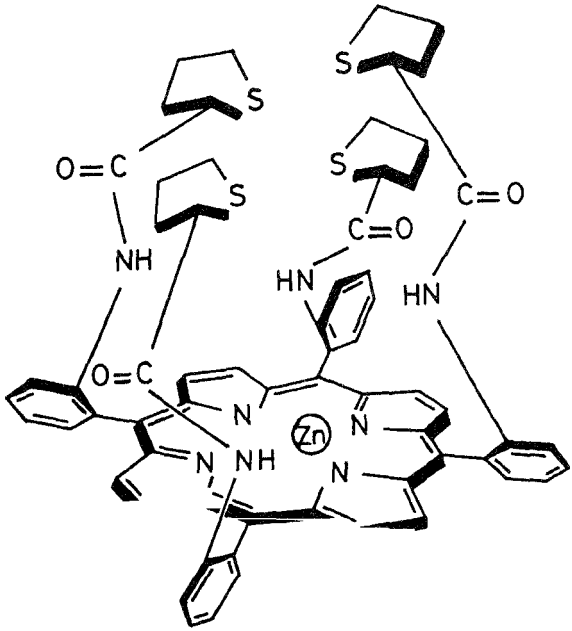

representative of five coordinate complexes with thiolate as axial ligand. The relative binding of thiolate to the metal centre is found to be orientation dependent with respect to the substitution at the phenyl ring of the porphyrin[5]. Solution-averaged structures for the ortho-, meta- and para-linked dimers have been proposed based on the optical and magnetic resonance studies.

References

1. GUST, D. AND MOORE, T A.(eds) — Covalently linked donor–acceptor species for mimicry of photosynthetic electron and energy transfer, *Tetrahedron*, 1989, **45**, 4669–4983.
2. D'SOUZA, F. AND KRISHNAN, V — Singlet quenching of tetraphenylporphyrin and its metal derivatives by iron(III) coordination compounds, *Proc. Indian Acad Sci (Chem Sci)*, 1990, **102**, 131–146.
3. D'SOUZA, F. AND KRISHNAN, V. — Intramolecular donor–acceptor systems: Structures of novel linked porphyrin–phenolphthalein molecular systems, *Photochem. Photobiol.*, 1990, **51**, 285–291.
4. D'SOUZA, F. AND KRISHNAN, V. — Inter- and intramolecular interactions of porphyrins with 5,5-dithiobis (2-nitrobenzoic acid), *Photochem Photobiol.*, 1992, **56**, 145–156.
5. D'SOUZA, F. AND KRISHNAN, V — Coordination behaviour of metalloporphyrin with intramolecularly linked thiolate ligand, *Inorg. Chim. Acta*, 1990, **176**, 131–137.

Thesis Abstract (Ph.D.)

Theoretical studies of the flow of physiological fluids under pathological situations by R. V. Sagayamary
Research supervisor: G. Nath
Department: Mathematics

1. Introduction

It is well known that blood vessels bifurcate at frequent intervals and the diameter of the vessels varies with distance[1]. Hence the concept of flow in a slowly varying cross-section forms the basis of a large class of problems in understanding blood flows. To consider relevant geometrical and physiological details, this idea of slowly varying cross-section has been utilized in producing desirable axisymmetric constrictions or taper in a tube. Also, developments in microcontinuum fluid mechanics are well documented in the review article by Ariman *et al*[2] and the relations between many different theories are demonstrated with the aid of various tables.

Apart from stenosis, thrombosis is yet another concept of pathology involving greater observation in recent years. It is the deposition of masses formed by blood constituents which results in a clot. The only investigation which is relevant to the present work is that of Doffin and Chagnean[3]. However, the concept of clot formation in the arterial stenosis leading to thrombosis using mathematical modelling has not been studied so far.

Keeping all these aspects in mind, some theoretical investigations are carried out to study the various aspects of blood flow in the cardiovascular system based on the principles of fluid dynamics.

2. Present study

The investigations presented consider both Newtonian as well as non-Newtonian models of blood, while its motion is taken to be laminar. The basic equations are considered such that they include the nonlinear inertial effects too. The flow through tubes of arbitrary cross-sections is considered throughout the work so that a large class of problems can be analysed by specifying the particular type of cross-section. Solutions are obtained using long wavelength approximation.

The first problem deals with the flow of an incompressible couple stress fluid in a tube with slowly varying cross-section, where the effects of vessel tapering and arbitrary shape of the stenosis on the flow characteristics have been explored[4] Expressions for axial velocity and shear stress distribution on the walls are derived and a few special situations are examined to study the influence of the couple stress property of the fluid on the flow characteristics.

In the second problem, a simple mathematical analysis of the steady flow of Newtonian fluid in stenosed arteries with the existence of a clot in the middle is carried out to study the additional effects of the clot along with those of the stenosis. A brief study is also done on the blood flow through arterial stenosis with an inserted catheter. The above analysis is extended to include the visco-elastic properties of blood. Catheter insertion on the peristatic motion of visco-elastic fluid through tubes of arbitrary wave shape is studied. Axial velocities, wall shear stress and streamlines are drawn and a comparative work has been carried out to find the effects of the insertion of the catheter, size of the catheter and the visco-elastic parameter.

3. Conclusions

As a stenosis develops in an artery, the nature of the flow in its vicinity is significantly altered. The degree of the alteration is strongly influenced by the severity of the stenosis. A comparison of the axial velocity and wall shear stress profiles of Newtonian and non-Newtonian fluids is made. It is observed that the shear stress vanishes indicating the existence of separation zones. It is evident that the existence of negative velocities is the characteristic feature of non-Newtonian fluid while the Newtonian profile is positive at every cross-section.

Separation zones near the stenosis are not observed whereas such zones near the clot are predominant. Also, it is observed that higher the protuberance, the smaller is the required Re for back flow to be initiated. Besides, the shape of the stenosis alters the flow to be initiated. Besides, the shape of stenosis alters the flow apart from the present stenosis. The streamline pattern exhibits the existence of recirculating zones resulting in vortices. It is also found that the insertion of the catheter influences the flow characteristics and the size of the catheter has a large role in it. Considering the blood as visco-elastic fluid, the maximum difference between the results of Newtonian and visco-elastic fluids is 11.9%. The changes in shear stress which are seen to be a sensitive factor clearly explain that the non-Newtonian character is very much relevant in evaluating the damages caused by the higher shear stress on the arterial walls.

A comparative study with the earlier works regarding peristaltic motion of fluids taking the wave shape by

$$s(x) = \begin{cases} B + Ax^n & \text{for } 0 < x < 1 \\ B + Al^n & \text{for } 1 < x < l \end{cases}$$

exhibits clearly the influence of catheter and of non-Newtonian fluid The streamline pattern results in concentric loops near the wall which can be associated with the retrograde motion of a part of the total urine flow in a direction opposite to the main urine flow.

References

1 WHITMORE, R L. *Rheology of circulation*, 1968, Pergamon Press.

2. ARIMAN, T., TURK, M A. AND SYLVASTER, N.D Microcontinuum fluid mechanics—A review, *Int. J. Engng Sci.*, 1973, **11**, 905–930.

3 DOFFIN, J. AND CHANGNEAU, F. Oscillating flow between a clot model and a stenosis, *J. Biomech.*, 1981, **14**, 143–148

4 SAGAYAMARY, R V. AND DEVANATHAN, R Steady flow of couple stress fluid through tubes of slowly varying cross-sections–Application to blood flows, *Biorheology*, 1989, **26**, 753–769.

Thesis Abstract (Ph.D.)

Analysis of mathematical models of blood flow in the cardiovascular system by K. V. Manjula
Research supervisor: G. Nath
Department: Mathematics

1. Introduction

Rheological interest in the cardiovascular system centres on the extent to which the flow characteristics of blood and the physical properties of the walls of the blood vessels influence flow resistance and pressure wave propagation of the system under both normal and pathological conditions[1]. As a consequence, much attention is being paid to the study of detailed or local flow patterns in the circulatory system by using both theoretical and experimental means based on the principles of fluid mechanics. The basic idea in the theoretical models is to assign known characteristics to the motion of the fluid (blood) and the vessel walls and describe these by the equations of motion, like the Navier-Stokes equations of momentum transfer and equation of continuity for the fluid flow and the membrane equations to describe the tube wall motion. Based on the existing literature, it is evident that there are certain important problems which have either been studied approximately, like using only linear models or certain effects, like that due to the structure of vessel wall, have not been taken into consideration. We address some of these problems.

2. Present study

The present analysis involves mainly the entrance effects and the cardiac catheterisation on the blood flow based on the nonlinear mathematical modelling of cardiovascular system. Throughout the study, blood is treated as a homogeneous, viscous, incompressible Newtonian fluid and the flow is considered to be laminar. The walls of the blood vessels are assumed to be rigid. This is because the study is mainly confined to those parts of the systemic circulation where the diameter of the blood vessels is large enough to satisfy the above conditions. The governing set of equations are Navier–Stokes equations for the axisymmetric flow of an incompressible Newtonian fluid

Based on the observation that *in vivo* measurements of flow characteristics sometimes give rise to serious instrumentation and physiological problems[3], the problem of estimating errors involved in pressure readings using a catheter-type pressure transducer is studied. Due to frequent occurrence of arterial lesions leading to stenosis, analysis of the blood flow through a stenosed artery in the presence of a catheter is carried out using both linear and nonlinear mathematical models, where the nonlinear problem is studied numerically using a finite-differencer scheme. The problem is studied both for steady and oscillatory flow conditions in the developed region of blood vessels.

The cardiovascular system is characterised by a large number of tube branchings and many times, an artery bifurcates before the flow in it is fully developed. Hence, in the present work emphasis is also laid on entry flows taking into consideration the effects of such hemodynamic properties as unsteady flow of blood and the permeability of vessel walls. We have investigated the blood flow development effects in large arteries in the beginning of the cardiac cycle using a nonlinear mathematical model of a flow impulsively started from rest in a semi-infinite tube which later develops into a steady flow. A closed-form solution to the integral momentum equation is obtained by the method of characteristics to determine the flow variables. We have also taken into consideration the porosity of the vessel walls separately[3] while studying the entry flow problem because in microcirculation the mechanism of water and other metabolic end products between blood and various tissues takes place through the walls of the vessels. Using the boundary-layer approach, an analytical method is developed to obtain an exact solution for the nonlinear equations which predicts the steady flow development and pressure drop in the inlet of a pipe.

3. Results and discussion

Closed-form solutions obtained using a linearised form of the Navier–Stokes equations for a steady flow of blood through a stenosed arterial section in the presence of a catheter indicate that the error, which is the magnitude of the difference in the values of the flow variables with and without a catheter, increases with the increase in the radius of the catheter and also with the height of the stenosis. Pressure readings are found to be more sensitive to changes in the catheter radius when compared to the stenosis height as observed by Bjorno and Petterson[4]. In the case of an oscillatory flow where once again closed-form solutions are obtained using a linearised Navier–Stokes equations, the maximum value of the errors over a period of one cycle is found to be always greater than the corresponding value in the steady flow. A mathematical model, where nonlinear terms in the Navier–Stokes equations are retained for the unsteady flow problem, is analysed using a finite-difference scheme. Applicability of this method has been checked by considering an oscillatory flow in a straight tube and comparing the obtained results with the exact analytical solution. It is found that the results are in good agreement with the analytical solution (error less than 1%). A comparison of the present results with the numerical results of Lloyd *et al*[5] for the case of unsteady flow in a stenosed artery without a catheter indicate that the difference between the results is within 5%. It is found that when both the inertial and the viscous forces are taken into consideration, errors due to catheterisation are about one-third of the errors obtained by neglecting the inertial forces in a stenosed tube. Magnitude of the errors is also less when compared to the existing theoretical results and hence agrees better with the experimental results of Kanai *et al*[6].

The study of impulsively started laminar flow in the entrance region of a circular tube with constant inlet velocity by using integral momentum approach shows that the steady-state entrance length obtained is the same as that of Campbell and Slattery[7]. This means for the physiological ranges of the flow, the flow development length is comparable to the total lengths of many large blood vessels. The shear stress

on the wall of the tube is found to attain the steady state much before the time taken by the velocity profile to reach its steady-state value.

The analysis of a steady laminar flow of an inviscid, incompressible Newtonian fluid in the entrance region of the porous pipe indicates that the entry length is sensitive to wall Reynolds number. Entry length decreases with increase in the wall Reynolds number for injection, whereas for suction it increases with increase in the wall Reynolds number. For suction, a well-defined entry length is predicted for wall Reynolds number less than ten.

References

1. YOUNG, T — On the functions of the heart and arteries, *Phil Trans*, 1809, **99**, 1–31
2. PATEL, D J., GREENFIELD, J C., AUSTIN, W G., MORROW, A G AND FRY, D.L. — Pressure-flow relationships in the ascending aorta and femoral artery of man, *J. Appl Physiol*, 1965, **20**, 459–463
3. DEVANATHAN, R AND MANJULA, K.V. — *Mathematical model of blood flows in the entry region of arteries*, Karger monographs on atherosclerosis, No 15, pp. 273–281, 1990.
4. BJORNO, L AND PETTERSON, H. — Hydro- and hemodynamic effects of catheterisation of vessels II-Model experiments comparing circular and annular lumen area reduction, *Acta Radiol Diagnosis*, 1976, **71**, 749–762.
5. LLOYD, D R., JOHN, P AND DONALD, W C. — Analysis of pulsatile, viscous blood flow through diseased coronary arteries of man, *J. Biomech*, 1977, **10**, 339–353
6. KANAI, H., IIZUKA, M. AND SAKAMOTO, K — One of the problems in the measurement of blood pressure by catheter insertion. Wave reflection at the tip of the catheter, *Med. Biol Engng*, 1970, **8**, 483–496.
7. CAMPBELL, W.D. AND SLATTERY, J.C. — Flow in the entrance of a tube, *Trans. ASME, J. Basic Engng*, 1963, 41–46.

Thesis Abstract (Ph.D.)

Analysis of behavior of cement composites—Particulate and non-particulate considerations by S. G. Shashiprakash

Research supervisors: T. S. Nagaraj and B. K. Raghu Prasad

Department: Civil Engineering

1. Introduction

Concrete is used as a construction material since Roman times, but the knowledge of its nature and behavior so far did not receive their due share of introspection from materials science point of view. As the uses of concrete have become more widespread, so have the limitations of this wholly engineering approach become more apparent. Only recently, concrete technologists have focussed their attention on the internal structure of concrete. These investigations have confirmed that, ironically, one of the man's oldest and most widely accepted polyphase materials is also one of the most variable and complex.

With materials such as concrete answering all basic questions is not made easy because the constituents of concrete, quite apart from the concrete itself, are intrinsically highly variable in themselves. For most purposes, for reasons of economy, they cannot usually be changed very much and must be used more or less as they are found in nature. It is necessary and profitable to delve into the mysteries and try to understand the behavior of concrete. Any attempt to understand, interpret and generalize the behavior of concrete both in its preset and set states would enhance the potential use of concrete under diverse conditions.

It is the aim of this investigation, to understand, interpret and generalize the behavior of concrete within the framework of basic principles of material science.

2. Studies on concrete as a particulate material

This part of the investigation deals with the analysis of concrete as a particulate material Based on this analysis, an analogy has been brought out between saturated soil and fresh concrete, with respect to material constituents and physicochemical interactions[1]. It has been shown that clay in soils and cement in concrete interact with water. The coarse inert constituents are found to float in the matrix, diluting the physicochemical potential of the active material, *i.e*, clay in soils and cement in concrete. Such a mode of understanding has further led to the generalization of flow behavior of cement paste, mortars and concrete This generalization permits one to quantify the reduction in water content to achieve target flow, when coarse constituents are included to clay or cement; and also to take into account the physicochemical characteristics of cements at engineering level.

The next part of the investigation deals with the workability of concrete. Here, the behavior of concrete as it is studied in various tests is analysed. The analyses of various tests such as slump, flow table, compacting factor, Kelly ball, K-slump and Powers' remolding tests indicate that they are primarily measures of shear resistance. The possibility of having a 'One-point method' of determining normal consistency using Vicat's apparatus is suggested here. Cone penetrometer, hitherto used to determine the liquid limit of soils, is made use of for the determination of consistency, keeping in view the vague method of assessment of consistency using the Vicat's test. Since the mode of determination of the property is the same in both Vicat's and cone penetrometer methods, the latter has the potential of being a good alternative to the former. This needs to be probed in depth before an equivalent cone penetration is defined for normal consistency. It should also be possible to define equivalent cone penetrations for initial and final setting times of cement. Use of the cone penetrometer with modified cones, on mortars and concrete indicates that this test can be a good alternative to Kelly ball test. With a proper design of the cone, it should be possible to have a common equipment for both consistency of cement paste and workability of concrete.

Further, studies were conducted on superplasticized concrete. These deal with optimization of superplasticizer dosage and extension of workability of concrete using admixtures. Soil–concrete analogy is made use of in understanding the physico-chemical interactions in the cement–water–superplasticizer system Based on this, explanations are given for flocculation in cement–water system and hence for assessment of optimal dosage of superplasticizers[2]. A simple method of assessing optimal dosage of superplasticizers is suggested here (Fig. 1). Further, it is shown that it is possible to rejuvenate the workability of concrete even after two and a half hours after adding water, by the use of superplasticizer premixed with 0.5% sodium gluconate[3]

3. Studies on concrete as a non-particulate material

This is an attempt to link the micro and macro behavior through micromechanistic considerations of cement and water with the compressive strength–water–cement ratio relationships, enunciated in Abrams' law. The reexamination of Abrams' law indicates that, though, the deductions were based on experimental observations, the law has a sound theoretical basis. The generalization of Abrams' law done here is made use of in the proportioning of concrete mixes[4].

The next part of the investigation deals with the proportioning of concrete mixes. The various aspects studied here include the different factors considered in the mix proportioning and the different methods in vogue. Having observed the need for a method of re-proportioning of concrete mixes to achieve target workability and strength, a method is suggested which is designated as 'Generalized approach for mix proportioning'. This takes into account the physicochemical characteristics of cement and surface characteristics of aggregates. This method makes use of three generalized plots (Figs 2, 3 and 4), using which it is possible to get a wide spectrum of concretes with varied workability and strength ranges, based on the data of one trial mix. This method developed on a scientific base has been found suitable for both plain and superplasticized concretes (Tables I and II). It is hoped that this method will be applicable to flyash concretes also.

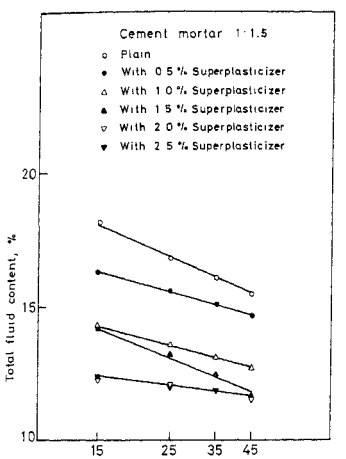

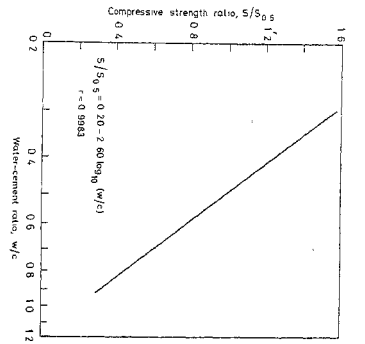

FIG. 1 Optimization of superplasticizer dosage

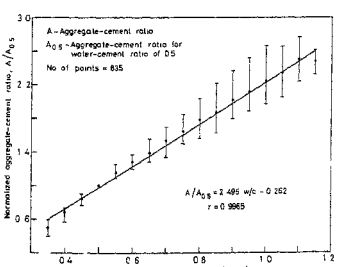

FIG. 3. Relationship between normalized aggregate–cement ratio and water-cement ratio.

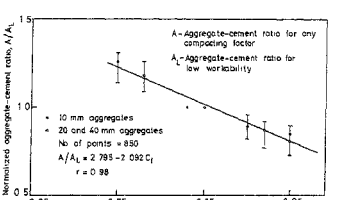

FIG. 4. Relationship between normalized aggregate–cement ratio and compacting factor.

4. Concluding remarks

The following specific conclusions were drawn from this investigation:

Concrete exhibits particulate characteristics in the fresh state and non-particulate characteristics in the hardened state.

There exists an analogy between saturated soil and fresh concrete. The flow behavior of cement paste, mortars and concrete can be generalized. The inert coarse constituents are found to dilute the

Table Ia
Details of concrete mixes

Water–cement ratio	*Aggregate–cement ratio*	*Compacting factor obtained*	*28-day strength (N/mm^2)*
a) ACC Cement *Target compacting factor=0·90*			
0·40*	4·68	0·77	37·68
0·45	4·20	0·89	35·06
0·50	4·81	0·88	29·56
0·55	5·41	0·87	25·80
0·60	6·02	0·86	21·53
0·70	7·26	0·86	18·46
b) Diamond Cement *Target compacting factor=0·85*			
0·40*	4·68	0·81	22·00
0 30	2·85	0·82	28·85
0·35	3·58	0·82	28·11
0 45	5·05	0·83	22·62
0·50	5·78	0·83	19·13
0·55	6·51	0·86	15·15

* Trial mix

Table Ib
Comparison between calculated and actual 28-day strength

Water–cement ratio	*Strength (N/mm^2)*		*Percentage difference over calculated strength*
	Calculated	*Actual*	
a) ACC Cement			
0.40	-	37·68	Reference mix
0·45	33·62	35·06	+4·28
0·50	30·52	29·56	−3·15
0·55	26·71	25·80	−3·41
0·60	23·71	21·53	−9·19
0·70	18·40	18·46	+0·33
b) Diamond Cement			
0·40	-	22·00	Reference mix
0·30	27·79	28·85	+ 3·81
0·35	24·69	28·11	+13·85
0·45	19·63	22·62	+15·23
0·50	17·82	19·13	+ 7·35
0·55	15·59	15·15	− 2·82

chemical potential of clay or cement. This mode of generalization takes into account the physicochemical characteristics of cements at engineering level.

The analysis of various workability tests indicates that they are primarily measures of shear resistance. Normal consistency of cement can be determined by a single point test. Cone penetrometer has the potential of being a good alternative to Vicat's test and may also be a workability test.

Optimal dosage of superplasticizer can be determined by simpler tests. Superplasticizers premixed with sodium gluconate can rejuvenate the workability of concrete even after two-and-a half hours.

Tabel II
Details of the superplasticized mix

Sl No.	Target values		Fluid–cement ratio	Aggregate–cement ratio	Results obtained		Percentage variation over target strength
	Strength N/mm²	Compacting factor			Strength N/mm²	Compacting factor	
With Conplast 337							
1.	15	0·92	0·87	9·35	15·11	0·89	1·00
2.	25	0·80	0·70	9·32	23·22	0·85	−7·00
3	25	0·92	0·70	7·25	24·33	0·92	−2·70
4.	25	0·97*	0·70	6·42	24·33	0·98	−2·70
5.	35	0·92	0·57	5·68	32·33	0·87	−7·60
With Prescon							
1.	15	0·92	0·87	9·00	17 44	0·89	16·27
2.	25	0·80	0·70	8·87	25·48	0·835	1·92
3.	25	0·92	0·70	6·90	26·28	0·93	5·12
4.	25	0·95*	0·70	6·42	24·67	0·94	−1·32
5.	35	0·92	0·57	5·40	32·67	0·93	−6·66

Note· (i) *indicates the compacting factor obtained using optimal dosage of superplasticizer in the trial mix.
(ii) Proportion of the fine to coarse aggregates is kept the same as that of the trial mix, in all the cases

The 'Generalized approach for mix proportioning' takes into account the physicochemical characteristics of cements and the surface characteristics of coarse aggregates. This method is found suitable for both plain and superplasticized concretes.

References

1. NAGARAJ, T S , SUNDARA RAJA IYENGAR, K.T. AND SHASHIPRAKASH, S.G. — Soil–concrete analogy—Principles and potentials, *Cem Concr. Res.*, 1989, **19**, 534–546.
2. NAGARAJ, T.S. SUNDARA RAJA IYENGAR, K.T. AND SHASHIPRAKASH, S.G. — Superplasticized concretes—An engineering approach for assessment of optimal dosage, *J. Irrig. Power*, 1987, **44**, 119–129
3. NAGARAJ, T.S. AND SHASHIPRAKASH, S.G. — Extended workability of superplasticized concretes for practical application, *55th R&D Session of Central Board of irrigation and Power*, Srinagar, Technical Session VIII, 1989, pp. 55–62.
4. NAGARAJ, T.S., SHASHIPRAKASH, S.G. AND KAMESWARA RAO, B. — Generalized Abrams' law. Invited paper for *RILEM Colloquium 'Properties of Fresh Concrete'*, Hanover, FRG, 1990, pp 242–252.

Thesis Abstract (Ph.D.)

Structural and related investigations of gel-derived ZrO_2-based ceramic composites by
V. S. Nagarajan
Research supervisor: K. J. Rao
Department: Materials Research Centre

1. Introduction

Zirconia, both partially stabilized and fully stabilized and ceramic composites containing fine particulates of ZrO_2 are known to possess improved fracture toughness (K_{IC})[1]. This is largely attributed to the

stress-induced tetragonal → monoclinic phase transformation[2] of ZrO_2. Ceramic processing by the sol–gel method[3] has become important in recent years. The work reported aims at the preparation and characterization of ZrO_2-based ceramics and composites obtained using the sol–gel route. The systems investigated in this work have been chosen keeping in view their potential for application. The systems investigated here include Y_2O_3–ZrO_2, CeO_2–ZrO_2, ZrO_2–SiO_2, ZrO_2–Al_2O_3–SiO_2, ZrO_2-cordierite and ZrO_2-hydroxyapatite.

2. Experimental

Fine ceramic powders in the above-mentioned systems were prepared using sol–gel method. The powders were compacted and sintered at higher temperatures in the case of Y_2O_3–ZrO_2, CeO_2–ZrO_2 and ZrO_2-hydroxyapatite systems. Hot isostatic pressing (HIP) was done in case of Ce–TZP samples. Vicker's hardness (V_H), and fracture toughness (K_{IC}) were measured using an indentation method. Biocompatibility of these sintered samples was evaluated using an *in vitro* cell test. The ZrO_2–SiO_2, ZrO_2–Al_2O_3–SiO_2 and ZrO_2–cordierite gels were studied for the thermally induced chemical and structural changes A number of characterization techniques such as X-ray diffractometry (XRD), scanning and transformation electron microscopy (SEM and TEM), thermogravimetry (TGA), infrared (IR) spectroscopy, magic-angle spinning NMR spectroscopy (MAS NMR) and computer simulation were used to elucidate a number of structural aspects, at various stages.

3. Results and discussion

The change in the nature of major phase observed during heat treatment in CeO_2–ZrO_2 gel has been found to be related to the presence of a barrier for transformation from metastable to stable regime[4] which in turn appears to be related to the diffusion barriers of Ce^{4+} in ZrO_2. The sintered or HIPed Y_2O_3 and CeO_2-stabilized ZrO_2 exhibit fracture toughness values ranging from 7–12 MPa $m^{1/2}$ with fine grain sizes. They are biocompatible as evidenced by an *in vitro* cell test Formation of $Ce_2Zr_2O_7$ (pyrochlore) in the case of 15 mole% CeO_2-stabilized zirconia polycrystal (15 Ce–TZP) has been interpreted as a spinodal decomposition using a chemical scheme The high value of K_{IC} observed in HIPed 15 Ce–TZP has been rationalized by a new toughening mechanism[5] leading to the probable decomposition of pyrochlore during crack propagation (Fig. 1).

Formation of tetragonal phase of ZrO_2 in the bulk ZrO_2–SiO_2 (Z/S) gels is influenced by the lower symmetry SiO_2 and by various physicochemical factors[6]. The crystallization studied *in situ* under electron beam heating[7] in a TEM confirms that the size of ZrO_2 particles are presence of hydroxyl groups influence the nature of the crystallized ZrO_2 phase. The molecular dynamics simulation results of Z/S system reveal an inherent tendency of Zr atoms towards clustering even at low concentrations. Also the oxygen environment of Zr suggests edge sharing of [$SiO_{4/2}$] tetrahedra at high ZrO_2 concentrations while at low concent-

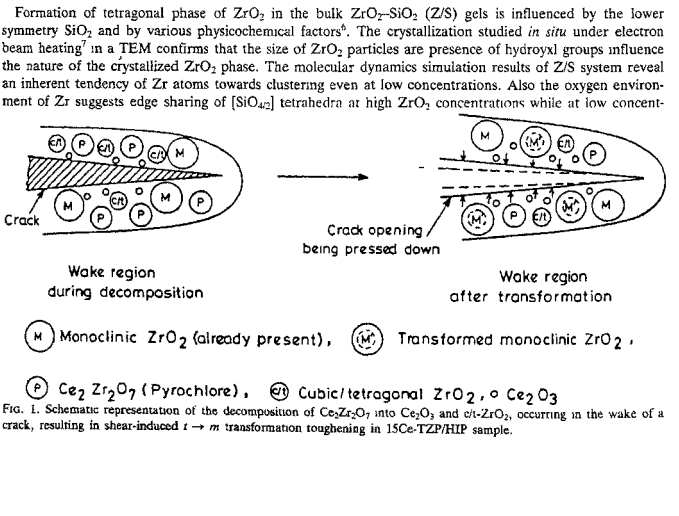

FIG. 1. Schematic representation of the decomposition of $Ce_2Zr_2O_7$ into Ce_2O_3 and c/t-ZrO_2, occurring in the wake of a crack, resulting in shear-induced $t \rightarrow m$ transformation toughening in 15Ce-TZP/HIP sample.

rations they are predominantly in corner-sharing geometry. Features suggesting the formation of zircon-type structures have been observed[8].

Formation of compounds at higher temperatures in the Al_2O_3–ZrO_2–SiO_2[9] and ZrO_2–cordierite[10] gel systems have been shown to be related to the various acid–base reactions between the oxides and the catalyst acid or base in the sol. A new approach based on molecular electronegativity differences of component oxides has been made to rationalize the observed reactions. Partial charges on oxygen in various oxides have been calculated using molecular electronegativities and are shown to be consistent with well-known basicities of component oxides and the observed reactions.

Hydroxyapatite (OHAp)-based composites toughened by gel-derived and commercial ZrO_2 additions have been investigated for prosthetic applications. The composites have been sintered and HIPed and higher K_{IC} (two to three times higher than pure OHAp) has been achieved. The composites are biocompatible. CaO which forms as a product of decomposition dissolves completely into ZrO_2 and stabilizes the latter in its cubic/tetragonal phase[11].

The work is hoped to help in designing toughened ZrO_2 composites by sol–gel route. The new chemical approach based on molecular electronegativities presented here is expected to help rationalizing the nature of high temperature products formed during heat treatment of gels The new mechanism of toughening proposed may prove a novel strategy for designing other ceramic composites.

References

1 CLAUSSEN, N., RUHLE, M AND HEUER, A. (eds) *Advances in ceramics*, Vol. 12, 1984, The American Ceramic Society, Columbus, Oh.

2. GARVIE, A C. AND HANNINK, R.H.J *Nature*, (Lond) 1975, **258**, 703–704.

3 BRINKER, C.J AND SCHERER, G.W. *Sol–gel science*, 1990, Academic Press

4. NAGARAJAN, V.S. AND RAO, K J. *J Mater. Res.*, 1991, **6**, 2688–2693.

5. NAGARAJAN, V S. AND RAO, K J. *Phil. Mag A*, 1992, **65**, 771–781.

6 NAGARAJAN, V.S AND RAO, K.J. *J Mater. Sci*, 1989, **24**, 2140–2146.

7. NAGARAJAN, V.S AND RAO, K J *Mater. Res. Bull*, 1991, **26**, 715–721.

8. DAMODARAN, K.V., NAGARAJAN, V.S. AND RAO, K.J. *J Non-Cryst. Solids*, 1990, **124**, 233–241

9. NAGARAJAN, V S AND RAO, K J. *J. Solid St Chem*, 1990, **88**, 419–428

10. NAGARAJAN, V.S AND RAO, K.J. *J Solid St. Chem.*, 1991, **94**, 149–162.

11 NAGARAJAN, V.S AND RAO, K J. *J Mater. Chem.*, 1993, **3**, 43–51.

Thesis Abstract (Ph.D.)

Voltage-limiting nonlinear resistors based on ZnO ceramics with chemically simplified formulations by N. Raghu

Research supervisor: T. R. N. Kutty
Department: Materials Research Centre

1. Introduction

Voltage-limiting nonlinear resistors, generally known as varistors, based on ZnO ceramics, have found extensive applications as surge-protecting devices both in electronic circuits as well as in power systems[1]. Their utility is widely expanding in various fields extending from medical, defence to consumer and professional electronics. However, the working formulations and critical processing steps of stable varistors are of proprietary nature and are hardly dealt with in open literature. The reported varistor compositions

contain up to ten chemical constituents in addition to ZnO and the function of individual constituents is not well understood In this respect, simplified varistor formulations are necessary which however invariably lead to resistors with low nonlinearity The main reason for the incomplete understanding is the lack of knowledge about the chemical origin of nonlinear resistivity. Thus, the present work concentrates on the science of voltage-limiting resistors by way of understanding the role played by individual additives in ZnO-based varistors with simplified compositions and at the same time having high nonlinearity.

2. Experimental techniques

High-purity ZnO has been prepared from three different routes after purifying the Zn solution by fractional precipitation. The resultant ZnO is characterised using XRD (Philips PW 1050/70/76), transmission electron microscope (Philips EM 301), electrochemical analysis for nonstoichiometry determination and by spectroscopic techniques(EPR–Varion 109, Optical–Shimadzu UV 210A double beam spectrometer) In preparing the additive phases such as cobaltates, manganates, chromates, and cuprates enough care has been taken to maximise the oxygen content. The additives are thoroughly mixed with ZnO and discs of 10 mm dia and 2 mm thick are sintered at 1100–1350°C for one to four hours Ohmic contacts are obtained using electroless silver coating. The I–V curves are carried out using a home-built instrument. The C–V measurements are made using Genrad 1658 digibridge.

3. Results and discussion

Since nonlinear property is exhibited only by polycrystalline materials, high-sinter density and controlled grain size are important which in turn require starting powders of submicron particles. Thus, three chemical routes of preparation are chosen so as to find the influence of exo- or endothermic reactions as well as the influence of back reaction by the evolved gases, on the nonlinearity, particle size and the reactivity of the resulting ZnO powders. The as decomposed oxalate-derived powder shows low particle size (~ 25 nm), higher strain value and larger nonstoichiometry (δ_{Zn}~ 25 ppma). Ex-nitrate ZnO shows strong particle agglomeration although the size of the particles are ~50 nm. Although the ex-carbonates are strain free they exhibit strong agglomeration and largest particle size (~70 nm). Nonstoichiometry of ex-carbonate and nitrate are <3 ppma. Post-preparative annealing of the ZnO powders at 900°C leads to higher nonstoichiometry in ex-carbonate and nitrate-derived samples. Annealed samples react favourably in achieving higher sinter density at comparatively lower temperatures of sintering. For a given additive, the lower temperature of sintering is found to be advantageous in stabilizing high nonlinearity in the current–voltage characteristics[2].

ZnO varistors are prepared[3] with a single-phase additive, namely, $MCoO_{3-x}$(M=Ba or Sr). These forming phases have been chosen as a model system to understand the role played by the element of larger ionic radii (Ba^{2+} or Sr^{2+} in this case) which serves as the 'varistor-forming' constituent and a transition metal element with multivalency as the 'varistor-performing' constituents. The oxygen-deficient orthorhombic $BaCoO_{3-x}$, where $x > 0.15$, leads to ceramics with poor microstructure and low nonlinearity. Whereas the use of oxygen-rich $BaCoO_{3-x}$, where $x < 0{\cdot}15$, having hexagonal perovskite structure as the additive, gave rise to nonlinear index > 20. Faster cooling rate following sintering as well as proper post-sintering annealing gave rise to ceramics with α up to 45 (Fig. 1). EPR and optical spectral studies lend support to multivalence state of Co, *viz.*, Co^{2+} and Co^{3+} in the sintered ceramics. The preferential presence of CO^{3+} in the grain boundary regions is indicated by the grain size dependence of the EPR spectral characteristics. The overwhelming presence of Ba^{2+} ions at the grain boundaries as shown by the electron microprobe analysis is explained on the basis of limited solubility of BaO in ZnO wherein the solubility is inversely proportional to the temperature. CO^{3+} is compensated by V_{zn} and is inferred from the appearance of the EPR signals of hole centre with $g \sim 2.010$. Thus, the presence of excess V_{zn} at the grain boundary region produces the double Schottky-type potential barrier whose width decreases with applied voltage. Furthermore, the presence of hole centres near the grain boundary region squeezes the barrier so that electron tunneling takes place at higher voltages leading to nonlinear resistivity

The above model system containing the single formulating additive phase has been extended to other simplified compositions with the well-characterised additive phases such as $BiCoO_{3-x}$, $Ln_{1-y}M_yCoO_{3-x}$ (Ln = Lanthanides, M = Ba or Sr), $MMnO_{3-x}$, $BaCrO_4$ and $YBa_2Cu_3O_{7-x}$. All these additives lead to

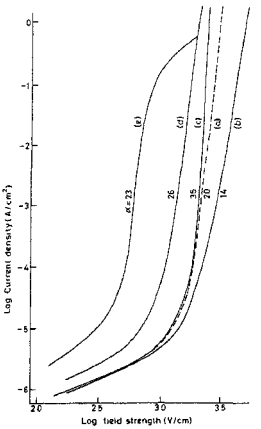

FIG 1 Post-sintering effect of (a) 1100°C for 2h-sintered ZnO+1% $BaCoO_{2.96}$ ceramic. Taken to 1130°C for 15 min and cooled at (b) 20°C/min, (c) 100°C/min, (d) Taken to 1130°C for 45 min, and (e) to 1200°C for 30 min. Samples (d) and (e) cooled at 100°C/min.

nonlinear ceramics with high α values in the range of 15 to 35 indicating that they are not just primitive varistors. The investigations with these additives confirm the conclusions drawn from the ZnO–$BaCoO_{3-\delta}$ system. The importance of higher valency state of the transition metal element is also confirmed from the better performance of ZnO + Bi_2O_3 + Co_3O_4 + MnO_2 as compared to ZnO + Bi_2O_3 + CoO + MnO having the same concentrations of additives. These results lead to a model[4] wherein the oxygen produced *in situ* by the decomposition of the nonstoichiometric additive is chemisorbed on the ZnO particle surface producing the negatively charged surface states. These surface states are compensated by the ionized donor states towards bulk so that the depletion region is produced. In turn, the depletion regions give rise to the formation of potential barriers at the grain boundaries. The preferential presence of the high valent states of the transition elements at the grain boundaries is compensated by V_{Zn} and hence the potential barrier is preserved even after sintering and desorption of oxygen takes place from the surface. The ready formation of nonlinear resistors is observed only when ZnO powders annealed above 900°C have been used which contained nonstoichiometric value of δ_{Zn}>10 ppma. This observation is accounted for in terms of the higher concentration of native donor states, mostly oxygen vacancies, as established by the EPR results, in the grain interiors than in the grain boundary regions. Faster cooling rates enhance the donor density which, in turn, narrow down the width of the depletion region layer and enhance the electron tunneling probability.

Varistors are also formed by co-sintering ZnO and spinels having negative temperature coefficient (NTC) in resistance[5]. The latter phases are chosen because the transition metal constituents can form separate spinel phases with NTC properties such as $NiMn_2O_4$, $NiMn_{2+x}O_4$, $CuMn_2O_4$, $ZnCoMnO_4$, $Zn_{0.5}Co_{0.5}MnCrO_4$. Steady-state I–V characteristics of NTC ceramics exhibit negative differential resistance (NDR) above a certain applied voltage. In the NDR region, the voltage decreases with rise in current as well as the body temperature of the ceramics. Mixed-phase ceramics of ZnO+NTC spinels progressively renders the slope of the NDR region positive with ZnO content. Under critical compositional and processing conditions abnormally high values of 100–150 can be achieved. The thermal characteristics of these ceramic composites show favourable stability because the heat dissipated is always higher than the heat generated even at fairly higher ambient temperature conditions. The I-V characteristics of these mixed-phase ceramics

are accounted for in terms of the combined influence of the field as well as the thermal effect

The voltage-limiting properties[6] of ZnO ceramics doped only with CuO have also been analyzed. Cu in the range of $< 1\%$ is incorporated by dipping porous ZnO pellets in Cu solutions followed by final sintering Properly processed ceramics show α in the range of 15–40. TEM studies give evidence of the presence of extensive dislocation networks. The origin of these dislocations is explained on the basis of decreasing solubility of CuO on cooling from the sintering temperatures leading to the exsolusion of the impurities The latter gives rise to lattice strain which can be partly removed by the formation of the dislocation networks. Higher concentration of the impurities can be expected at the dislocations because of the space charge associated with the line defects of ionic solids. The variation in the photoluminescence spectra with concentration indicates the presence of both Cu'_{Zn} and $Cu'_{Zn}Cu^{\cdot}_{i}$ centres at low concentrations, whereas Cu'_{Zn} dominates at higher Cu levels. The preferential accumulation of Cu'_{Zn} at the dislocations leads to non-radiative transitions and quenching of the green luminescence. The EPR spectra support the presence of hole centres being stabilized by Cu^{3+} species at the grain boundary regions. Higher α values observed in ZnO-doped Cu systems are accounted for in terms of the potential barrier prevailing around the dislocations through which tunneling may occur. This is in addition to the potential barrier existing at the grain boundary regions.

The present studies clearly indicate that high nonlinearity can be obtained in ZnO ceramics prepared from single-forming additive phases. However, one and the same mechanism cannot adequately account for the wide range of α values exhibited by ZnO ceramics.

References

1. GUPTA, T K — Applications of Zinc oxide varistors, *J Am Ceram Soc.*, 1990, **73**, 1817–1840

2 KUTTY, T R N AND RAGHU, N. — Characterisation of the chemically prepared ZnO powders in relation to the nonlinear resistors, *J Euro Ceram. Soc*, 1993, **11**, 161–170

3 KUTTY, T R N. AND RAGHU, N — ZnO-based voltage-limiting resistors with $MCoO_x$ (M = Ba, Sr) as the only forming additive, *Mater Sci Engng B*, 1992, **13**, 181–197

4. RAGHU, N. AND KUTTY, T.R.N. — Realtionship between nonlinear resistivity and the varistor forming mechanism in ZnO ceramics, *Appl Phys Lett*, 1992, **60**, 100–102

5 RAGHU, N AND KUTTY, T R N. — Varistors based on mixed phase ceramics containing ZnO and negative temperature coefficient spinels, *Appl Phys. Lett*, 1991, **58**, 1050–1052

6. KUTTY, T.R N AND RAGHU, N. — Varistors based on polycrystalline ZnO Cu, *Appl Phys Lett*, 1989, **54**, 1796–1798.

Thesis Abstract (Ph.D.)

Engineering behaviour of fine-grained soils with chemical additives and the governing physico-chemical mechanics

by K. Vijaya Bhaskar Raju
Research supervisors: P. V. Sivapullaiah and A. Sridharan
Department: Civil Engineering

1. Introduction

The aim of the present investigation is to study the influence of chemical additives on the engineering behaviour of saturated fine-grained soils with high initial water content and to understand the physico-chemical mechanisms governing the same. The chemical additives used include both which can induce reversible and irreversible changes in the soil pore–fluid system. Among the chemical additives which can

induce reversible changes like changes in electrolyte concentration and type of exchangeable ions are chlorides and hydroxides of mono- and divalent cations. The irreversible changes produced by chemical reactions between soil and chemical additive have been mainly brought through lime[1] alone or admixtures of lime and other inorganic chemicals[2].

2. Theoretical considerations

The effective stress concept provides satisfactory basis for understanding the behaviour of soils. This effective stress concept can be summarized as

$$\sigma' = \sigma - u$$

where σ' = effective stress,

σ = applied external pressure, and

u = pore water pressure.

It is well established that both attractive (A) and repulsive (R) forces of electrical nature exist between clay particles. Sridharan and Rao[3] modified the effective stress equation as follows.

$$\bar{c} = {}^{m}\sigma\, a_m = \alpha - u\bar{u}_a - \bar{u}_w - R - A$$

where $\bar{c}$ = effective contact stress

${}^{m}\sigma$ = mineral-to-mineral contact stress

σ = externally applied pressure on unit area

$\bar{u}_w$ = effective pore water pressure

$\bar{u}_a$ = effective pore air pressure

a_m = fraction of the total inter-particle contact area that is mineral-to-mineral contact or

$\bar{c} = \sigma' + \sigma''$

where σ' = conventional effective stress, and

σ'' = effective stress.

In this investigation, this equation has been used to formulate the mechanisms controlling the strength and volume change behaviour of soils with chemical additives.

3. Results and discussion

It has been shown that the addition of any chloride brings down the liquid limit and free swell index values and increases the shrinkage and plastic limits for black cotton soil and the changes have been explained based on diffuse double layer considerations. For red earth, addition of chloride reduces the liquid limit, free swell index and plastic limit and marginal increase in the shrinkage limit, which are more due to the effect of fabric changes than due to the effect of diffuse double layer. Addition of hydroxides also reduces the liquid limit (except magnesium oxide) and increases the plastic limit, shrinkage limit and free swell index of black cotton soil. For red earth, liquid limit, plastic limit and free swell index values are reduced, while shrinkage limit is increased on addition of hydroxides. Also, it was noticed that, generally, hydroxides offer enhanced liquid and shrinkage limits than their corresponding chlorides for black cotton soil and red earth. This has been attributed to flocculation of clay particles on the addition of hydroxides. A method to identify the fabric of soils has been developed based on their liquid and shrinkage limits (Fig. 1).

It has been shown that the volume change behaviour of black cotton soil in the presence of chlorides and hydroxides is controlled by different mechanisms. The volume change behaviour of black cotton soil in the presence of chlorides is primarily controlled by diffuse double layer forces, whereas the behaviour of black cotton soil in the presence of hydroxides is primarily controlled by the shearing resistance at particle level. Immediately after the addition of lime, the liquid limit of BC soil decreases because of depressed double layer but increases with time. The increase with duration of curing time has been

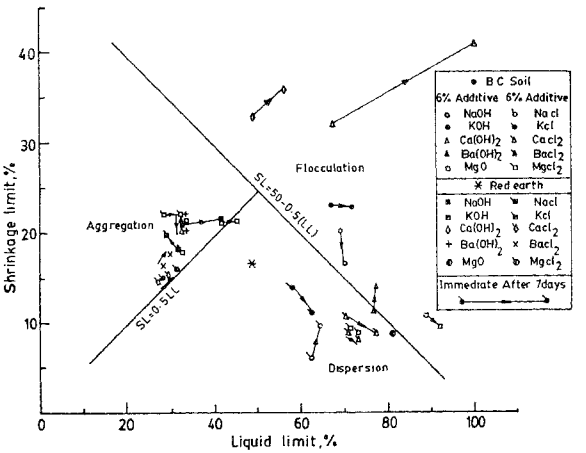

FIG 1. Identification of nature of fabric.

attributed to changes in fabric towards more flocculated one. The same trend is observed for black cotton soil with higher percentage of clay. But, for black cotton soil with lower percentage of clay, the liquid limit increases even initially, and very slightly with time. In the case of kaolinite, because of low cation exchange capacity, the liquid limit increases immediately and also with time. For soils where the diffuse double layer effects are less significant, addition of lime increases the liquid limit immediately due to flocculation.

Immediately on addition of 1% lime, the plastic limit of BC soil has increased and remains unaffected with further additions. This indicates that the increase in shearing resistance at particle level controls the plastic limit behaviour unlike in the case of liquid limit where the effect of diffuse double layer is predominant.

Shrinkage limits of all the BC soils increase even initially on addition of lime, since the shrinkage limit is primarily controlled by fabric changes than by changes in double layer.

Since the completion of consolidation test takes time, during which time the pozzolanic reaction can take place, the effect of duration of pressure increment was varied from 1/2 to 48 hours for black cotton soil with 6% lime. It was noticed that the primary consolidation was over even with duration of pressure increment of 1/2 hour. The secondary compression coefficient decreases significantly with increase in the duration of pressure increment. From the consolidation tests on black cotton soil with various percentages of lime, it was observed that the magnitude of compression decreases with increase in lime content.

From the consolidated undrained shear test, it was shown that while the cell pressure has profound effect on the pore water pressure changes, it has marginal effect on the deviator stress for lime-treated soils. The failure deviator stress increases with increase in the percentage of lime, which increases further with curing time. The effective strength parameters increase with increase in lime content, indicating an

increase in the bond strength between particles. Curing with more than 6% lime, the cohesion values increase further and the angle of shearing resistance values remain unaffected.

The influence of substitution of lime by other chemicals on the basic and engineering properties of black cotton soil has been reported[2]. The chemicals used for substitution are sodium hydroxide, sodium chloride, sodium silicate, potassium hydroxide and magnesium oxide.

Substitution of lime with other chemicals which increases the pH enhance the scope for lime stabilization of soils in increasing their strength. Magnesium oxide accelerates the lime–soil reactions.

The behaviour of lime-treated soils of the same liquid limit having different clay minerals and grain size distribution has been examined. It has been shown that the lime reactivity of the soil can be assessed better based on changes in the basic properties on lime treatment rather than its liquid limit.

4. Conclusions

This work brings out the effect of chemical additives on the basic and engineering properties of fine-grained soils at high water content which can be explained using diffuse double layer theory and fabric changes. Depending upon the nature of chemical additives the mechanisms controlling the properties get altered. Lime significantly improves the engineering behaviour of expansive black cotton soil even at high water content. The optimum lime content is found to be 6% viewed from basic and volume change behaviour whereas from strength consideration, it is seen that even 12% of lime significantly improves. Effect of lime can be enhanced by judiciously selecting other chemical admixtures.

References

1. BELL, G — Stabilization and treatment of clay soils with lime, Part 1–Basic principles, *Ground Engng*, 1988, **21**, 10–15.
2. DAVIDSON, D. T., MATEOS, M. AND BARNES, H. F. — Improvement of lime stabilization of montmorillonitic clay soils with chemical additives, *Highw. Res. Rec. Bull.*, 1960, **262**, 33–50
3. SRIDHARAN, A. AND RAO, G. V. — Effective stress theory of shrinkage phenomena, *Can. Geotech. J.*, 1971, **8**, 503–513

Thesis Abstract (M.Sc. (Engng))

Electrical swithching—Instrumentation and investigations by Ranajit Chatterjee

Research supervisors: S. Asokan and A. Kumar
Department: Instrumentation and Services Unit

1. Introduction

Electrical switching is an interesting phenomenon, referring to the transition in certain materials, from a high resistance state to a comparatively low resistance state under an electric field. The swithching can be reversible (threshold type) or irreversible (memory type). Many amorphous semiconductors which exhibit switching[1] are found to have applications in the fields of information storage and power control devices[2].

Experimental investigations on the electrical switching characteristics of materials, like the switching voltage, temperature dependence of switching, etc., are important, for selecting a suitable material for a particular application.

The present work deals with the development of a PC-based system for studying I–V characteristics and switching in solids. The system built is used for studying the electrical switching in certain chalcogenide glasses.

2. Instrumentation

The system consists of a programmable constant current source capable of supplying up to 200 m Amp current at a compliance voltage of 1000 V. The stability of the set current is of the order of 1 micro Amp. The required current settings are achieved through an IBM PC XT *via* parallel I/O ports. The system can also be operated in the pulse mode where the pulse width can be programmed, with a lower limit of about a micro second.

The sample is held in a cell, between a flat plate electrode and a point contact electrode. The set current is passed through the sample and the voltage across the sample is measured using a meter which is interfaced with the PC using IEEE 488 bus. The sample current is dropped across a standard series resistor and the voltage developed is measured by a similar arrangement.

A resetting current pulse of variable magnitude (0–200 m Amp) and width (1 μs to 65 ms) can also be applied to the sample to bring it back to the initial high resistance state in case of memory switching.

The set up also includes a heating arrangement with a controller, to study the switching characteristics at different temperatures. The controller uses pulse width modulation for controlling sample temperatures in the range 300–500 K, with an accuracy better than 1% of full scale. The temperature setting and measurement are also done through the PC, using parallel port interfaces. The provision for high-temperature operation is incorporated to study the thermal stability of the parameters like switching voltage.

The system software is written such that the experiment is fully automatic. Once a sample of a given thickness is mounted in the cell and the mode of operation and other parameters of the experiment like the maximum current, current increment step, resetting pulse specification (fixed or variable), number of switching cycles with resetting, temperature limit and temperature increment, etc., are specified, the experiment is carried automatically by the PC and the required characteristics are plotted on the screen. Data files are also created if needed. The user can also alter any parameter during an experiment.

3. Results and discussion

Investigations are undertaken on the switching characteristics of two chalcogenide glassy systems, As_xTe_{100-x} ($25 \leq x \leq 60$) and $As_xTe_{100-x-y}Se_y$ ($25 \leq x \leq 60$, $10 \leq y \leq 25$).

In the As_xTe_{100-x} system ($25 \leq x \leq 60$), all the glasses are found to exhibit a current-controlled negative resistance with memory, rather than sharp switching. It is found that the threshold field E_t increases with the arsenic content linearly and there is a slope change at a composition $x=40$. The variation of the threshold field E_t with composition can be explained on the basis of the changes in the local structure of As_xTe_{100-x} glasses with composition. It is also observed that with temperature the threshold field E_t comes down linearly. The temperature dependence of E_t of the As_xTe_{100-x} glasses is consistent with that observed in other chalcogenide glasses[1].

$As_xTe_{100-x-y}Se_y$ glasses also exhibit a current-controlled negative resistance with memory. For a fixed Se content (y=10, 15, 20 and 25), threshold field is found to increase with the arsenic content x. Further, the field is also found to increase with increase in Se content. Among the samples studied, only one sample ($As_{40}Te_{30}Se_{20}$) shows a very sharp memory switching without any prominent negative resistance region.

In both the glass systems, a pulse of around 100 milli amps magnitude and 10μs width is found to bring the samples back to the initial high-resistance state, after switching. After resetting, the switching characteristics are found to be repeatable. The variation in the threshold field during cycling is found to be around ± 5%.

The present investigations reveal that the $As_{40}Te_{30}Se_{20}$ glasses, because of their sharp switching, may be interesting from the application point of view.

References

1. FRITZSCHE, H. In *Amorphous and liquid semiconductors* (J. Tauc, ed.), 1974, pp. 221–312, Plenum.

2 ADLER, D. *Scient. Am.*, 1977, **236**, 36–42.

Thesis Abstract (M.Sc. (Engng))

Power flow and sensitivity analysis in MTDC-AC system by V. Kalyanaraman
Research supervisor: K. R. Padiyar
Department: Electrical Engineering

1. Introduction

HVDC power transmission[1] has several advantages over AC transmission particularly for long-distance bulk power transmission and asynchronous interconnection of power systems. A major feature is the fast controllability of power which can be used effectively for improving the system security. Multiterminal DC (MTDC) systems contribute to better economy and flexibility of system operation thereby increasing the scope of application of HVDC links.

The planning of MTDC systems requires detailed studies involving power flow analysis in AC/DC systems. The approach to the solution of power flow problem in AC/DC system is broadly divided into two categories: (1) simultaneous or unified, and (2) sequential or alternating methods. The latter approach is widely used and involves the iterative solution of AC and DC systems separately and alternately until convergence is obtained.

There are several lacunae in the development of power flow analysis in MTDC systems as reported in the literature. A major weakness is the lack of adequate appreciation for the nature of the differences and similarities in the structure of AC and DC systems and their operation. Firstly, there is no distinction between the control and scheduled variables. In AC systems both the control and scheduled variables are the same (P_g), V_g (at the generator terminals). But in DC systems there are two control variables per terminal (transformer tap 'a' and the control angle 'θ') and these are used to schedule some other variables such as Voltage (V_d), current (I_d), power (P_d), reactive power (Q_d) or AC bus voltages (V). Secondly, there is no clear difference between the control and network equations. Thirdly, an overdetermined set of variables like V_d, I_d, cos θ, ϕ and a has been used to characterise the state of operation of the DC system[2]. This can be confusing because all the variables are not independent. The choice of state variables for the DC network can be limited to V_d or some other related variables. The other shortcomings are the use of inflexible per unit system where the base AC and DC voltages are related. As only one base DC voltage can be used in a connected MTDC system this implies a fixed AC base voltage which is inconvenient. Further, the handling of constraints on different variables such as I_d, a, θ, V, etc., has not been given satisfactory consideration in the literature available so far.

With the rapid increase of HVDC utilization in the electric utility for either transmission or back-to-back applications, the relative portion of the DC power to the total system power is increasing. The SCR, defined as the ratio of the short-circuit MVA at the converter bus to the DC power in MW, is continuously decreasing. The operation of HVDV converter connected to such a weak station poses many problems. Among them, voltage instability is the most important one. The problem of maintaining stable voltage is related to the problem of maintaining proper reactive power balance or the adoption of suitable converter control strategy can help in overcoming the voltage instability problems.

The steady-state analysis of voltage stability can be performed using the concept of voltage stability factor (VSF) which is defined as the ratio of the incremental change in AC voltage V to a small change in the shunt susceptance B_c at a specific power level. Positive values of VSF indicate stability while negative values indicate instability. Padiyar *et al*[3] have generalized this analysis by defining VSF as a matrix for multiterminal systems. They have considered the existence of mutual VSF which can also influence voltage collapse at a terminal other than the voltage setting terminal (VST). However, a detailed study of voltage stability influenced by converter controls in MTDC system is not yet reported in literature.

Maintaining of system security is an important aspect in the modern operation of power system. Proper regard to line flows must be given particularly following a contingency. If the line flow violates limits, it may lead to cascade tripping and consequently to system black out. The earlier approach was to adjust the generation which was originally operating at a value where the generation cost was minimum. Because

of the adjustment the operating costs become higher With the introduction of MTDC systems, advantage can be taken of the fast controllability of power in DC systems, which can adjust the AC line flows. Linear AC power flow has been widely used for contingency analysis because of linearity, speed of solution and the use of superposition for multiple contingencies. Use of this method for relieving network overloads by HVDC control needs to be studied.

The objectives of this work were:

(i) To study the formulation and solution of power flow in MTDC-AC systems under both steady state and dynamic conditions to overcome some limitations described earlier.
(ii) To investigate the problems of voltage instability through sensitivity analysis.
(iii) To examine alleviation of AC line overloads through HVDC control using linear programming technique.

2. Contribution of the thesis

1) A new and general approach for performing power-flow analysis for MTDC-AC systems is described which takes into account several constraints and control strategies. It is shown that under steady-state conditions when two control variables (θ, a) per terminal are available, the solution of the MTDC-AC power flow is obtained by solving the DC network first using one set of specifications (P_d or I_d and V_d) and subsequently solving the AC network first using also the second set of specifications (θ, $Q_d \cos \phi$ or V_i. Using the sensitivity information based on two DC and two AC network solutions, it is possible to eliminate the constraint violations by revising from the second set of specifications and also the V_d at VST, if necessary.

Only under dynamic conditions when transformer tap is not available for fast control, the DC and AC network equations are coupled and have to be solved simultaneously for better convergence characteristics.

2) A sensitivity matrix is formed which relates the control and other variables to specifications. Using this matrix, VSF matrix is obtained which can be used to predict voltage instability. Sensitivity matrix can be used for rescheduling specified variables to eliminate the constraint violations. However, sensitivity matrix is used to form matrix of voltage stability factors (VSF) which can be used to study voltage collapse problems at the converter buses in an MTDC system. Voltage stability analysis is illustrated by taking up the case study of a four-terminal MTDC system. Different converter control strategies are investigated with regard to improving the voltage stability.

3) A simple technique using linear programming is proposed for rescheduling power flows in HVDC lines to remove overloads in AC lines following a contingency.

References

1. PADIYAR, K R. *HVDC power transmission systems–Technology and system interactions*, 1990, Wiley Eastern.

2 ARRILLAGA, J , ARNOLD, C.P. AND HARKER, B. J. *Computer modelling of electrical power systems*, 1983, Wiley

3. PADIYAR, K. R AND SREEDHAR, P N Voltage stability analysis of multiterminal DC systems, *Sixth National Power System Conf.*, Bombay, India, August 1990, pp. 64-69

Thesis Abstract (Ph.D.)

Ion assisted deposition of oxide thin films by M. Ghanashyam Krishna
Research supervisors: S. Mohan and K. Narasimha Rao
Department: Instrumentation and Services Unit

1. Introduction

Novel deposition techniques and new materials are two very important aspects in the development of

optical thin film devices. Hence, they have received a lot of attention right through the development of the science and technolgy of thin films Although dielectric oxides constitute only a very small percentage of the materials used for optical devices, they have proved to be much superior to numerous other materials by virtue of their hardness, durability, refractive index, low extinction coefficient, etc. They have the additional advantage that with a proper selection of deposition process and process parameters the above-mentioned properties can be tailored to suit specific applications. A number of physical vapour deposition techniques have been used to deposit oxide thin films. But better control over the properties has been achieved only by the use of ion-assisted deposition processes. This is a consequence of the simple manner in which ion source parameters can be controlled to obtain the desired properties[1–5].

The objective of the present work is to study the variation in properties of titanium and zirconium dioxide thin films deposited by ion-assisted deposition and reactive electron beam evaporation in neutral oxygen atmosphere.

2. Experimental procedure

The films were prepared in an oil diffusion pumped chamber which could give pressures of the order of 10^{-6} torr. The films were coated on fused silica substrates. The source to distance was 28 cm. Zirconia films were coated using ZrO_2 as the starting material and titania films using TiO as the starting material. Substrates were heated during deposition using a radiant heater Oxygen ions were produced using two different sources: (1) a Heitmann-type cold cathode discharge source (HIS), and (2) a broad beam high-energy Kaufman-type ion source (KIS). The major differences between the two sources are: (1) The energy and current density of ions can be independently controlled in the KIS whereas it is not possible in the HIS, and (2) The energy of ions in the HIS is less than 100 eV but current densities up to 2 mA/cm^2 can be obtained The KIS can produce ions of energy up to 1500 eV and lower current densities. The films were characterized for the following properties: refractive index, extinction coefficient, packing density, optical inhomogeneity, optical band gap, structure and stoichiometry.

Zirconia and titania thin films were deposited at current densities up to 1 mA/cm^2 using the HIS and in the energy range 0 to 700 eV and current densities up to 220 $\mu A/cm^2$ using the KIS. The starting material was evaporated from an electron beam source. The upper values for energy and current density were set by the deterioration in optical properties.

3. Results and conclusions

The major results of the work have been summarized in Tables I and II.

It was observed in the case of zirconia thin films that the refractive index increased with increase in energy and current density and saturated beyond certain critical values. The extinction coefficient which was initially low increased drastically beyond the critical values. The neutral oxygen and HIS-deposited films showed much lower indices and extinction coefficient than the KIS films. They also exhibited optical homogeneity. The KIS films however showed a transition from negative to positive inhomogeneity both with increasing energy as well as current density. It was seen that even the inhomogeneity exhibited critically it in its behaviour with the films at only one energy or current density resulting in homogeneous behaviour. Optical band gap calculations have shown that it is strongly energy dependent. It was observed that the values approached that of the bulk up to 500eV beyond which a decrease in gap values was observed.

All as deposited films as were X-ray amorphous and annealing to 500°C resulted in crystallinity. Two significant observations were made during this study: (1) The films showed crystalline inhomogeneity (*i.e.*, presence of more than one crystalline phase) at any post-deposition annealing temperature > 500°C, and (2) the cubic phase formed at low annealing temperatures (500°C) in the neutral oxygen deposited as well as the KIS films. For the first time infrared reflectance measurements were used to characterize phase compositions of the films. The refractive index decreased with an increase in annealing temperature whereas the extinction coefficient increased. The packing density also showed a decrease with increasing annealing temperature.

Table I
Results on zirconia thin films

	Neutral		*HIS*		*KIS*	
	As dep.	*Anneal*	*As dep.*	*Anneal*	*As dep*	*Anneal*
Ref. index	L	D	L	D	H[1]	VL
Extinction coefficient	L	I	L	I	H[2]	SI
Structure	Am	M+C (500°C) M+T (750°C) M (850°C)	Am	M+T At all annealing temperatures	Am	Most films show M Some films show cubic structure

L: Low, D: Decrease, H: High, VL: Very little change, SI: Slight increase, I: Increase, Am: Amorphous, M: Monoclinic, T: Tetragonal, C: Cubic.
[1]Saturates beyond critical value. [2]Increases beyond critical value

Table II
Results on titania thin films

	Neutral	*HIS*		*KIS*	
	As dep	*As dep*	*Heated*	*As dep*	*Anneal*
Ref. index	L	L	H	H[1]	VL
Extinction coefficient	L	L	L	L[2]	VL
Structure	Am	Am	Am	Am	All films show anatase structure

L: Low, H: High, VL: Very little change, Am: Amorphous,
[1]Decreases beyond critical value. [2]Increases beyond critical value.

Titania films deposited in neutral oxygen atmosphere showed much lower indices than the corresponding bulk material and very high absorption. It was found that the films deposited using the HIS had lower absorption than the neutral oxygen-deposited films. The index variation was, however, insignificant. It was observed that to a limited extent both in refractive index as well as the extinction coefficient a critical value of current existed beyond which there was a deterioration in optical properties. Films deposited on to heated substrates with simultaneous ion bombardment showed much better properties. At 200°C the films had a refractive index which was closer to that of the bulk, but the extinction coefficient was not affected significantly. All titania films were homogeneous independent of deposition conditions. It was observed that the effect of increasing the substrate temperature was much more pronounced than that of increasing the discharge current at a fixed temperature. The KIS titania films had much higher indices than the HIS films. This was true for films deposited at ambient as well as high temperatures. It was, however, found that the degradation in film properties occurred at much lower bombardment levels than for zirconia films. Even in the case of titania films the existence of a critical value for energy and current density has been demonstrated. The films were X-ray amorphous. Post-deposition annealing revealed that the films were anatase in nature.

A limited number of films were subjected to laser-induced damage threshold measurements using photoacoustic spectrometry. It was found that although the KIS films had a higher damage threshold the absolute values were still low. Since only a few samples were tested no definite trend could be established.

Finally, the experimental observations were fitted into a few currently used models for ion-assisted deposition. It was found that most of the observations fitted into a model which predicts the momentum transfer mechanism as being the dominant one in ion-assisted deposition processes

References

1	PULKER, H. K.	Characterization of optical thin films, *Appl Opt.*, 1979, **20**, 1969–1977
2.	PAWLEWICZ, W. T., MARTIN, P. M., HAYS, D. D. AND MANN, I. B.	Recent developments in reactively sputtered optical thin films, *Proc. Soc Photo-Opt. Instrum. Engng*, 1982, **325**, 105–112
3	RUJKORAKARN, R. AND SITES, J. R	Crystallization of zirconia thin films by thermal annealing, *J. Vac. Sci Technol. A*, 1986, **4**, 568–572
4.	MARTIN, P. J.	Ion-based methods for optical thin film deposition, *J Mater Sci.*, 1986, **21**, 1–25
5	GHANASHYAM KRISHNA, M. NARASIMHA RAO, K. AND MOHAN, S	Optical and structural characterization of zirconia thin films, *Appl Phys. Lett.*, 1990, **57**, 557–559

Thesis Abstract (Ph.D.)

Decision support data of interacting factors for design of footings by D. Bhanu Prasad
Research supervisor: B.V. Ranganatham
Department: Civil Engineering

1. Introduction

The problem of foundation analysis is divided into two broad groups: engineering and economic, whereas the design solution integrates both the aspects. The engineering problems resolve into questions of safety and suitability. The first question in evolving a suitable foundation design concerns the loads the superstructure will impose on the foundation and the second concerns the permissible tolerances of movements governing the type and use of the structure and these are considered fully specified for the purpose of this study. The third step concerns the analysis of the soil types and conditions and the next is to link up the two sets of facts, above and below ground, to choose the type of foundation that will match the demands of the structure with the conditions of the site. The final step is primarily an economic one. Among possible designs only one will give the designed safety and suitability at the least possible cost and that design will, therefore, be economically correct.

Isolated and combined footings of reinforced concrete are widely adopted foundations owing to the ease and economy of construction and maintenance and yet their rational design integrating engineering and economic aspects involves many an interacting factor. The key steps in the design are the determination of design-bearing pressure and the structural design. The investigation is in two stages (steps); the first is to assess the design-bearing pressure in terms of many significant parameters of the subsurface and superstructure and the second is the economic evaluation of rational alternate structural design.

2. Design-bearing pressure

Between the two criteria for the determination of design-bearing pressure (q_a), namely, bearing capacity and settlement, the latter governs the design in majority of situations as bearing-capacity failure is also preceded by unacceptable level of settlement. An idealised normally consolidated deposit is chosen for the analytical study on design-bearing pressure. Realising that the design-bearing pressure (q_a) is complexly affected by many factors, the scope of the present study is limited to the following unambiguous and quantifiable factors relevant to settlement criterion: compressibility index (C_c), load on the footing (w), depth of steady water table (D_w), depth of foundation (D_f), permissible level of settlement (S_a) and interference from adjoining column loads.

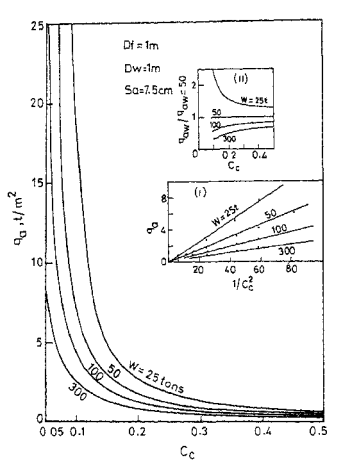

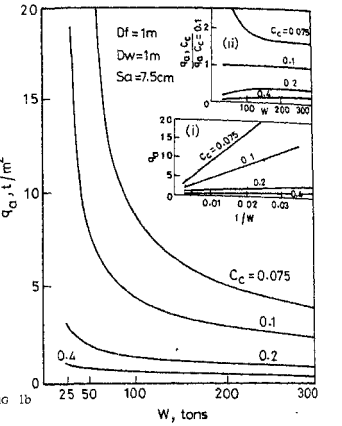

FIG 1b

FIG. 1a Variation of design soil-bearing pressure with, (a) compression index (b) effective column load and (c) permissible settlement

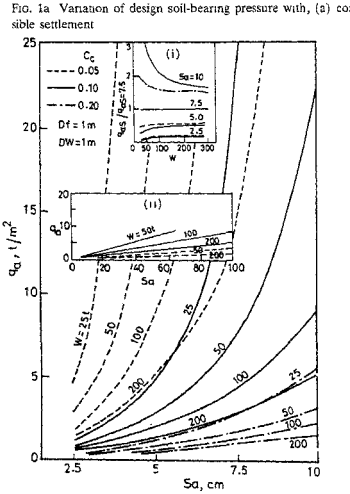

FIG 1c

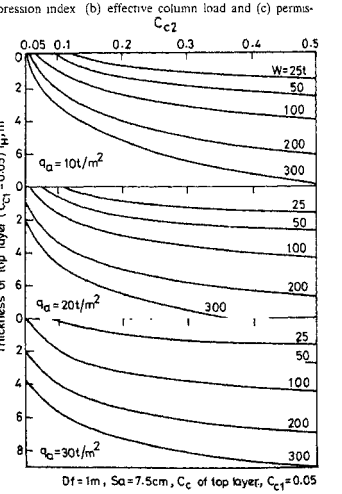

FIG. 2 Variations of thickness of less-compressible layer with compression index.

The compression index *versus* void ratio relation[1] is used to arrive at the *in-situ* void ratio (e_o) and resulting *in-situ* effective stress (p_o). The stress increase (ΔP) underneath the centre of footing due to applied uniform contact pressure is computed using Boussinesq expression. Starting with a tentative plan dimension the consolidation settlement is computed for the given values of compression index and effective load on the footing, the procedure is iterated till the computed settlement complies with the permissible value specified by the code and the resulting uniform pressure becomes the design-bearing pressure appropriate to the assumed design inputs. An approximate relation for design-bearing pressure deduced from theoretical considerations[2] is

$$q_a \propto \frac{S_a^2}{WC_i^2}.$$

Figures 1a–c are typical results verifying the validity of the above relation over a useful range of parameters

There is almost direct increase of design-bearing pressure with increase in depth to static water table owing to increase in effective stress from capillary suction. The increase in design-bearing pressure is much more pronounced as the soil in the capillary zone is considered less compressible. The results of design-bearing pressure with respect to less compressible soil above water table are used to arrive at the thickness of layer of improved ground of reduced compressibility to ensure a stated level of design-bearing pressure (Fig. 2). From these results, an empirical expression is suggested for the thickness (T_H) of top layer of less compressibility (C_{c_1}) for the stated level of allowable bearing pressure (q_a).

$$T_H = [0{\cdot}53 + 0{\cdot}002\ (q_a - 10)]\ [\sqrt{WC_c} - 1]10^{[1.55+0.5\ 1/C_c]C_{c_1}}.$$

When the predicted T_H is less than about 5 m, the error in prediction lies within ± 10%.

3. Structural design and economic evaluation

The structural action including failure mechanism of the conventional uniform thick footing still eludes the comprehension of the designer precisely defined distribution of contact pressure at the bottom. Because of the danger of punching distress the current practice is to design thickness of footing for punching shear and to arrive at reinforcement from flexural considerations. Shear failure should be avoided because, besides difficulties in predicting shear strength, it has little ductility and post-peak strength. This compelling consideration has motivated the examination of alternate structural forms of footings that will ensure flexural failure by eliminating punching shear failure. Two basic (alternate) forms studied are beam slab footings (uniaxial, axial and diagonal beam slab square footings) and tapered footings, the forms of which are such as to prevent failure in shear[3]. The uniaxial beam slab footing brings in real simplification of the structural action of footing in that slab and beams are to flex in mutually orthogonal directions and reinforcement is provided to resist bending only in one direction. With unidirectional flexing of slab, its design is refined by suitable tapering and curtailment of reinforcement. The main reinforcement in beam is also rationally curtailed. Uniaxial beam slab footing incorporating such improvements in design details is studied (Fig. 3). The footing systems are designed in conformity with code provisions. Computer-aided structural design and economic evaluation of footing systems have been made choosing design-bearing pressure (q_a) and column load (w) as independent inputs. A simple and accurate enough for design, relation between concrete quantity (Q_c) and design inputs (w and q_a) is deduced from idealised theoretical considerations,

$$Q_c \propto \frac{W^{1.5}}{q_a}.$$

Typical results of variation of cost with respect to W and q_a are shown in Figs 4a and b. The study has demonstrated the superior economic performance of uniaxial beam slab footing with refined design detailing that too with improved safety margin. Uniaxial beam slab footing with refined design details when adopted for other forms of footings like rectangular isolated and combined footings is shown to be superior. It is significant that the ratio of self weight of footing to the column load is not a constant but varies as $W^{0.5}/q_a$.

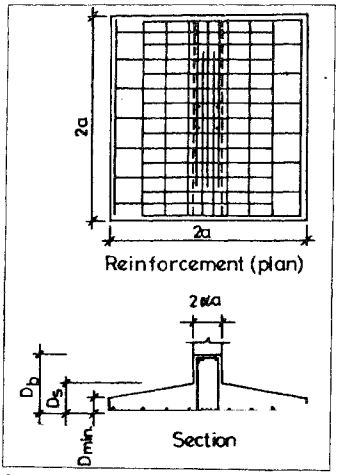

FIG. 3. Schematic sketch of reinforcement in uniaxial beam-slab footng.

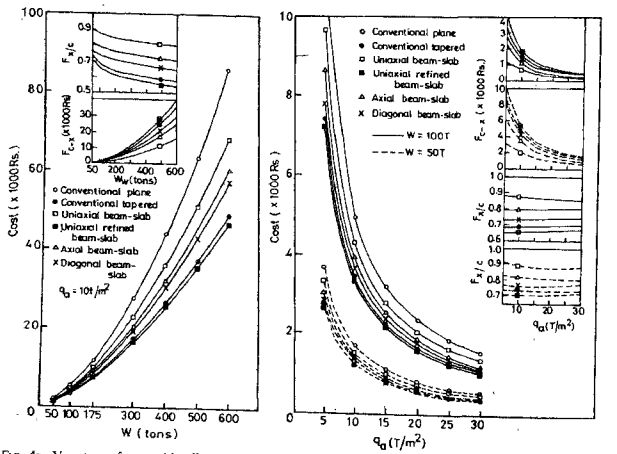

FIG. 4a. Variation of cost with effective load, and (b) allowable pressure.

The study has generated in realistic terms wide and useful database involving the identified interacting factors which could actively help footing design decision rational.

References

1 NISHIDA, Y — A brief note on the compression index of soil, *J Soil Mech Foundation Div*, ASCE, 1956, 82 (SM3), 1–14.

2 RANGANATHAM, B V AND NARAYANA REDDY, R — Integrating footing design with soil characteristics, *Proc Indian Geotech Conf*, 1987, Bangalore, India, Vol. 1

3. RANGANATHAM, B V — General report on structure–soil interaction, *Proc 5th Asian Reg Conf. on Soil Mech Foundation Engng*, 1975, Bangalore, India, Vol 2, pp 193–211

Thesis Abstract (M.Sc.(Engng))

Analysis of dynamical behaviour of an aircraft at touchdown by S. S. Kothari
Research supervisors: M. R. Ananthasayanam and K. Rajaiah
Department: Aerospace Engineering

1. Introduction

The landing of an airplane commences from the approach condition with the pilot operating the controls for a smooth touchdown followed by deceleration to rest or turn off the runway. Statistical information based on flight records is available concerning the approach and touchdown conditions as well as the acceleration experienced by the airplanes soon after. To connect such empirical statistical relations and be useful for airworthiness and design studies it is best to model the pilot input and the landing gear and subsequently analyse the response of the airplane[1–4]. This work deals with the effect of the landing gear on an airplane's response after touchdown.

2. Contribution of the thesis

The general equations of motion relevant to the aircraft together with the landing gear are derived and later simplified to analyse the longitudinal dynamical behaviour. Subsequently, by considering a series of increasing degrees of freedom models based on a series and parallel combination of spring, mass, moment of inertia and damper systems and with a method to account for aerodynamic lift as well provided the numerical and the modelling validation. A 'landing window' based on the force and moment equilibrium conditions limits the operation of an aircraft in the approach speed *vs* glide path angle plane due to aerodynamic, thrust, the landing gear strut compression rate and airplane altitude at touchdown, etc. (Fig. 1). This helps to understand the difficulties in specifying the touchdown conditions without knowing the pilot input. A possible way of overcoming such a problem is discussed. The response of the airplane is shown in Fig. 2 for the reference landing condition. Later, the effect of various parameters on the dynamical response of the airplane and the landing gear as also the g loads at the center of gravity and at the pilot's location is studied. The dominant parameters as shown in Table I were found to be the vertical velocity, as is to be expected, regarding which a large amount of flight data are available and unexpectedly the pitch attitude of the airplane about which there are meagre flight data and the damping coefficients of the landing gear oleos. The tyre and the oleo stiffnesses as also the aircraft speed have a modest effect and the aerodynamic characteristics of the airplane have only a weak influence on the g loads felt at the center of gravity and at the pilot's location.

It is suggested that the study of the problem by modelling the pilot input using the present-day digital flight data recorders and also the analysis for a flexible aircraft would be highly worthwhile.

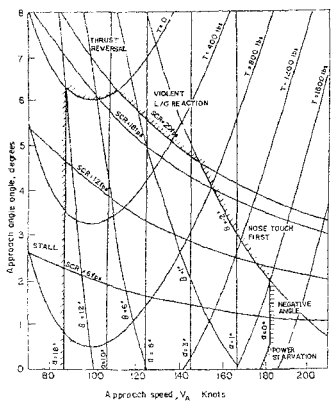

FIG 1 Landing window

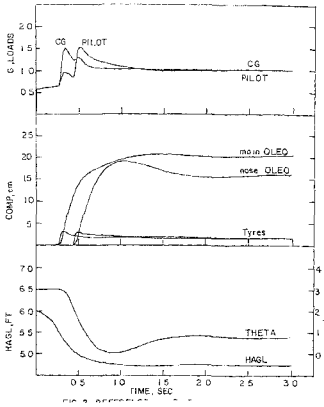

FIG. 2 Reference landing

Table 1
G load weightage of different parameters

		Influence on the peak G load at	
Set	*Parameter*	*CG*	*Pilot's location*
Flight parameters	Aircraft speed v	2	2
	Vertical velocity V_v	3	3
	Pitch attitude θ	3	3
Landing gear parameters	Main oleo stiffness	1	0
	Nose oleo stiffness	0	1
	Main tyre stiffness	2	0
	Nose tyre stiffness	0	2
	Main oleo damping	3	1
	Nose oleo damping	0	3
Aerodynamic characteristics	Stability margin	0	0
	Control effectiveness	0	0
	Pitch damping	0	0

where 0 indicates no or very weak influence, 1, weak influence; 2, strong influence; and 3, very strong influence.

References

1. MILWITZKY, B. AND LINDQUIST, D. C. *Evaluation of reduced mass method of representing the wing lift effects in free fall drop,* NACA-TN-2400, 1951
2. FLUGGE, W. *Landing gear impact,* NACA-TN-2743, 1952.
3. WILSON, R. J. AND MCKAY, J. M. *Landing loads and acceleration of XB-70-1 airplane,* NASA TND-4836, 1968
4. MCGEHEE, J. R. AND GADEN, D. *A mathematical model of an active control landing gear for load control during landing and rollout,* NASA TND-8080, 1976.

Thesis Abstract (Ph.D.)

Experimental investigations of hypersonic flow over a bulbous heatshield at Mach number 6 by P. Srinivasa
Research supervisors: N. M. Reddy and V. Adimurthy (VSSC)
Department: Aerospace Engineering

1. Introduction

Satellite launch vehicles that are used for launching large satellites usually have bulbous heatshield configurations During the atmospheric flight of such vehicles, these heatshields protect their payload from the aerodynamic environment. In the hypersonic part of the flight regime, the environment is especially severe with aerodynamic heating becoming significant in addition to the aerodynamic loads. To design such a heatshield, including its thermal protection system, the designer needs data on heating rates, pressure distributions, forces and moments, etc. For such information, it is essential to have a full understanding of the hypersonic flow over such configurations. Due to launch constraints, it is possible that the vehicle may have appreciable angles of incidence also For various design data and understanding of the hypersonic flow characteristics at angles of attack, both analytical and experimental methods are presently used. To use an effective computational method, large high-speed computing facilities are required. Here, primarily experimental methods are used to study Mach 6 flow over a bulbous heatshield configurations in a shock tunnel and in a conventional hypersonic tunnel

2. Measurements of aerodynamic heating

Aerodynamic heating of flight vehicles is a major concern at hypersonic speeds. To measure heating rates in a wind tunnel, it is essential to simulate the flight total temperature in addition to Mach number and Reynolds number, so that real gas effects are also simulated Vidal[1] used platinum thin film gauges in a shock tunnel for heat-transfer measurements. A hydrogen-driven shock tunnel with a run time of about 1 millisecond is used in this study and heating rates over a bulbous configuration model at $\alpha = 0$ to 17° are measured at freestream conditions of $M_\infty = 5.75$, $Re_n = 2.5 \times 10^4$ and $T_O = 1830$K. These conditions are typical of satellite launch vehicle trajectories. To ensure geometrical accuracy of the model, Macor-thin film heat-transfer gauges are developed using a simple technique. A new analogue circuit which includes constant current source, amplifier stage and T-section analogue network is developed to measure heat-transfer rates directly from the thin-film gauge signals. This circuit has high-frequency response and therefore can be used in shock tunnels where run times are of the order of a few milliseconds. Macor-thin film gauges are prepared in a simple but different way than elsewhere and therefore extensive calibration tests are made to obtain their constants like the backing material properties and temperature coefficient of resistance. For accurate data acquisition and processing, digital transient recorders and a computer are used.

3. Measurements of pressure distribution, forces and flow visualization

For measurements of surface pressure distribution, forces and moments and flow visualization studies, it is sufficient to simulate the flight Mach number and Reynolds number in the wind tunnel. Therefore, a conventional blowdown type of hypersonic wind tunnel with a run time of about 20 seconds is used for these studies on the same bulbous heatshield configuration. These studies are made at a Mach number of 6 and Reynolds number based on nose radius of 10^5. Pressure distribution measurements are made over the cylinder–boat tail–cylinder region at $\alpha = 0°$ and 5°. At 5° angle of attack, pressure distributions are obtained on nine planes in the range $\phi = 0$ to 180°. These measurements are made using a scanivalve, scanivalve digital interface unit and a computer. Force measurements are made in the same hypersonic tunnel using a strain gauge balance. These tests are done using the continuous pitch method with real time data acquisition using a computer. Normal force, pitching moment and axial force are measured at angles of attack 0 to 8°. To obtain good-quality oil flow pictures of the boat tail region of the model, conventional technique used in supersonic tunnels is modified and pictures are obtained at $\alpha = 0$ and 5°

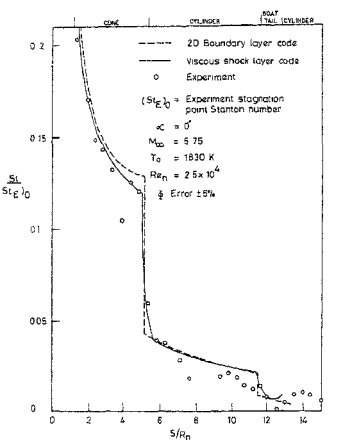

FIG. 1. Comparison of experimental heat-transfer rates with predictions (α = 0°).

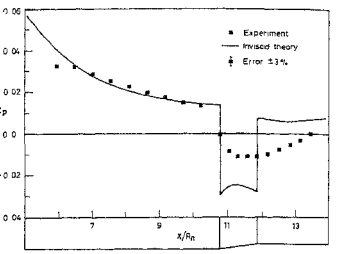

FIG 2 Pressure coefficient distribution at α = 5° and ϕ = 0 0°.

4. Computations

To compare the experimental results to a limited extent, computations are made using two CFD codes. An Euler[2] code is used to obtain inviscid pressure distribution and forces and moments at α = 5°. The inviscid shock shape obtained from this code is used as the input shock shape to a viscous shock layer code[3]. The viscous shock layer code is used to compute heat-transfer rates over the attached flow regions at α = 0 and 10°.

At zero degree incidence, the measured stagnation point heat-transfer rate agrees very well with the theory of Fay and Riddell[4]. Over the 20° blunt cone and cylinder region of the configuration, viscous shock layer results agree well with measured heating rates (Fig. 1). Oil flow picture and pressure measurements show longitudinal flow separation over the 15° boat tail with attachment on the downstream cylinder. The Euler code predictions of surface pressures over the attached flow regions of the first cylinder is in good agreement with experimental data (Fig. 2). Prediction of normal force and centre of pressure by the Euler code is in good agreement with measurements, mainly due to the reason that at α = 5°, the major contributions are from the attached flow over cone and first cylinder. About 15% difference in axial force coefficient is observed due to skin friction and flow separation in the experiment.

5. Analysis of hypersonic flow characteristics over bulbous heatshield based on experimental results

The experimental data obtained in this investigation are analyzed and examined in totality to evolve detailed flowfield characteristics at α = 0 (Fig. 3) and 5° (Fig. 4). Observed drop and subsequent increrase of heating rates over the first cylinder is attributed to reflected compression wave interaction with the laminar boundary layer. These reflected compression waves exist as a result of the interaction of Prandtl–Meyer expansion waves with the bow shock. Flow separation and reattachment zones over the configuration at α = 0 and 5° (typical of small angles of attack) are identified. At α = 0°, the flow separation over the boat tail is purely longitudinal. However, at α = 5°, the separated flow region over the boat tail and

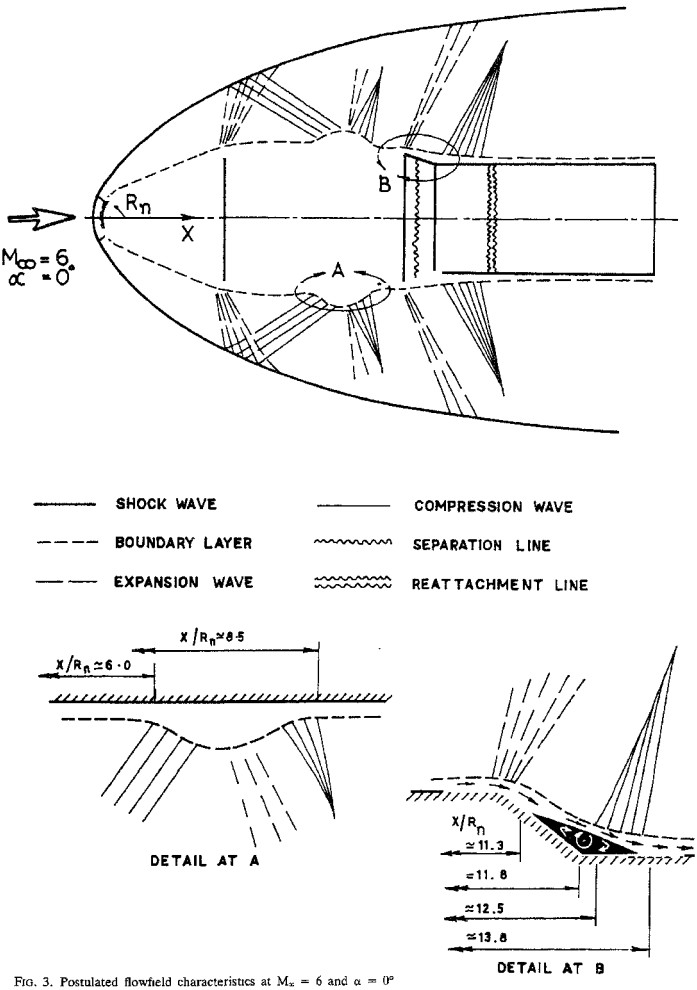

FIG. 3. Postulated flowfield characteristics at $M_\infty = 6$ and $\alpha = 0°$

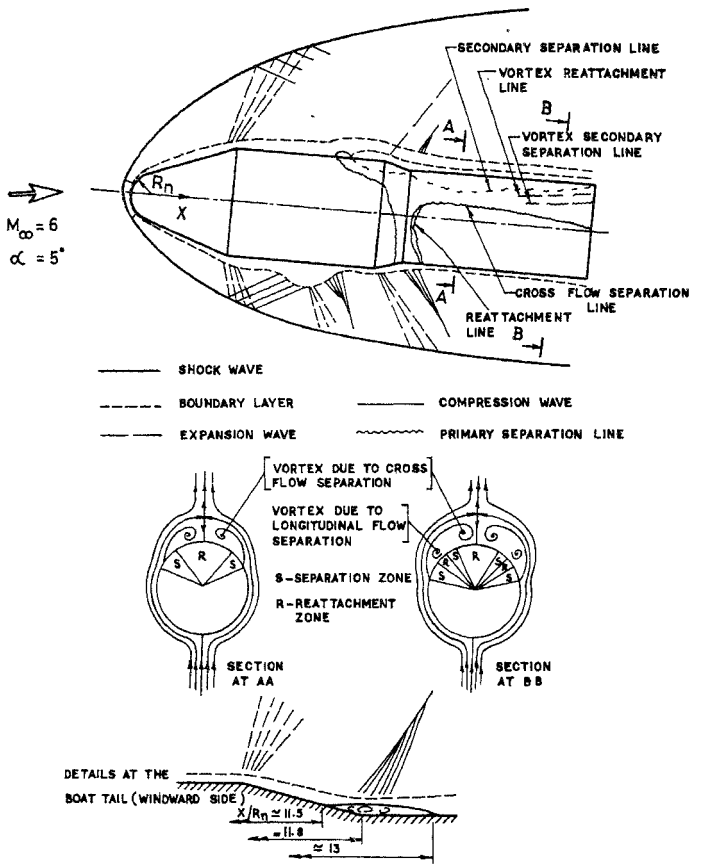

FIG. 4. Postulated flowfield characteristics at $M_\infty = 6$ and $\alpha = 5°$.

the second cylinder is due to longitudinal and cross-flow separation. The flowfield characteristics evolved in this work are of importance to numerical computations in selecting appropriate numerical schemes and computation–grid patterns.

6. Conclusions

Substantial data on hypersonic flow over a typical bulbous heatshield configuration are generated using experimental methods in a shock tunnel and a hypersonic tunnel. Overall flowfield details over a bulbous heatshield configuration at angles of attack are presented in this work

References

1 VIDAL, R. J. — *Model instrumentation technique for heat transfer and force measurements in a hypersonic shock tunnel*, Report No. AD–917–A–I, 1959, Cornell Aeronautical Laboratory, NY

2. SOLOMON, J. M., CIMENT, M., FERGUSON, R. E., BELL, J. B. AND WARDLAW, A. B. JR — *A programme for computing steady inviscid three-dimensional supersonic flow on reentry vehicles*, Vol. 1, Analysis and programming, 1977, Report No. NSWC/WOL/TR 77-28

3. MURRAY, A. L. AND LEWIS, C. H — Hypersonic three-dimensional viscous shock-layer flows over blunt bodies, *AIAA J.*, 1978, **16**, 1279–1286

4 FAY, J. A. AND RIDDELL, F. R. — Theory of stagnation point heat transfer in dissociated air, *J. Aero. Sci.*, 1958, **25**, 73–85

Thesis Abstract (M.Sc.(Engng))

The effect of oxygen transfer on the kinetics of formation of polyols by *H. Anomala*

by S. V. Patil

Research supervisors: N. V. S. Sastri and S. J. Jadhav

Department: Chemical Engineering

1. Introduction

Production of glycerol and related polyols by the fermentation route, particularly from the renewable raw materials, is assuming increasing importance in view of the escalating petroleum crude prices and shortage of fats and oils. Fermentation of sugars by osmophilic yeasts for the production of these chemicals holds high promise.

This work involves the study of the role of molecular oxygen on the kinetics of glycerol and arabitol formation in the fermentation of sugar by an osmophilic yeast *Hansenula anomala.*

2. Shake flask studies

The screening of osmophilic yeasts and optimization of nutrient and environmental parameters were carried out in shake flaks. After screening 16 strains of osmophilic yeasts, *H anomala* was selected for further studies on the basis of high yield of the product, glycerol. *H. anomala* produced mainly glycerol and arabitol in the ratio 4:1. The nutrient and environmental factors were optimized in the shake flask runs. Optimum yields of polyol (based on the per cent sugar consumed) were obtained with a starting sugar concentration of 30%, oxygen consumption of 45 mM/l/h and an alkaline pH of 8·0.

Polyol production was influenced by the dissolved oxygen (DO) concentration in the medium as well as by the rates of oxygen consumption. High sugar concentrations in the medium drastically decreased DO concentration and created quickly anaerobic conditions which affected sugar utilization and cell growth. With limited rates of oxygen supply, polyol yield remained stationary while the cell yield increased with

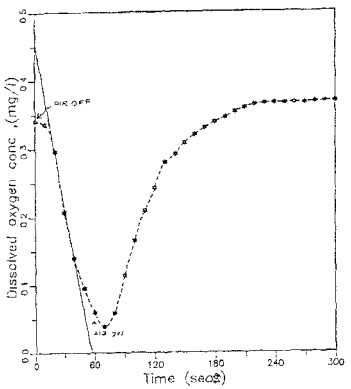

FIG. 1. Estimation of volumetric oxygen demand rate.

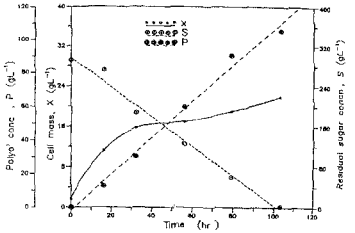

FIG. 2 Effect of sugar concentration (30%)

sugar consumption. Highly aerobic conditions lead in increased cell mass yield and low polyol yield. The critical role of oxygen supply on the yields of polyol was established in shake flask experiments.

3. Measurement of oxygen transfer rates (OTR)

The oxygen transfer rates were quantified in a Chemap fermenter. Oxygen transfer rates in the fermenter were determined by (i) the sulphite oxidation method, and (ii) the dynamic method of grassing out. It was shown that the OTR obtained by the sulphite oxidation method were not applicable to slow-growing microorganisms like osmophilic yeasts. The dynamic method developed by Taguchi and Humphrey[1] has the advantage of measuring the volumetric mass transfer coefficient (K_La) in actual fermentation. It is also very simple as it involves the use of a fast-response DO probe. Measurements were made of transient DO concentrations in a respiring culture after stopping the air supply. This results in a linear decline in the DO concentration as shown in Fig. 1. The slope of the line between 'air off' and 'air on' points yields OTR of the organism. A maximum OTR of 6·2 mM/l/h was obtained in the experiments.

4. Oxygen transfer effects

In fermenter studies, the effects of process parameters on cell growth and polyol production are best illustrated by typical time course concentration profiles of substrates and products as shown in Figs. 2 and 3. In these figures, measured values of polyol concentration (P), cell mass (X), residual sugar concentration (S), per cent saturation (pO_2) and pH of the medium are plotted against time. The time course profile of cell mass indicates three distinct phases: the first one shows rapid cell growth under oxygen limitation with little polyol formation. The rate of oxygen consumption is high, but constant and the rapid growth phase is terminated after about 18 hours. The second phase is marked by a sharp increase in the value of DO and a linear increase of polyol concentration with time, reaching a maximum value at the point of total sugar utilization. Polyol yield in this phase increases with increase in the DO value. The third stage of the process begins at the point of total sugar consumption when rapid cell growth commences again, probably due to switchover of metabolism of the organism utilizing glycerol as substrate in place of sugar.

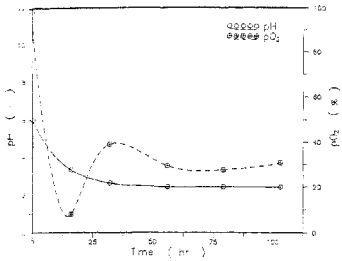

FIG 3 Effect of sugar concentration (30%).

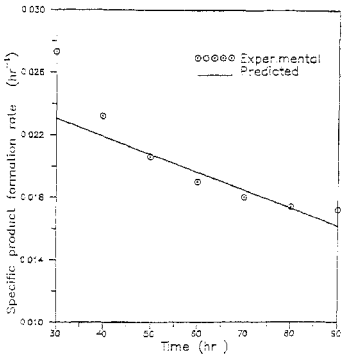

FIG. 4 Comparison of experimental and predicted specific product formation rate

From the experimental evidence it is clear that the growth process during the product formation was not limited by the OTR as the DO concentrations corresponded to 40 to 70% of oxygen saturation values. The initial rapid cell growth phase, when very little of polyols is produced, could be considerably shortened by enhancing OTR or by increasing the O_2 partial pressure. At the end of growth phase the aeration rate could be considerably reduced during polyol production. Thus, it is profitable to conduct fermentation in two stages as far as aeration is concerned.

One curious point that was observed in this study concerned inverse relationship between the specific growth rate of the cells and the substrate concentration. This is due to drastic decrese in the solubility of the second substrate, oxygen, as the sugar concentration increased.

Increased product yields were obtained under alkaline conditions. It was observed that a pH of 8 is optimum for product yield. The other optimum conditions established for maximum polyol production are: aeration rate, 0·54 VVM; agitation rate, 600 rpm; initial sugar concentration, 30%. The maximum yield of polyol based on sugar utilization is 51%. In this mixture, glycerol and arabitol were found to be in the ratio of 4·1. The optimum productivity of polyol formation is 1·1 g/l/h on fermenter scale experiments.

5. Kinetic model

A kinetic model has been proposed to take into account the effect of concentrations of sugar, oxygen and cell mass on the rate of product formation. This can be used for design purposes. The specific rate of product formation is given by

$$\mu_{mp} = \mu^*_{mp}\left[\frac{S}{K^*_s + S}\right] \tag{1a}$$

$$\mu_{mp} = \left[\frac{\mu_{mp} C_L}{K_x + C_L}\right] \tag{1b}$$

$$K^*_s = \frac{K_s C_L}{K_x + C_L} \tag{1c}$$

where S is the concentration of the sugar and C_L, the concentration of DO The kinetic coefficients μ_{mp}, K_s and K_i are evaluated from Lineweaver–Burk plots made from the experimental rate data. The observed rates of specific growth are compared with the predicted values from eqn (1) in Fig. 4. The agreement between the experiment and the model has been found to be quite good except in the initial phase of product formation which corresponded with the termination of the fast cell growth phase.

Reference

1 TAGUCHI, H AND HUMPHREY, A. E *J Ferment Technol.* (Jap) 1966, **44**, 881

Thesis Abstract (M.Sc.(Engng))

Instrumentation for holographic interferometry and some applications by M. R. Sajan.
Research supervisors: B. S. Ramprasad and E. S. R. Gopal
Department: Instrumentation and Services Unit

1. Introduction

Holographic techniques have become important for nondestructive testing in research and industry[1]. The method is simple, easy to implement and is often cost-effective. Major objectives of the research work were to develop a holographic recording set-up and to perform holographic interferometry experiments for the measurement of corrosion rate of materials, which is an important engineering problem[2,3]. There exist several methods for its measurement. The feasibility of holographic interferometry method for the measurement of corrosion rate of materials is investigated in detail. Advantages of the method over the conventional measurement techniques are also discussed.

2. Experimental techniques

A vibration-free table is constructed for performing holographic experiments using a thick rubberised coir foam as vibration isolator. Optical and mechanical components are fabricated in the laboratory with good precision. A lensless Fourier transform geometry is used for recording holograms. The stability of the set-up is evaluated by using a long-legged Michelson interferometer and also by recording a few double-exposure holographic interferograms.

The set-up is used for the measurement of corrosion rate of aluminium in sodium hydroxide solution. A glass cell with a drainage valve is fixed in the set-up for dissolving sample plates. The sample plate is screwed on to the mount attached to the glass cell. First exposure is given after filling the cell with water. The water is drained off from the cell and the specimen plate is allowed to dissolve in sodium hydroxide solution of known concentration for a fixed time interval. After dissolution, the plate is cleaned and the cell is filled with water. Now the second exposure is given. While reconstructing the hologram, the virtual image of the sample plate can be seen overlaid with a fringe pattern. This fringe pattern is a measure of thickness loss of the plate due to dissolution If N is the number of fringes, the thickness loss t can be found out from the relationship

$$t = \frac{N\lambda}{2 \cos \theta/2 * \cos \delta}$$

where λ is the illuminating wavelength (632.8 nm), θ, the angle between the illuminating and viewing directions, and δ, the angle between the displacement vector and the bisector of the angle. In these experiments, the displacement of the object is along the bisector, which means $\delta = 0$. θ is chosen as 46°. The equation reduces to $t = \frac{N}{2 \cos \theta/2}$.

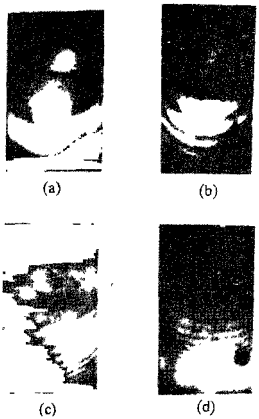

FIG. 1. Interference fringes from double-exposure holograms representing thickness loss of an aluminium plate dissolved in 0 5N NaOH for different dissolution times, a) 5, b) 15, c) 25, and d) 35 minutes.

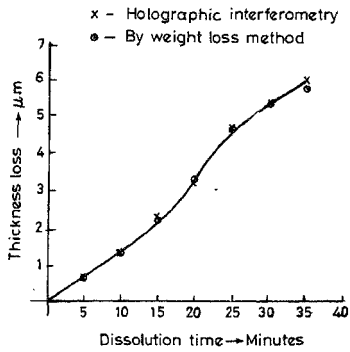

FIG. 2 Corrosion rate of aluminium in 0.5N NaOH.

In the darkroom it is very difficult to conduct the dissolution part of the experiment without disturbing the components in the recording set-up. To avoid this difficulty, a kinematic plate holder[4] is fabricated for fixing the sample plate. The mount can be taken outside, the dissolution of the sample can be done outside the dark room and the mount can be relocated exactly in the original position ensuring a zero fringe condition Also the components in the set-up are not disturbed accidentally in darkness.

3. Results and discussion

Some of the interferograms obtained for the dissolution of aluminium plate in sodium hydroxide solution are shown in Fig. 1. The thickness loss is also found out by the weight loss method. The results obtained from the weight loss method and the holographic interferometry method are plotted in Fig. 2. The results are in good agreement.

Experiments were also carried out for the measurement of the dissolution rate of Al–Ni alloy in sodium hydroxide and glass in hydrofluoric acid.

The major limitation of the present method is the loss of contrast of the interference fringes for high-dissolution times or for higher concentration of the solvent. This is due to the change in the surface micro-structure of the plate due to dissolution[5]. A simple speckle-shape analysis is performed to study the changes in the surface microstructure of the specimen plate due to dissolution. Several speckle patterns from the same sample plate surface are recorded after dissolving the sample plate for different dissolution times. The kinematic plateholder is used to replace the specimen plate in the original position after dissolution. Visual examination of the speckle patterns is sufficient to indicate any change in the shape of the speckles.

In the case of aluminium dissolved in sodium hydroxide, the size and shape of the speckles change gradually with increase in dissolution time as shown in Fig. 3. This would lead to the loss of contrast of the holographic interference fringes for higher dissolution times.

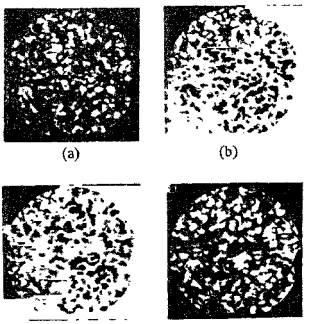

FIG. 3. Speckle pattern photographs of an aluminium plate dissolved in 0 25N NaOH for different dissolution times. a) Initial speckle pattern, b) 10, c) 20, and d) 30 minutes Visual examination reveals many changes in the structures of the speckles in photograph (d) compared to (a).

When brass is allowed to dissolve in 2% nitric acid, even after just 5 minutes of dissolution time, the shape of the speckles changes drastically. This points out the rapid wavefront decorrelation introduced by the dissolution of brass in nitric acid. Hence, it is difficult in practice to get holographic interference fringes in the case of brass dissolved in nitric acid.

For glass dissolved in hydrofluoric acid, the speckle pattern does not show any significant change even after large dissolution times.

The holographic interferometry method has the following advantages.

(a) The method is simple and gives the direct measurement of thickness loss.

(b) Localised corrosion effects can be studied which are not possible by conventional methods.

(c) *In-situ* measurements are possible in case of large components fixed to a system.

(d) Using real-time holographic interferometry, it is possible to monitor corrosion rate continuously.

Usually, the interference fringe pattern is photographed and analysed manually. For automatic analysis of fringes, a microprocessor-controlled fringe scanning system is developed. The displacements or deformations causing the formation of the fringe patterns can be visualised in 3D with the help of a computer. The performance of the set-up is evaluated by analysing a few interferograms from a Fizeau interferometer for testing flatness of optical flats.

Limitations exist for the measurement of corrosion rate by holographic interferometry method due to the loss of contrast of the interference fringes for higher dissolution times. Also, large amount of thickness loss causes large number of interference fringes. It is very difficult to analyse such a closely packed fringe pattern. In spite of these limitations, the technique offers further investigation possibilities in the accelerated corrosion studies of materials. The speckle shape analysis can be used to characterize materials and solvents suitable for study using holographic interferometry.

References

1. JONES, R AND WYKES, C — *Holographic and speckle interferometry*, 1989, Cambridge University Press
2. BEHRENS, D — *Corrosion Handbook*, 1987, Dechema, FRG
3. MACDONALD, D D., LEE, K. H., MOCCARI, A AND HARRINGTON, D. — Evaluation of alloy anodes for aluminium–air batteries Corrosion studies, *Corrosion*, 1988, **44**, 652–657.
4. RAMPRASAD, B. S AND RADHA, T. S. — A simple method for the measurement of stress in evaporated thin films by real-time holographic interferometry, *Thin Solid Films*, 1978, **51**, 335–338
5. ASHTON, R A., SLOVIN, D. AND GERRITSEN, H. J. — Interferometric holography applied to elastic stress and surface corrosion, *Appl Opt*, 1971, **10**, 440–441.